Internal wave patterns in enclosed density-stratified and rotating fluids

Interne golfpatronen in dichtheidsgelaagde en roterende vloeistoffen in afgesloten bekkens

(met een samenvatting in het Nederlands)

Proefschrift

ter verkrijging van de graad van doctor aan de Universiteit van Utrecht
op gezag van de Rector Magnificus, Prof. dr. W.H. Gispen,
ingevolge het besluit van het College voor Promoties
in het openbaar te verdedigen
op maandag 13 oktober 2003 des middags om half drie

door

Astrid Margaretha Maria Manders

geboren op 5 april 1975 te Venray

Promotoren: Prof. dr. J.J. Duistermaat
Prof. dr. F. Verhulst
Faculteit der Wiskunde en Informatica, Universiteit Utrecht
Co-promotor: Dr. L.R.M. Maas
Koninklijk Nederlands Instituut voor Onderzoek der Zee

Dit proefschrift werd mede mogelijk gemaakt door financiële steun van de Nederlandse Organisatie voor Wetenschappelijk Onderzoek (NWO), in het kader van het programma Niet-lineaire Systemen, onder projectnummer 620-61-392.

ISBN 90-393-3478-1

Contents

1 Introduction **5**
- 1.1 Waves in the interior of fluids . . . 5
- 1.2 Internal gravity waves . . . 6
- 1.3 Inertial waves . . . 10
- 1.4 Internal waves in enclosed basins . . . 12
  - 1.4.1 Reflection . . . 13
  - 1.4.2 Two-dimensional enclosed basins . . . 14
  - 1.4.3 Three-dimensional enclosed basins . . . 16
- 1.5 This thesis . . . 18

2 A smooth convex enclosed geometry **21**
- 2.1 Introduction . . . 21
- 2.2 Theory . . . 23
- 2.3 Results . . . 27
- 2.4 Special trajectories . . . 33
- 2.5 Breaking of basin symmetry . . . 34
- 2.6 Perturbed circle . . . 36
  - 2.6.1 Application to ellipse and third degree curve . . . 39
- 2.7 Discussion . . . 41
  - Appendix: Lyapunov-Exponent . . . 43

3 Observations of inertial wave structures **47**
- 3.1 Introduction . . . 47
- 3.2 Theory . . . 49
  - 3.2.1 Inertial waves . . . 50
  - 3.2.2 Vorticity-conserving flow . . . 54
- 3.3 Experimental set-up . . . 54
- 3.4 Results . . . 57
  - 3.4.1 Vertical cross-sections . . . 57
  - 3.4.2 Horizontal cross sections . . . 64
- 3.5 Discussion . . . 66
  - Appendix: Vorticity-conserving flow . . . 70

4 The 3-D structure of the inertial wave field **75**
4.1 Introduction . . . 75
4.2 Theory . . . 76
4.2.1 Derivation of Poincaré equation . . . 77
4.2.2 Plane wave solutions . . . 78
4.2.3 Solution in two dimensions . . . 79
4.2.4 Refraction of plane waves . . . 81
4.2.5 Three-dimensional ray-tracing . . . 86
4.2.6 Towards three-dimensional solutions . . . 87
4.3 Experimental set-up . . . 90
4.4 Results . . . 91
4.4.1 Vertical cross-sections . . . 94
4.4.2 Horizontal cross-sections . . . 97
4.5 Discussion . . . 100
4.5.1 The three-dimensional wave field . . . 100
4.5.2 Modal solutions . . . 101
4.5.3 Limitation of energy concentration . . . 102
4.6 Conclusions . . . 103

5 Observations of internal tides in the Mozambique Channel **105**
5.1 Introduction . . . 105
5.2 Description of the Mozambique channel . . . 106
5.3 Internal wave models . . . 108
5.4 Yo-yo results . . . 110
5.5 Current meter results . . . 113
5.5.1 Barotropic currents . . . 115
5.5.2 Internal tides . . . 116
5.6 Discussion . . . 124
5.7 Synthesis . . . 125

Bibliography **127**

Samenvatting **135**

Dankwoord **142**

Curriculum Vitae **144**

Chapter 1

Introduction

1.1 Waves in the interior of fluids

Waves owe their existence to a restoring force, acting on a perturbation of a background equilibrium state. This perturbation is forced back to its original position, overshoots since it has a finite velocity when reaching it, and the sign of the restoring force reverses. This process is repeated, resulting in an oscillation. The type of wave depends on the particular restoring force. For geophysical fluids, this can be gravity, for example for surface water waves, but also surface tension (small capillary waves at the surface), the pressure gradient (sound waves), or the Coriolis force (Poincaré waves, Rossby waves). The wave energy propagates, but the particles of the fluid just oscillate and pass the energy through, after which they return to their equilibrium position (in linear approximation). Which waves are relevant depends on the scale and specific setting one is interested in. On the scale of the ocean, Rossby waves are visible, whereas for a ship the wind-generated surface waves are most important.

This thesis is about a special class of waves, that propagate *through* the fluid: internal waves, which have their maximum amplitude in the interior of the fluid. They occur in both density-stratified and rotating fluids, as well as in the combined case, and are therefore relevant for the fluid basins of the Earth (lakes, oceans, atmosphere and the liquid outer core in the Earth's interior). In this introduction, first the two types of internal waves will be introduced and their relevance in nature is discussed, with emphasis on oceanographical implications. Then the effect of wave reflection is brought forward. More specifically, repeated wave reflection in an enclosed basin may lead to the formation of patterns of energy concentration. The study of this pattern formation, both theoretically and with experiments, is the main topic of this thesis. The study is completed with field observations of internal waves in a cross section of the Mozambique Channel.

1.2 Internal gravity waves

A kitchen-sink example of internal waves can be observed in a tank (glass) filled with two fluids of slightly different density that do not mix easily, for example oil on water. A perturbation of the interface between these fluids will propagate as a wave along this interface. Away from the interface the amplitude of the wave decreases and the free surface of the upper layer hardly moves. Gravity, reduced by the relative density contrast, or equivalently, buoyancy, provides the restoring mechanism. Therefore these waves are called *internal* gravity waves or buoyancy waves. Such waves on an interface can be compared with surface gravity waves on the boundary between water and air. However, since the density contrast between oil and water is much smaller than between air and water, the restoring force is weaker. This makes that internal waves have larger amplitudes, smaller phase speeds and longer periods than surface gravity waves for the same forcing.

A historical report of this phenomenon is given in a letter from 1762 by Benjamin Franklin. In an 'Italian lamp' he observed strong motion on the interface between oil and water, while the surface of the fluid was tranquil, and repeated his observations in experiments. Such internal waves also explain the long-known 'dead water' phenomenon, often encountered in fjords. In such water, a ship only moves at a fraction of its normal speed. The explanation is that the ship generates waves on the interface between the upper layer (fresh water originating from river outflow) and the lower layer of fluid (salty sea water), thereby losing part of the energy that would otherwise have been used for progression (see figure 1.1). Although the explanation seems evident nowadays, it was not until about 1900 that it was reported extensively by the famous oceanographers Fridtjof Nansen and Walfrid Ekman, and explained by V. Bjerknes. Ekman also carried out experiments to verify the explanation. A more complete overview, including the historical citations, can be found in Gill (1982). This dead water is also a potential hazard to swimmers in deep lakes, when in summer a warm surface layer develops above colder water. Although no reports are known with direct evidence, it is an effect to be aware of.

Internal waves need a stable stratification. An unstable stratification, with light water below and heavy water on top, cannot support waves, the slightest perturbation would lead to overturning, such that the heavy water flows to the bottom and the light water rises to the top. The most common cases of stratification are a layer of warm water (due to solar heating) on top of a cold water mass, or a layer of fresh water (due to river output) on top of a salty water mass. Strictly speaking, the internal waves on the interface between the fluids of different density in a two-layer system are called interfacial waves. In nature, the density stratification is usually not discrete. But a continuous stratification can also carry internal gravity waves. They again have maximum amplitude in the interior, but in the absence of a sharp density transition they can propagate *obliquely* through the fluid instead of horizontally along the interface.

The stability of the stratification is expressed in terms of the buoyancy frequency, often called the *Brunt-Väisälä-frequency* and denoted by N. It is the frequency with which a parcel of fluid oscillates vertically when it is brought out of equilibrium. It depends on gravity g, the gradient in the background density stratification $\rho_0(z)$ in the direction against gravity (z),

and the local sound speed c_s:

$$N^2 = -\frac{g}{\rho_0}\left\{\frac{d\rho_0}{dz} + \frac{\rho_0 g}{c_s^2}\right\}. \tag{1.1}$$

The sound speed accounts for the thermodynamic effects of rising or sinking on the density of a fluid parcel. It can be calculated using an equation of state that relates the density to pressure, temperature and salinity. The fluid is stably stratified if $N^2 > 0$.

The basic equations govering a density-stratified fluid are the equations of conservation of momentum, conservation of density and the continuity equation. If plane monochromatic waves of frequency ω are substituted, the dispersion relation follows. It relates the wave frequency to the wave number vector, that describes the direction of propagation and the distance between crests and troughs. The dispersion relation reads

$$\frac{N^2 - \omega^2}{\omega^2} = \tan^2\theta, \text{ or more directly } \frac{\omega^2}{N^2} = \cos^2\theta. \tag{1.2}$$

This relation describes the elementary and rather unusual properties of internal gravity waves. The magnitude of the wave vector appears irrelevant, the frequency is only related to N and the direction of propagation θ, the angle of the wave vector with the horizontal (direction of gravity is vertical). Another curious property is that the group velocity vector, denoting the direction of energy propagation, is at right angles with the wave vector and makes an angle θ with the vertical axis.

The waves that propagate away from the source thus form a 'St. Andrews cross'. This is illustrated in figure 1.2. Energy propagates along the lines ('wave rays') of the cross, crests (black) and troughs (white) are parallel to these lines, they fade away rapidly with increasing distance to the wave rays. The oblique propagation results from the fact that a frequency different from the natural frequency N is imposed. The fluid must adopt this forcing frequency in such a way that the restoring force due to reduced gravity (buoyancy) matches this frequency, which is done by *oblique* oscillation. Freely propagating buoyancy waves with frequency larger than N are not possible, as indicted by the dispersion relation. The fluid cannot follow the forcing anymore for such frequencies and perturbations are trapped to the forcing body.

Internal gravity waves can be found in nature. For example the Earth's ocean and atmosphere are density-stratified. In the upper ocean and the troposphere (lowest 11 km of the atmosphere, containing most of the water vapour and clouds), N takes values of the order of 0.01 rad/s. Above the tropopause, in the stratosphere, N is up to twice as large. In the deep ocean N is more than ten times smaller. Internal waves are found everywhere in the ocean. An example of a spectrum, that shows the drop in kinetic energy for frequencies larger than N is shown in figure 1.3. The open-ocean wave spectrum is more or less universal, this spectrum is referred to as the Garrett-Munk spectrum (Garrett & Munk, 1972). The criticism that this universality ruled out physical sources and sinks (Wunsch, 1975) is appropriate, but only near continental slopes, ridges and seamounts significant deviations of the spectrum are reported (Wunsch, 1976; Eriksen, 1982). The Garrett-Munk-spectrum is used as a canonical spectrum to compare spectra of different locations and identify processes that are responsible for deviations from this spectrum. Still, improvements are proposed to this spectrum, to facilitate comparison of different observations (Levine, 2002). The dominant frequencies in the

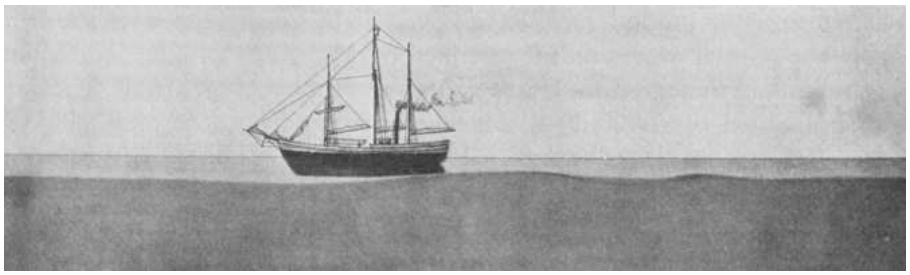

Figure 1.1: Laboratory experiment by Ekman to demonstrate the generation of internal waves by a ship on the interface between two layers of different density. The lower layer has been dyed. The 'ship' (an illustration of the famous Norwegian research vessel 'Fram' was drawn over it later on) is towed from right to left such that internal waves are generated in the wake of the ship (picture from Gill, 1982).

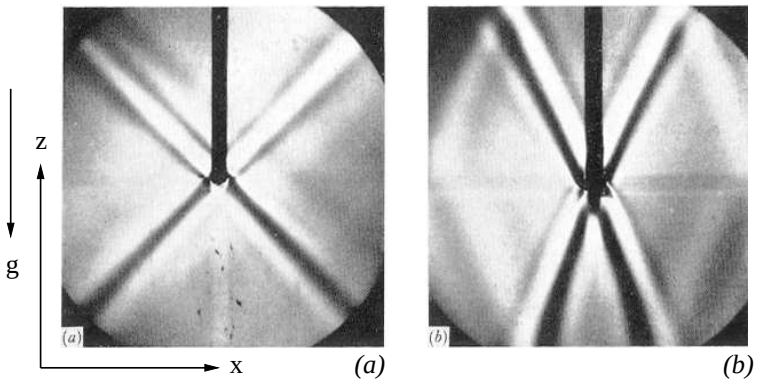

Figure 1.2: Observations of internal gravity waves in the vertical plane by Mowbray and Rarity (1967) (pictures from Turner, 1973). A small horizontal cylinder, at the end of the thick black vertical structure, oscillates vertically in a uniformly density-stratified fluid. Energy propagates away along rays, of which the angle with respect to the vertical changes with frequency: in *(a)* $\omega/N = 0.615$, in *(b)* $\omega/N = 0.900$. Black and white lines represent the crests and troughs, they are aligned along the rays and propagate perpendicular to them. Visualization is achieved by the Schlieren method, based on the principle that slight density changes change the refractive index of the fluid and perturb the light that shines through the fluid. In figure *(b)* also the reflected waves are faintly visible.

spectrum are the *inertial* frequency f, determined by the local Coriolis parameter (we will come back to this later) and the semidiurnal tidal frequency M_2 due to the action of the moon. Internal waves with tidal frequency are named internal tides. Depending on the stratification and the forcing mechanism, internal waves can have any scale, from tens of metres to tens of kilometres and periods of minutes to days.

Internal waves can be generated when wind or tidal motion is directed across a slope and the flow displaces isopycnals (surfaces of equal density). Conversion of the barotropic tide (loosely speaking: the flow that is uniform over the depth) to internal waves (baroclinic tide) is considered as an important sink for the barotropic tidal energy. This occurs at the coastal

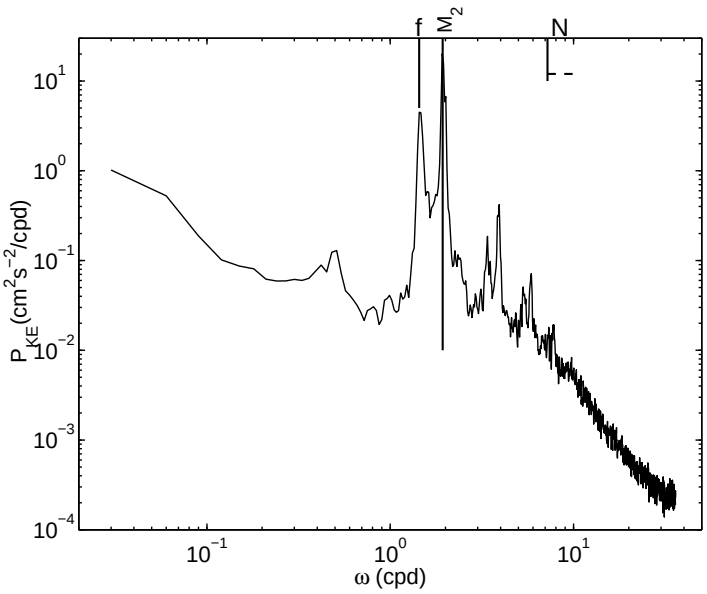

Figure 1.3: Kinetic energy spectrum, depicting power P_{KE} per frequency ω (cycles per day) band of velocities observed by a current meter that has been deployed for 11 months in the Bay of Biscay, at 3810 m depth (water depth 4810 m), 45° 48' N, 06° 50' W, about 100 km from the base of the continental slope (picture after van Haren *et al.*, 2002). Clearly visible are the enhanced energy levels at the semidiurnal tidal frequency M_2 and at inertial frequency f (and higher harmonics). For frequencies larger than N (horizontal dashed line denotes the uncertainty) the energy content of the spectrum drops rapidly.

shelf edges, where the bottom slope is relatively strong, that is a few degrees, with internal wave rays that also have slopes of a few degrees. Where the bottom slope equals the slope of the internal waves, generation of the waves is particularly effective (Baines, 1986).

But conversion near the top of the continental slopes only accounts for part of the dissipation. Interaction of tidal currents with bottom topography, like sea mounts, islands and oceanic ridges, is theoretically seen as another important source of internal waves. Estimates of the strength of the barotropic tide, based on satellite sea surface height altimetry, can be plugged into numerical models to estimate the associated tidal currents (Egbert & Ray, 2001). These currents in turn interact with topography, and it appears that most tidal energy is lost at locations where the currents are perpendicular to the topography, which is exactly the mechanism for internal tide generation. The idea that the flow over ridges is more cross slope than near the continental slopes, where the flow must be directed more or less parallel to it, makes that ridges are in general considered as a more important source. Notable exceptions are shelf seas where tidal currents are strongly enhanced, resulting in strong internal tides. A well-known example are the strong internal waves in the Bay of Biscay due to the strong tides in the Channel between England and France.

Internal waves can propagate over large distances, and are observed hundreds of kilome-

tres away from the supposed generation area. Evidence is found from current meter measurements in the open ocean, far away from generation areas (Morozov, 1995) or, more recently, has become available via satellite altimetry (Ray & Mitchum, 1997). Although the surface displacement caused by the internal tides is approximately 1000 times smaller than the amplitude in the interior (tens of metres, resulting in surface amplitudes of a few centimetres), these deviations of a few centimetres can now be separated from the total elevation field. The decay of the waves might take place via reflection at the bottom and interaction with the thermocline (Gerkema, 2001).

Reflection of internal tides at slopes and ridges may also lead to energy concentration, especially if the reflected wave ray is parallel to the slope (Dauxois & Young, 1999). But also reflection upslope, when the wave rays are steeper than the slope (Wunsch, 1969; Cacchione & Wunsch, 1974), or reflection downslope, when the wave rays are less steep than the slope (Maas & Lam, 1995; Maas *et al.*, 1997) leads to concentration of energy and a reduction of scale. Concentration of energy may lead to non-linear and/or viscous processes and even to wave breaking. This transfers energy to the smallest scale of motion, such that it is available for mixing processes (Ivey & Nokes, 1989).

Mixing is still a hot item in oceanography (Munk & Wunsch, 1998). A certain amount of mixing is necessary to maintain the global ocean circulation. The observed values of diffusivity in the open ocean are a factor 10 too low as compared to the required globally averaged values. It is assumed that mixing takes place locally, at the boundaries of the oceans and in shallow seas, through interaction of the flow with topography. Thus, even higher mixing rates are expected in these areas. Internal wave induced mixing could contribute considerably to the total mixing but estimates are still coarse and generally based on large scale observations. Therefore, more insight in internal waves is desired.

Concentration of wave energy and mixing in the ocean are not only important from a physical perspective. Intense mixing will prevent the deposition of sediment, which in turn may make the environment suitable for life. Maybe even more important, due to mixing a nutrient flux may be provided to an otherwise poor environment, where the absence of organic carbon is the limiting factor (Genin *et al.*, 1992). The existence of thin layers (tens of centimetres) of phytoplankton may be due to internal wave shear, causing stretching and spreading of a thicker (in the order of 10 metres) patch of phytoplankton (Franks, 1995).

1.3 Inertial waves

A stable density gradient is not the only setting for internal motion. Rotation alone can cause a 'stratification' in the fluid that supports waves that are in many respects similar to internal gravity waves. When the fluid rotates uniformly, the homogeneous fluid is stably and continuously radially stratified, namely in angular momentum. For a fluid that rotates with angular frequency Ω, at radial position r the fluid has velocity $v = \Omega r$ resulting in angular momentum $I = vr = \Omega r^2$. The pressure gradient force and the centrifugal force provide a dynamic equilibrium in the coordinate system rotating with the fluid. When putting a parcel of fluid out of equilibrium in the radial direction, its velocity will be different from the velocity of solid rotation at the new position, because it conserves the angular momentum it had at the original position. With this new velocity, the outward centrifugal force at the

internal gravity waves		inertial waves
density $\rho(z)$	*stratification*	angular momentum $I(r)$
buoyancy (reduced gravity)	*restoring mechanism*	inertia (Coriolis force)
$\omega = N$	*natural frequency*	$\omega = f = 2\Omega$
$\frac{N^2-\omega^2}{\omega^2} = \tan^2\theta$	*dispersion relation*	$\frac{\omega^2}{f^2-\omega^2} = \tan^2\theta$

Table 1.1: Comparison of the two types of internal waves

new position does not balance the inward pressure gradient force. The parcel experiences a restoring force (Coriolis force) and will start to oscillate. These waves are called *gyroscopic waves* (LeBlond & Mysak, 1978) or more commonly *inertial waves* (Greenspan, 1968*b*).

When waves with frequency ω, less than the Coriolis parameter $f = 2\Omega$, are generated, they will propagate under a fixed angle with the rotation axis. In this case, the angle of propagation depends on the frequency of the wave and the rotation frequency. The dispersion relation reads

$$\frac{\omega^2}{f^2-\omega^2} = \tan^2\theta, \text{ or } \frac{\omega^2}{f^2} = \sin^2\theta \tag{1.3}$$

Again the anomalous dispersion, with energy propagation perpendicular to propagation of crests and troughs, appears.

Inertial waves closely resemble internal gravity waves. A direct comparison is given in table 1.1. The analogy is discussed more precisely by Veronis (1970). The most important difference is that internal gravity waves are essentially two-dimensional, particle motion is linear, whereas gyroscopic waves are three-dimensional, particle motion is circular, due to the Coriolis force. As will be argued further on, this has important consequences for the behaviour in three-dimensional enclosed basins.

Inertial waves may play a role in the liquid outer core of the Earth. They could be driven by the Earth's precession. Since the outer core consists of electromagnetic fluid, inertial waves there may contribute to the Earth's magnetic field (Malkus, 1968). Internal gravity waves probably do not exist, since due to convection the fluid in the outer core will be rather homogeneous. Aldridge & Lumb (1987) report that frequencies calculated for specific eigenmodes of inertial waves in a spheroid of the dimension of the outer core match frequencies observed in long period gravimeter data from two large earthquakes. Strictly speaking, the outer core should be modelled as a spherical shell. The authors claim that the differences are only a few percent, but it must be mentioned that for a spherical shell the structure of the solutions may differ considerably from those of the full sphere, as we will see further on. However, the frequency ranges apparently match and observations of these long period oscillations and comparison with theoretical inertial wave behaviour in the outer core would give more insight in the properties of the outer core.

A completely different system where these waves come into play are spacecraft. Often they rotate about one of their axes and contain a fluid tank for stability or to store fuel. It is important that they do not become destabilized by inertial waves (Manasseh, 1993). Also liquid-filled ballistics appear to become destabilized, resulting in unpredictable paths (Aldridge *et al.*, 1989).

Inertial waves are possibly relevant for the deep ocean or regions of convection, where the density stratification is weak. Van Haren & Millot (2003) recently found evidence of inertial waves in the Mediterranean Sea. Also the Arctic seas exhibit a loss of stratification, which would enable the existence of inertial waves. But generally N is larger than f in the ocean. Because of their close resemblance, in a fluid that is both density-stratified and rotating, internal and inertial waves combine into a single 'gravito-inertial' or 'inertio-gravity' wave, depending on the relative strength of f and N. Their dispersion relation reads

$$\tan^2\theta = \frac{N^2-\omega^2}{\omega^2-f^2} \quad \text{or} \quad \omega^2 = f^2\sin^2\theta + N^2\cos^2\theta. \tag{1.4}$$

When N is larger than f, and $\omega \ll N$, the hydrostatic approximation is acceptable, assuming that the vertical pressure gradient is purely determined by the static density of the water column. This approximation however eliminates the possibility of true inertial waves. Since in oceanography this approximation is widely used, inertial waves that propagate obliquely through homogeneous fluid are not well known. The term inertial wave or inertial oscillation is in this context often used to designate waves whose frequency equals twice the local vertical projection of the rotation frequency $f = 2\Omega\sin\phi$, with ϕ the geographical latitude. These inertial oscillations are commonly observed in the ocean (Fu, 1981) and often form the largest peak in the frequency spectrum (figure 1.3). But in the hydrostatic framework these do not propagate. This thesis will not deal with this degenerate situation.

Nevertheless, the rotational contribution will alter the behaviour of internal waves such that particle motion is no longer rectilinear but becomes circular, which has consequences for the behaviour in three-dimensional enclosed basins. Also, the combined waves, which can only exist in the frequency range $f < \omega < N$, experience *turning surfaces*, across which they cannot propagate as a free wave since f becomes larger than ω. Often, on a sphere, these are referred to as turning latitudes, but strictly speaking, when gravity and the rotation axis are not parallel, these are curved surfaces (Friedlander & Siegmann, 1982). Internal waves of semidiurnal frequency can propagate over most of the globe, their turning surface is around 75 degrees North or South, but for internal waves of diurnal frequency this latitude is around 30 degrees. The effect of such turning latitudes on wave ray patterns is investigated for a full sphere by Friedlander & Siegmann (1982); Friedlander (1982), and for a spherical shell by Dintrans *et al.* (1999) and may lead to trapping of the wave at its turning surface (Maas, 2001), when the bottom and the turning surface provide a kind of wedge from which the wave cannot escape. This mechanism may explain the strong oscillations of frequency f that are observed, that were generally attributed to local generation by the wind. The importance of the turning latitude and the exact stratification on the generation of internal waves at a continental slope was studied by Robertson (2001).

1.4 Internal waves in enclosed basins

When internal waves propagate in an enclosed basin, repeated reflection of the waves at the walls may lead to the formation of patterns. The resulting pattern is highly sensitive to the direction of propagation θ and the basin geometry.

We will look at steady wave patterns resulting for monochromatic waves. This implies that time can be eliminated from the description of the wave behaviour. The spatial behaviour of plane internal waves is governed by a three-dimensional hyperbolic equation, called the Poincaré equation (Cartan, 1922) in honour of H. Poincaré, who first reduced the system of linearized momentum equations and the continuity equation governing rotating fluid into this single equation (Poincaré, 1885). Sobolev rediscovered it and studied corresponding boundary value problems in the 1940's (Arnol'd & Khesin, 1998), therefore it is also known as the Sobolev-equation. This equation, here written in terms of the pressure, reads

$$p_{xx} + p_{yy} - \lambda^2 p_{zz} = 0 \tag{1.5}$$

where subscripts denote partial derivatives and λ^2 indicates $1/\tan^2\theta$, referring to the oblique propagation. Although this equation is linear, it cannot be solved in a straightforward way for enclosed basins of general shape. Oblique derivatives appear in the boundary conditions, which prohibit separation in equations for the different directions, and wave modes with wavenumbers related to the size of the basin cannot be generally found. Furthermore, it describes an ill-posed problem, which means that solutions are not continuously dependent on the parameters which appear in the problem, or solutions are not unique. This does however not mean that an ill-posed problem describes per definition unphysical situations. Although some of the consequences may be offending, at a different scale other processes may compensate for this, and the solution is certainly worth further investigation.

To find wave patterns, it appeared a fruitful approach to study the paths of wave rays. First, the effect of wave reflection will be illustrated. Then the effects of repeated wave reflection in a (quasi-)two-dimensional basin and in a three-dimensional basin are discussed. For convenience, N and Ω are taken uniform over the basin, such that the waves propagate along straight lines. A nonuniform stratification would lead to bending of rays and eventually to turning points, but would not alter the basic concepts, as long as the stratification is continuous and variations are on scales longer than the wavelength.

1.4.1 Reflection

As already mentioned, the direction of propagation of internal waves is restricted, depending on the strength of the stratification, the rotation rate and the wave frequency. Since the wave conserves its frequency, when the background conditions are unchanged the angle θ is conserved upon reflection. This means that we no longer have Snell's law, where the angle with respect to the normal to the boundary is conserved upon reflection. When an internal wave reflects at a horizontal or vertical boundary (perpendicular or parallel to the direction of gravity or rotation), there is no difference in practice. When two parallel wave rays reflect, their distance is unaltered. This is illustrated in figure 1.4(a).

But when an internal wave reflects from a sloping surface with angle α with the direction of gravity and/or the rotation axis, the results change considerably. When $\theta < \alpha$, wave rays travelling downwards in the direction of the slope are reflected upslope (subcritical reflection), and the distance between two wave rays decreases upon reflection (figure 1.4b). This is called focusing. For wave rays coming from the other direction, the distance decreases, and we speak of defocusing. When $\theta > \alpha$, wave rays travelling downwards towards the slope are reflected downslope (supercritical reflection, figure 1.4c). This also results in focusing, and

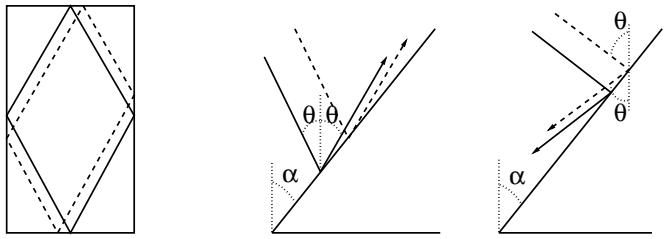

Figure 1.4: *(a)* Reflection at horizontal and vertical walls, *(b)* subcritical reflection at sloping wall, $\theta < \alpha$, *(c)* supercritical reflection at sloping wall, $\theta > \alpha$

by defocusing for upward propagating waves. When $\alpha = \theta$ (critical reflection), the 'reflected' wave rays are parallel to the slope and are focused infinitely.

The wavelength is not conserved upon reflection: focusing leads to a decrease of the wavelength. The energy becomes more concentrated and velocity with which energy is transported (the group velocity) decreases to zero.

1.4.2 Two-dimensional enclosed basins

An infinitely long channel of uniform cross section can be interpreted as two-dimensional. One can describe the waves in a cross section and assume uniformity in the third (say y) spatial dimension, removing gradients in y. However, for inertial waves particle motion itself remains three-dimensional due to the Coriolis force. The Poincaré equation (1.5) reduces to a wave equation in x and z (hyperbolic equation):

$$p_{xx} - \lambda^2 p_{zz} = 0. \tag{1.6}$$

Solving the wave equation in spatial coordinates in an *enclosed* domain comes with specific complications.

Classically, the wave equation is solved by separation of variables, translating the single equation into two equations, one for each (spatial) coordinate, coupled via an eigenvalue. Then a set of standing waves is obtained, a combination of sine and cosine functions, or some special functions, with wavelengths that match the dimensions of the basin such that there is no motion through the walls, and with suitable prefactors such that the forcing is represented correctly. This method is suitable for some very simple geometries, like the rectangle (main axes parallel to direction of gravity and rotation) and the circle, or geometries that are related to them via a linear coordinate transformation (for example the ellipse, that can be transformed into a circle). If the slope of the wave rays (wave frequency) or the dimension of the basin is changed, the wave pattern is destroyed, since it does not 'fit'. Standing wave patterns only exist for a discrete set of frequencies, depending on the angle θ and the aspect ratio of the rectangle. For a rectangle or circle this is still a large set, related to the set of rational numbers, although the wave patterns will have small scale structures for the largest part of this set. The irrational numbers correspond with the frequencies or aspect ratios for which no standing wave solution exists.

For a basin with a sloping wall separation of variables is not possible, since the boundary conditions at the slope couple the two dimensions. Then the 'method of characteristics' can be used to determine the structure of the solution (John, 1978). This method reduces a partial differential equation to a set of ordinary differential equations in terms of a single variable along so-called 'characteristic curves' of the differential operator (or simply *characteristics*). This single variable relates the variables of the partial differential equation and defines curves on which the relation between these variables is constant. The (constant) functional value on such a characteristic is determined by 'initial conditions', say a function $f(s)$, on a certain part s of the domain S. Problems arise if a characteristic has multiple intersections with s (say s_1 and s_2), since $f(s_1)$ is not necessarily equal to $f(s_2)$ and the value along the characteristic must be unique. Therefore, this method is mainly used for evolution equations, where the behaviour in time is described and since time is always increasing such ambiguities cannot occur.

An example of such an evolution equation is the ordinary wave equation, where characteristics describe the space-time paths of the wave. But, if strict conditions on the 'initial conditions' are applied, this method can also be used for the wave equation in two spatial coordinates, as will be described in chapter 2. The characteristics then represent the spatial patterns of the wave rays. Since there is no time evolution, the pressure on the boundary, which depends on the exact forcing mechanism, determines the function $f(s)$. The problem is that in an enclosed domain, the characteristics will reflect at the boundary at several points, which may lead to multiply defined values. To avoid this, the pressure can be prescribed such that it obeys the periodicity conditions $f(s_1) = f(s_2)$ (Maas & Lam, 1995). It is however very well possible that the pressure on the boundary in a real physical experiment does not obey these periodicity conditions. It depends on the exact forcing mechanism. Probably this can be repaired when the full initial value problem is considered and time is reincorporated. For now, we are satisfied with the idea that the characteristics can be used to find basic properties of the spatial structure of the wave field.

The correspondence between standing waves and the use of characteristics is most easily demonstrated for the rectangle (figure 1.5a). As we have seen, separation of variables can be used when the main axes are parallel to the direction of gravity or the rotation axis. Alternatively, the method of characteristics yields closed characteristic patterns for the frequencies corresponding to standing wave solutions. The pressure on the boundary can be prescribed on the interval between two side reflection points of a single characteristic. The number of reflections needed to close a characteristic is called the *period* (loosely speaking, as slightly different definitions are also in use, for example in chapter 2). For the standing waves, all characteristics close onto themselves, and no net focusing occurs over a period. For the frequencies for which no standing wave exists, characteristics never close and fill the whole basin.

When the basin has a sloping wall, separation of variables is not possible, and focusing due to the sloping wall comes into play. This is illustrated in figure 1.5(b). A single characteristic reflects repeatedly, thereby approaching (but never actually reaching) a periodic orbit. All wave rays will approach this specific periodic orbit, which acts as a limit cycle and is therefore called *wave attractor*. There is net focusing over a period. Contrary to standing waves, such attractors are not destroyed immediately but slightly stretched or squeezed when the wave frequency or the size of the domain is changed slightly; they exist in parameter

intervals. Here, the pressure can also only be prescribed on intervals, in this case there are two such intervals. The largest intervals are between the characteristics starting at the upper left and right (not shown) corners and their subsequent surface reflection. Scales are ever decreasing around the attractor, the large pressure gradients around the attractor point at high velocities.

The study of solutions to the wave equations on a closed domain gained attention in the late 1930's. The wave equation on a rectangle was studied by Bourgin & Duffin (1939) and related to number theory in Bourgin (1939). General statements for more general geometries, in terms of mapping of the circumference (the boundary) to itself were done by John (1941). He did notice that there were maps for which all points are periodic, maps for which a limited number of periodic points exist (attractors), and maps for which no periodic points can be found, depending on the properties of the boundary. So, although the wave equation is linear, its solutions on an enclosed spatial domain have properties that can be described conveniently in terms that are known from non-linear dynamics. However, Bourgin, Duffin and John did not consider the physical implications of such solutions.

In fluid mechanics, the notion of obliquely propagating internal waves started only in the 1940's with the work of Görtler (1943, 1944). He remarked that singularities in the velocity might exist, without elaborating on it. In geophysics, the notion of isolated periodic wave rays is, following the work of Stern (1963), due to Bretherton (1964), who constructed such rays near the equator, corresponding to axisymmetric waves in a vertical cross section of the homogeneous, rotating spherical shell. They appeared to be attracting (Stewartson, 1971, 1972) and existed in frequency intervals (Israeli, 1972), but such attracting closed rays were considered physically unacceptable. Indeed, the ultimate consequence of wave focusing, an infinite concentration of energy along the attractor, is physically unfeasible as viscosity and nonlinear processes will prevent it. In a closed cone, wave reflection towards the lower corner was observed for wave rays that reflect supercritically, as shown in figure 1.6 (Greenspan, 1968*a*). Also in a wedge, a model of internal waves propagating from the deep sea towards the beach (subcritical reflection), a wave attractor was predicted, with infinite energy concentration in the apex. These waves have been investigated in laboratory experiments (Wunsch, 1969; Cacchione & Wunsch, 1974) and the decrease in wavelength upon reflection has been observed. Various other geometries were investigated by Maas & Lam (1995), and in a rectangular basin with one sloping side wall the predicted wave attractors were observed experimentally for both internal gravity waves (Maas *et al.*, 1997) and inertial waves (Maas, 2001). Experimental evidence is the ultimate proof of the value of the use of the method of characteristics to predict the wave pattern. From numerical work on a cross section of the spherical shell it appeared that when viscosity is added, the patterns of energy concentration are as predicted by the characteristics, although the mathematical attractor is replaced by (thin) shear layers (Rieutord & Valdettaro, 1997). Thus, the predictions based on tracing characteristics appears to describe the real solution fairly well.

1.4.3 Three-dimensional enclosed basins

For three-dimensional basins, the problems are more serious than for two-dimensional basins. For the cylinder (Kelvin, 1880) and the sphere (Bryan, 1889), separation of variables again leads to a discrete set of standing wave solutions. But a rectangular basin is already nontrivial.

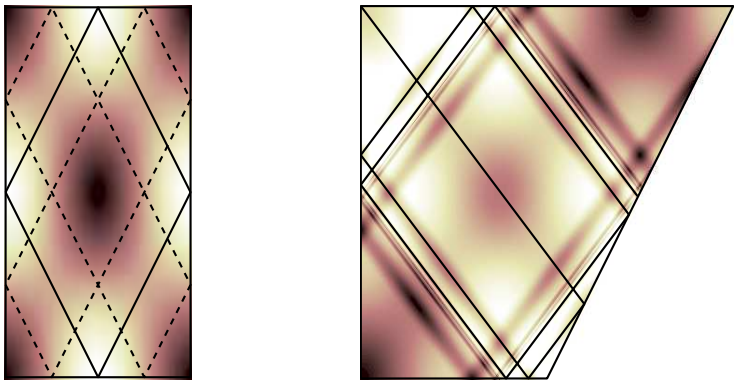

(a) *(b)*

Figure 1.5: Pressure field for the rectangle with and without sloping wall. For a rectangle, separation of variables generally yields standing wave solutions. For the rectangle with one sloping wall, separation of variables is not possible. In *(a)* all wave rays are periodic, in *(b)* wave rays rapidly approach a single periodic orbit, the wave attractor (central parallelogram), where the pressure field varies on very small scales. In *(a)* the pressure can be described along one of the side walls. In *(b)* there are two intervals where the pressure can be prescribed. The largest intervals are that between the ray from the upper left corner and its first reflection point at the top, and similarly, between the ray from the upper right corner and its first reflection point at the top (not shown).

For internal gravity waves, because of the rectilinear particle motion, the two-dimensional solution can still be applied since in the inviscid case particle motion parallel to the walls is a valid solution. Also separation of variables is possible, yielding a discrete set of standing waves. For inertial waves, this is not the case, because the circular particle motion conflicts with the requirement that there is no motion through the wall. Assuming standing waves in the vertical, the horizontal structure was solved, with amphidromic points and rapid changes near the walls, but without singularities (Maas, 2003).

As cylinders and spheres are widely used in laboratory experiments, (McEwan, 1970; Manasseh, 1992; Aldridge & Toomre, 1969), problems were not encountered. But also in geometries where standing modes cannot be found (spherical shell, truncated cone), experimental results in which stronger motion was detected for certain frequencies were still interpreted in terms of standing wave modes (Beardsley, 1970; Aldridge, 1972).

Unlike for a two-dimensional basin, where the method of characteristics can be used to construct solutions, to our knowledge no such general solution method exists for three dimensions. For problems in time and two spatial dimensions, the Riemann method can be applied as a 'follow-up' of the method of characteristics (see for example Myint-U & Debnath, 1987). But this method cannot be readily applied for three spatial dimensions, since the conflicts that are already encountered in two dimensions using characteristics become seemingly unsurmountable in three dimensions.

Although numerical methods and numerical capacity increase in strength rapidly, it is still problematic to solve the Poincaré equation numerically. Common practice is to include viscosity to make the problem well-posed. For the spherical shell solutions were computed

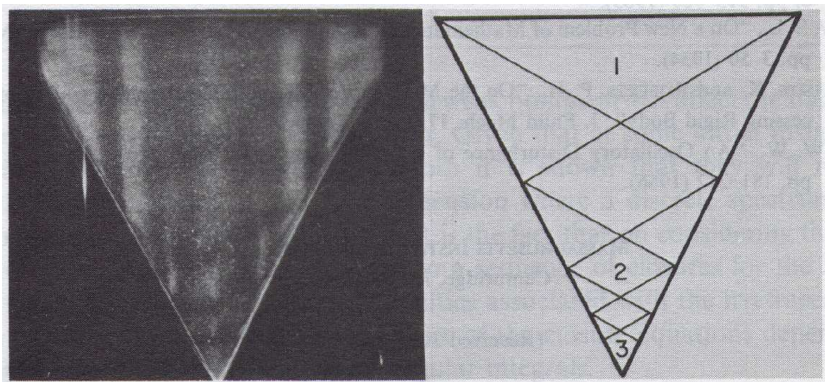

(a) *(b)*

Figure 1.6: *(a)* Experiment by Greenspan (1968*a*) in a cone rotating about its central axis, showing inertial wave rays (dark diagonal bands, compare with theoretical predictions *(b)*) emanating from the corner and reflecting at the boundaries according to the pattern in the right panel. Wave rays are finally trapped in the lower corner. Visualization is by means of aluminium flakes, that orient themselves according to the local shear and, depending on the orientation, reflect the light of a narrow beam. Interaction of wave beams with boundary layers induces a steady zonal flow (vertical bands). In region 1 the amplitude of the wave is small, in region 2 waves approximately have the amplitude of the imposed oscillation (modulation of the rotation rate), in region 3 it is smaller again. In region 2, waves are focused due to downward reflection. In region 3 shear, nonlinear terms or boundary effects may cause the decrease in amplitude.

by Hollerbach & Kerswell (1995), and more extensively by Rieutord & Valdettaro (1997), where the solutions are compared with wave ray paths. The latter paper gives a detailed description of the numerical method. The needed viscosity values, for the available numerical capacity, were larger than desired for physical applications like the liquid outer core or the interior of stars. Moreover, the solutions could not be extrapolated for lower values of the viscosity, as the solutions changed considerably with decreasing viscosity. It remains a topic of active research, where physical and mathematical knowledge are needed to obtain and select acceptable solutions.

1.5 This thesis

The body of this thesis consists of four chapters, in which different aspects of internal waves are studied. These chapters can be read separately.

In chapter 2 it is investigated whether attractors exist for a two-dimensional geometry without corners or other singularities. Not only a (tilted) rectangle, but even a 'lake' with parabolic bottom profile and a flat surface have corners. Critical latitude singularities play an important role in cross sections of a spherical shell. The geometry that was considered is a special convex, smooth curve that was defined by a third degree polynomial equation. Depending on a parameter value, it varied between a circle (no attractors possible) and a

triangle (vertices act as attractors). Also the slope of the wave rays is varied, such that a two-dimensional parameter space could be studied. The description of the successive reflections of wave rays at the boundary was given in terms of a map of the boundary to itself. We combined the theory of such maps with numerical ray-tracing and, when the curve is close to the circle, with asymptotic expansion.

In chapters 3 and 4, inertial wave attractors were studied in the laboratory. The question was if and how the theoretical two-dimensional attractors manifest themselves in a fully enclosed tank, where the two-dimensional description is at most valid as an approximation. A first positive answer to their existence is given in Maas (2001), where a wave attractor for inertial waves was observed in the laboratory. Chapter 3 of this thesis is an extension of this experiment. Experiments were performed on the 13 m diameter rotating platform of the Coriolis Laboratory in Grenoble, France, in a rectangular tank with a sloping side wall, of 107 cm wide, 80 high and 500 cm long. Six different frequencies were used, four of them within the frequency interval of the most simple attractor, one belonging to a standing wave in the two-dimensional approximation and one to a more complicated attractor.

In these experiments, the attractors and the standing wave were reproduced in part of the basin, again confirming the possibility of wave attractors in three dimensions. Since the tank was so long, however, not the whole basin could be captured in the experiments. Especially the influence of the walls that close the basin, and impose limitations on the two-dimensional approach, could not be studied properly.

In chapter 4, we therefore address the problem of the three-dimensional structure of the wave field further. Part of the experiments of chapter 3 were repeated on a much smaller scale: a tank of 19 cm wide, 19.5 cm high and 40 cm long, again with a sloping side wall was put on a 1 m diameter rotating table at the Fluid Dynamics Laboratory of the Technical University Eindhoven. Now measurements in the full horizontal plane and in vertical planes close to the end walls were obtained, resolving the structure of the inertial wave field better.

Although the method of characteristics does not apply for a three-dimensional wave field, wave ray paths were studied to investigate the possibility of convergence of wave rays towards an attractor, also when they initially do propagate in three dimensions. This does not lead to solutions, but it gives more insight in the behaviour of the waves and facilitates interpretation of the experimental observations.

In chapter 5, the possibility of concentration of internal waves in the real ocean was investigated. More specifically, the spatial distribution of internal wave energy in the Mozambique Channel was studied. This narrow (350 km wide) sea strait in between Mozambique and Madagascar has strong topography (from nearly 0 to 2.5 km depth) and reasonably strong tides. This makes the area favourable for the generation of internal tides. A rather wide array of current meters has been deployed in a cross section of this channel for one and a half year. The current meter records have been analysed to look for locations of relatively strong internal tidal motion. A two-dimensional ray-tracing model was used to predict wave ray paths. However, for a strongly varying stratification, like in the upper few hundred meters, scattering and internal reflections must be taken into account. A more sophisticated two-dimensional numerical internal-tide generation model, which includes these effects, is used to calculate the distribution of energy. Finally, the value of this thesis with respect to observations of internal waves in the ocean is discussed.

Chapter 2

Wave attractors in a smooth convex enclosed geometry

2.1 Introduction

Stably stratified fluids can carry waves that travel obliquely through the fluid. For density-stratified fluids they are called internal waves, owing their existence to a balance between the pressure gradient force and buoyancy. For a uniformly rotating fluid they are called inertial or gyroscopic waves and the radial stratification in angular momentum provides elasticity to the fluid. For a rotating fluid that is also density-stratified these effects are combined into inertio-gravity waves. The rotation axis is taken antiparallel to the direction of gravity for convenience in this study, parallel to the z-axis. The slope of the wave rays depends solely on the wave frequency, the strength of the density stratification and the rotation rate and cannot be altered due to reflection. We will restrict ourselves to uniformly stratified, uniformly rotating fluids so that the wave energy travels along straight lines (wave rays).

If the basin, in which the fluid is contained, is uniform in one of the horizontal coordinates, it is justified to consider two-dimensional plane waves. The behaviour of monochromatic waves is then governed by a hyperbolic equation in spatial coordinates in the vertical plane (Görtler, 1943, 1944). For an enclosed basin, this is an ill-posed problem: solutions change dramatically when parameters are changed slightly. For some special basin geometries, like the circle or a rectangle, one is able to obtain 'classical' regular solutions in terms of eigenmodes (standing waves, seiches) where every wave ray reflects back onto itself. Examples can be found in Høiland (1962) (circle, ellipse, rectangle), Franklin (1972) (arbitrarily oriented ellipse), Maas & Lam (1995) (rectangle, half ellipse). When the shape of the geometry or the slope of the wave rays is changed infinitesimally the standing wave is destroyed.

In general, separation of variables is not possible and one must use the method of characteristics to solve the hyperbolic equation. The characteristics can also be interpreted as wave rays (Maas & Lam, 1995). Because of the monochromatic Ansatz, time has been eliminated and the characteristics represent the spatial structure of the rays. It should be noted that a three-dimensional approach leads to a three-dimensional hyperbolic equation, called

Poincaré equation (Cartan, 1922), for which no such general method of solution is known to us for an enclosed basin.

When characteristics reflect at a sloping wall, they are focused or defocused. Reflection is not specular, parallel characteristics remain parallel. For internal waves propagating up a gentle slope, reflecting up-slope (subcritical reflection, horizontal component conserved upon reflection) at the slope and the surface, a decrease of wavelength and an increase of amplitude were predicted and observed in the laboratory (Wunsch, 1969; Cacchione & Wunsch, 1974). For a triangle, characteristics approach one of the vertices. This is experimentally shown for inertial waves in a rotating cone (Greenspan, 1968*a*; Beardsley, 1970), and described mathematically by Franklin (1972). In a different closed geometry, repeated reflection with focusing may lead to the approach to a limit cycle, the *wave attractor*. Examples are a basin of which the bottom is described by a parabola and a trapezoidal (bucket-shaped) basin (Maas & Lam, 1995), and the spherical shell (Rieutord *et al.*, 2001).

For inertial waves the peculiarity of trapping of a wave (the existence of a closed orbit) for the spherical shell is known from the 1960's (Stern, 1963; Bretherton, 1964). Closed ray paths were found for the equatorial region of a (thin) spherical shell. Somewhat later these trapped waves appeared to be limit cycles to which neighbouring wave rays converged (Stewartson, 1971, 1972), and it was noted that these limit cycles exist over continuous frequency intervals (Israeli, 1972). These limit cycles were later called wave attractors (Maas & Lam, 1995). Solution of the hyperbolic equation on a closed domain can also be treated as a mapping of the circumference onto itself (John, 1941). The mathematical notion of the existence of a limited number of periodic characteristics (attractors) for mappings of the circumference onto itself is older.

At first, a wave attractor was considered too pathological to be relevant for fluid dynamics (Stewartson, 1971). Indeed, the mathematical attractor, with its infinitely large concentration of energy around it, cannot appear due to viscous and nonlinear effects. But the attractor may be a good first order approximation for patterns to occur in a fluid. In laboratory experiments, theoretically predicted attractors have been observed both for internal waves (Maas *et al.*, 1997), and for inertial waves (Maas (2001), this thesis) in a basin with one sloping boundary. In numerical studies where viscosity was included, strong shear layers were found along patterns that were in agreement with the patterns of attractors predicted by the inviscid limit, as long as the mathematical attractor did not reflect more than about 10 times at the boundary (Rieutord *et al.* (2001); Tilgner (1999), both for the spherical shell).

The question arises what is essential for a geometry to bear the possibility of wave attractors. The spherical shell is a geometry with a 'hole' in the middle, it is not convex which introduces special behaviour due to the critical latitude singularity when the characteristic becomes tangent to the inner sphere (Israeli, 1972; Rieutord *et al.*, 2001). In Maas & Lam (1995) the parabolic basin and a bucket were investigated. The parabolic basin showed the presence of attractors. The bucket was a hybrid geometry which showed both attractors and standing patterns, depending on the parameter values. Both geometries have corners, which can also play a special role since they acts as critical points for all characteristics.

Here we study a geometry without such obvious special points. The smooth convex part of a third degree curve is adopted as a boundary. Depending on a parameter value, the convex part varies between a circle and a triangle. For the circle either all characteristics are periodic or no characteristic is periodic, for the triangle characteristics are always attracted to one of

the corners. The behaviour of the characteristics is investigated in terms of a map of the boundary onto itself.

In the next section the theory is explained and the map describing the successive reflections of a wave ray will be given. Also some definitions common in theory about one-dimensional maps are introduced. Then results will be shown from numerical iteration, followed by a discussion regarding the role of some special characteristics that close onto themselves. This leads to insight in the conditions under which attractors appear. Also, a criterion is derived that indicates whether attractors are present for first order perturbations to the circle. However, for the geometry under consideration second order theory is needed to describe the behaviour, as will be shown. Finally the results will be discussed and compared with results from literature.

2.2 Theory

We consider waves in an inviscid, linear, continuously stratified, steadily rotating Boussinesq fluid. The governing equations are the conservation of momentum, conservation of density and the continuity equation (see for example Krauss, 1966). The time dependence is eliminated by assuming the waves to be monochromatic (frequency ω), resulting in a factor $\exp(-i\omega t)$. The direction of gravity is the negative z-direction, the rotation axis is aligned along the z-axis. It is assumed that the basin is infinitely long in one horizontal direction, reducing the problem to a two-dimensional one. This enables the introduction of the stream function $\Psi(x, z)$ such that a single equation remains:

$$\frac{\partial^2 \Psi}{\partial x^2} - \kappa^2 \frac{\partial^2 \Psi}{\partial z^2} = 0, \tag{2.1}$$

with

$$\kappa^2 = \frac{\omega^2 - f^2}{N^2 - \omega^2}. \tag{2.2}$$

This is a wave equation (hyperbolic equation) in two spatial dimensions for real values of κ. N represents the buoyancy frequency, f is the Coriolis parameter and equals 2Ω, with Ω the rotation frequency. The physical condition of no flow through the boundary requires that

$$\Psi = 0 \text{ at the boundary.} \tag{2.3}$$

We will construct solutions using characteristics, since the possibility of separation of variables is restricted to some specific boundary geometries. These characteristics describe the spatial pattern of wave rays (see Maas & Lam (1995) for discussion) since time has been eliminated from the problem. The solution of (2.1) can be written in terms of the characteristic coordinates $\kappa x - z = c_1$ and $\kappa x + z = c_2$:

$$\Psi(x, y) = g(\kappa x - z) - h(\kappa x + z). \tag{2.4}$$

The slope of the characteristics is defined by κ, and as already mentioned solely depends on the wave frequency, the rotation rate and the buoyancy frequency. Therefore these waves are

sometimes called *monoclinical waves* (Tolstoy, 1973). In fluid dynamics one often does not work with the slope of the characteristics but with the angle θ of the characteristics (wave rays) with respect to the direction of gravity or the rotation axis, which are always uniquely defined. Here $\theta = \pi/2 - \arctan\kappa$.

The functions g and h are functions of the two characteristic coordinates only. If they are prescribed on the boundary, the solution is determined. The values of g and h on the boundary are conserved along characteristics, and the values at the boundary determine the solution in the interior. But since the geometry is closed, characteristics are 'reflected' (like wave rays) and the functions g and h on the boundary must obey some periodicity condition to avoid incompatibility. However, on a fundamental interval (an interval between a point on the boundary from which a certain characteristic leaves and its nearest reflection point) the function can be prescribed arbitrarily. From a physical viewpoint, prescription of g and h replaces the prescription of a forcing mechanism. In order to satisfy $\Psi = 0$ on the boundary, the functional values of g and h are identical when restricted to incoming and outgoing characteristic at the same point, that is when characteristics belong to one web built by a certain characteristic and all of its reflections.

Propagating internal or inertial waves conserve their slope κ upon reflection. This is correctly represented by these characteristics. When two parallel characteristics reflect from a boundary that is parallel or perpendicular to the direction of gravity or the rotation axis, their distance is conserved. But when they reflect from a sloping boundary, their distance may decrease (focus) or increase (defocus). In an enclosed basin, when focusing is not balanced by defocusing, rays may ultimately end up in a limit cycle, the so-called attractor. The patterns arising from the reflections of the characteristics form the framework of the structure of the stream function.

We want to obtain solutions for equation (2.1) on the domain of which the boundary Γ is parameterized by the convex part of the third degree curve

$$c = \frac{1}{\varepsilon}(x^2 + z^2) - z(x^2 - \frac{1}{3}z^2). \tag{2.5}$$

The parameter c is set to $c = \frac{1}{\varepsilon} - \frac{1}{3}$, to achieve that this curve is symmetric with respect to rotation over $\frac{2}{3}\pi$ around the origin. It has fixed points $(0,-1), (-\frac{1}{2}\sqrt{3}, \frac{1}{2}), (\frac{1}{2}\sqrt{3}, \frac{1}{2})$ regardless of the value of ε. The convex part varies between a triangle ($\varepsilon = 2$) and a circle ($\varepsilon \to 0$), depending on the value of the parameter ε. For $\varepsilon > 2$ there is no convex part, the curve then consists of isolated parts. The symmetry axes of the curve are the z-axis and the lines $z = \pm(\sqrt{3}/3)x$. Shapes of the curve for different values of ε are illustrated in figure 2.1.

The spatial structure of the wave field is determined by the pattern (web) formed by the spatial structure of the wave rays and their reflections. We will study the structure by describing the pattern formed by individual wave rays (characteristics).

A straight line has three intersection points with the third degree curve, one of these points lies outside the convex part. All three points are described by cubic roots. Expressions simplify if one of the intersection points is known, which is the case since one can choose a point on Γ as starting point for a characteristic. If the characteristic $z = \kappa x + b$ (belonging to the set of characteristics with positive slope) leaves from the point (x_n, z_n) on Γ, with

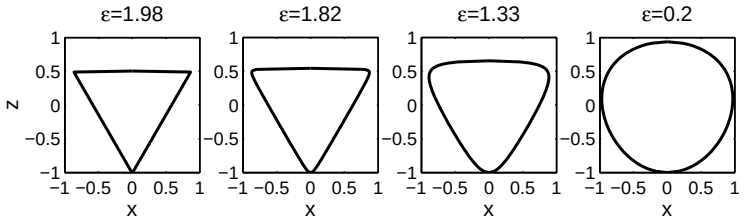

Figure 2.1: Shape of the curve for different values of ε.

$b = z_n - \kappa x_n$, then the next reflection point (x_{n+1}, z_{n+1}) is given by

$$z_{n+1} = \frac{1}{2z_n}\left(-z_n^2 - C_1 z_n \pm \sqrt{(z_n^2 + C_1 z_n)^2 + 4C_2 z_n}\right), \tag{2.6}$$

where

$$C_1 = \frac{-\frac{1}{\varepsilon}\kappa^2 - 2(z_n - \kappa x_n) - \frac{1}{\varepsilon}}{1 - \frac{1}{3}\kappa^2}, \qquad C_2 = \frac{\kappa^2(\frac{1}{\varepsilon} - \frac{1}{3}) - \frac{1}{\varepsilon}(z_n - \kappa x_n)^2}{1 - \frac{1}{3}\kappa^2}. \tag{2.7}$$

Now x_{n+1} follows from inserting z_{n+1} in the equation describing the characteristic, $x_{n+1} = (z_{n+1} - b)/\kappa$. The sign for the determination of z_{n+1} must be chosen as follows:

	$z_n < 0$	$z_n > 0$
$\kappa < \sqrt{3}$	$+$	$-$
$\kappa > \sqrt{3}$	$-$	$+$

(2.8)

For $z_n = 0$ the square root term vanishes, so there is no sign involved. The next iteration step is performed by following the same procedure, but now for the characteristic belonging to the set with slope $-\kappa$.

Following the successive reflections of a characteristics is equivalent to following the iterations of a map. Much is known about orientation preserving maps of the circumference to itself (see for example Arnol'd, 1965; De Melo & van Strien, 1993). Therefore an orientation preserving map is introduced, defined as the composition of two reflections, one for slope $+\kappa$ and one for slope $-\kappa$. Depending on whether one starts with characteristic with slope $-\kappa$ or with slope $+\kappa$ the map is said to be iterated forwards or backwards. This composite map will be called T and T^n is the n^{th} iterate of the map. It maps Γ onto itself. The position of a point on Γ can be parameterized by a single periodic parameter ϕ, where $z = r(\phi)\cos(2\pi\phi), x = r(\phi)\sin(2\pi\phi)$. The unusual convention of the coordinates is chosen in order to represent the symmetry in the z-axis. Here for any integer k the real numbers ϕ and $\phi + k$ represent the same point on Γ, we can make ϕ unique by restricting it to $[0, 1)$, but then have to jump discontinuously from 1 to 0 if we leave the interval at the right hand boundary. The transformation T corresponds to a *continuous* transformation $\widetilde{T}, R \to R$, which is unique up to addition of a constant integer k. If $\phi_0 \in [0, 1)$, then we can write $\widetilde{T}^n(\phi_0) = \phi_n + m$, where $\phi_n \in [0, 1)$ and m is an integer, both uniquely determined. The ϕ_n are the representations in $[0, 1)$ of the iterates of T on Γ, and m can be interpreted as a

winding number.

Different methods are used to study the behaviour of the 2-parameter map. Firstly, one can iterate the map for a certain parameter value combination (ε, κ) and directly plot a characteristic with its successive reflections. It gives a very intuitive insight in where focusing and defocusing take place on Γ.

Secondly, one can iterate the map for a range of values of one parameter, fixing the other parameter value. A Poincaré plot can be made by taking the last few hundred values of ϕ out of a larger number of iterations and repeat this for every parameter value. This plot gives insight in the change of behaviour of the map with the change of the parameter value regarding the presence and location of an attractor.

Thirdly, the rotation number can be computed. It measures the asymptotic average advance of ϕ per iteration of T. See for example Coddington & Levinson (1955) for details. The rotation number is defined as

$$\rho = \lim_{n\to\infty} \frac{\widetilde{T}^n(\phi_0)}{n}. \tag{2.9}$$

If $\widetilde{T}$ is replaced by $\widetilde{T}+k$, where k is a constant integer, then ρ is replaced by $\rho+k$. This means that for the transformation $T : \Gamma \to \Gamma$ the rotation number is well-defined modulo integers. If the rotation number is rational, so that it can be expressed as $\rho = \frac{p}{q}, p, q$ coprime, then there is a periodic orbit. The period of the orbit is q and $p < q$. If the rotation number is irrational, then the map is called quasiperiodic, the characteristics never close and finally fill a dense subset of the whole domain. The rotation number varies continuously and monotonously with the parameter value, and remains a constant, rational number in a window in parameter space for which there is a nondegenerate periodic point. A rational rotation number itself does not say anything about the character of a periodic orbit, it may be attracting or repelling (actually they usually occur in pairs, one attracting and one repelling) but it may also be neutral (every single ray is periodic, standing wave behaviour).

The Lyapunov exponent Λ indicates whether a periodic orbit is an attractor, neutral or a repellor. The factor e^{Λ} is the average factor with which a small interval $[\phi_0, \phi_0 + \epsilon]$ is stretched ($\Lambda > 0$) or shrunk ($\Lambda < 0$) after one iteration of the map. It is defined by (e.g. Schuster, 1984)

$$\begin{aligned}\Lambda(\phi_0) &= \lim_{N\to\infty}\lim_{\epsilon\to 0}\frac{1}{N}\log\left|\frac{T^N(\phi_0+\epsilon)-T^N(\phi_0)}{\epsilon}\right| = \lim_{N\to\infty}\frac{1}{N}\log\left|\frac{dT^N(\phi_0)}{d\phi_0}\right| \\ &= \lim_{N\to\infty}\frac{1}{N}\sum_{n=1}^{N-1}\log\left|\frac{dT(\phi_n)}{d\phi_n}\right|. \end{aligned} \tag{2.10}$$

In this study we will use an alternative formulation. We cannot work with the interval $[\phi, \phi+\epsilon]$ or the distance along the curve, since it depends on where the curve is intersected and therefore is not a measure of the convergence of the map. Therefore the perpendicular distance $\mathcal{D}$ between the characteristics passing through ϕ and $\phi + \epsilon$ is used. The ratio of the distance between rays before ($\mathcal{D}_{T^n}$)and after an iteration ($\mathcal{D}_{T^{n+1}}$) seems an appropriate measure from a physical viewpoint of focusing of a wave ray. We refer to the appendix for details for the

derivation of Λ in this specific case and just give the resulting formula:

$$\Lambda(z_0) = \lim_{N\to\infty} \frac{1}{N} \sum_{n=1}^{N-1} \log \frac{\mathcal{D}_{T^n}}{\mathcal{D}_{T^{n-1}}}. \tag{2.11}$$

It should be noted that the *ratio* of distances has a meaning, individual distances cannot be eliminated.

For some basin shapes it is possible to find a simple analytical expression for the Lyapunov exponent. An example is the bucket shaped basin (Maas & Lam, 1995), a geometry with two sloping walls with constant slope. Since the slopes are constant and the map linear, Λ can be determined with a 'bookkeeping' of the number of times that the ray reaches a divergent, convergent or neutral part of the map, corresponding to the sloping walls of the bucket or the horizontal walls. For the spherical shell, a very simple expression could be obtained for Λ, in terms of the latitudes of the reflections (Rieutord *et al.*, 2001).

In our case it was not possible to derive a simple explicit analytical expression for the Lyapunov exponent, since the slope of the boundary, and therewith the strength of the focusing, varies with the 'latitude' (ϕ) in a more complicated way. As a check to the conventional method, considering a large number of reflections to study the limiting behaviour of the map for a random starting point, we could alternatively start directly on the attractor of period q itself and apply the map q times, and calculate the Lyapunov exponent from that. The results are still numerical approximations, but this method saves the averaging over the large number of iterations for a random starting point. This method has been tested for the most simple attractor and the results agreed well with those for the conventional method.

2.3 Results

In this section we will show results for different parameter values to study the dependence of the map on the parameters ε and κ.

To illustrate the geometry and the idea of focusing a picture of the fate of a characteristic for $\varepsilon = 1.82$ and $\kappa = 1.5$ is shown in figure 2.2(a). The corresponding stream function is also plotted. The characteristic starts to the right (forward iteration) and ends up in the limit cycle of period 2. This is the most simple attractor and it exists over a range of parameter values, although its exact location will change with changing parameter values. When we would have iterated the map backwards, the attractor would have been located at the left and would be a reflection of the former attractor in the z-axis. Depending on the direction of iteration and the exact starting point of a certain characteristic, one of the two is an attractor, the other a repellor. A characteristic may change its direction from going clockwise to anticlockwise when it reflects critically. Critical reflection means that the characteristic directly reflects back onto itself, which occurs when the tangent to the curve is equal to minus the slope of the characteristic. For this different circulation direction a former repelling limit cycle turns into an attractor.

There are three fundamental intervals where the function g (or h) in equation (2.4) can be prescribed: one in between the two z-symmetric limit cycles, one to the left and one to the right, all for $z > 0.5$ in this case. These intervals are shown as black lines at the top boundary,

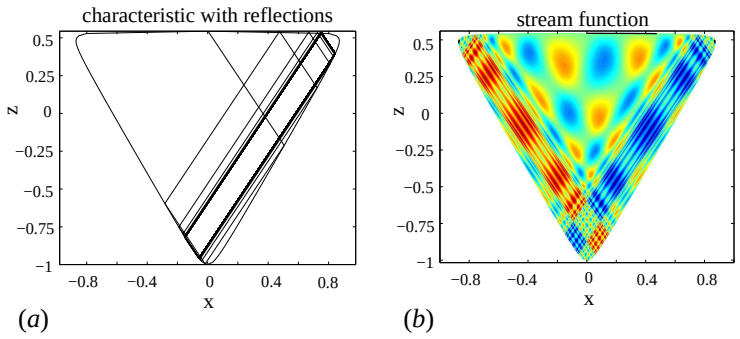

Figure 2.2: *(a)* Characteristic approaching an attractor and *(b)* corresponding stream function for $\varepsilon = 1.82$ and $\kappa = 1.5$. The black lines at the boundary represent the fundamental intervals.

directly right from the middle and on the leftmost and rightmost side, in figure 2.2(b). All three intervals have their own domain of influence. This is illustrated in the stream function plot. The intense grey-tones appear where information of two different fundamental intervals is incorporated, the more modest tones indicate that the information comes from a single fundamental interval. In all three fundamental intervals a sine-function was prescribed, with different absolute values to illustrate the different domains of influence. The derivative of the sine-function is zero at the boundary of the interval, which guarantees smooth solutions except on the attractor. However, in practice the forcing mechanism for the waves is prescribed and the derivative at the end of the fundamental interval is in general not smooth. Discontinuities in the velocity or the velocity gradient are reported for the precessing cylinder (Wood, 1965) and for forcing by oscillation of the end caps of a cylinder (Baines, 1967). Mathematically, there are no objections. In physical experiments discontinuities in velocity or the velocity gradient have been observed (McEwan, 1970).

In figure 2.3 the Poincaré plot is shown, where ε equals 1.82 and κ varies. There are distinct windows with attractors, separated by regions with high-periodic and quasiperiodic orbits. The regions with mostly quasiperiodic orbits may also contain attractors, but the intervals of κ over which they exist are too small to be visible on this scale. This will be illustrated later. Windows become substantially larger as κ increases. This has the following simple reason. To investigate the whole range of slopes, κ should vary between 0 and ∞. The angle of the characteristic with respect to the direction of gravity or rotation axis θ only varies between $\pi/2$ and 0. With $\kappa = \tan(\pi/2 - \theta)$ the interval $\pi/4 \geq \theta \geq 0$ is smeared out over the region $1 \leq \kappa \leq \infty$ whereas the interval $\pi/2 \geq \theta \geq \pi/4$ is compressed in the interval $0 \leq \kappa \leq 1$. But since the parameter κ arises in the definition of the map and it gives a good resolution in the most interesting region we chose to use this parameter rather than work in terms of θ.

The rotation number and the Lyapunov-exponent are shown in figure 2.4. The rotation number grows monotonously and remains constant in windows where a nondegenerate periodic point is present. The features of this graph, with a rapid increase of ρ just before and after an interval on which it is constant and many intervals in which ρ is constant, are also known as ‘devil’s staircase’. The Lyapunov exponent is nearly zero in the regions where the

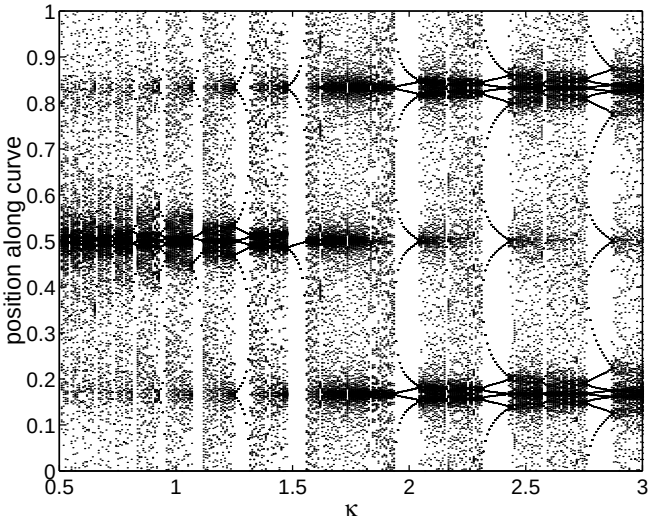

Figure 2.3: Poincaré plot for $\varepsilon = 1.82$.Position on Γ of last 200 reflections out of 1000.

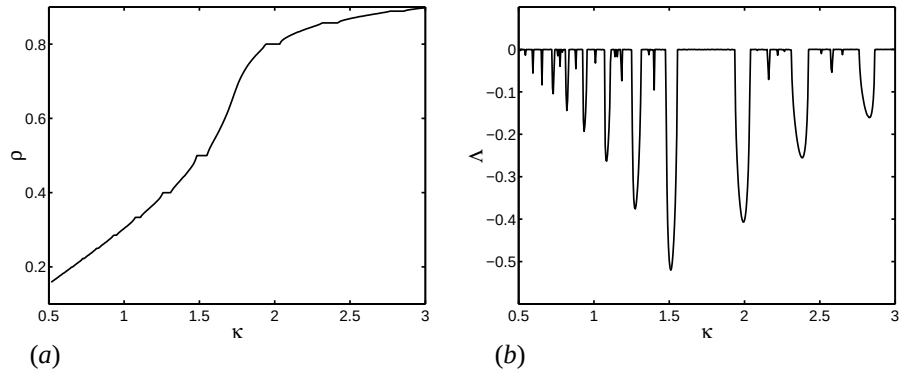

(*a*) (*b*)

Figure 2.4: *(a)* Rotation number and *(b)* Lyapunov exponent for $\varepsilon = 1.82$.

orbits are quasiperiodic or neutrally periodic and negative where the attractor exists. There is no interval on which $\Lambda > 0$.

It is remarkable that in figure 2.3 in the interval $1.6 < \kappa < 1.9$ no window with attractor is detected. This coincides with a relatively rapid increase of ρ in figure 2.4(a). In this interval the Lyapunov exponent (figure 2.4b) is nearly 0 and the minima of Λ become less deep again for $\kappa > 1.9$. This behaviour is due to the presence of a standing wave mode (all characteristics reflect back onto themselves) for $\kappa = \sqrt{3}$. In section 2.4, where more special orbits will be treated, we will see that the standing mode behaviour for $\kappa = \sqrt{3}$ occurs for all values of ε.

To compare and to investigate what the role of ε is we will also show results for other

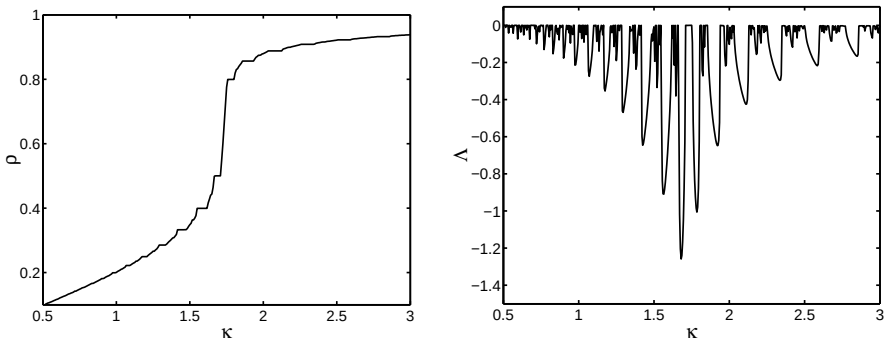

Figure 2.5: *(a)* Rotation number and *(b)* Lyapunov exponent for $\varepsilon = 1.98$.

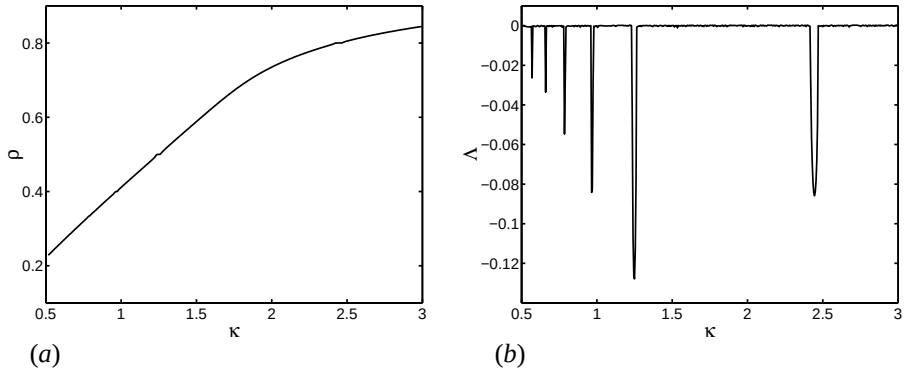

Figure 2.6: *(a)* Rotation number and *(b)* Lyapunov exponent for $\varepsilon = 1.33$.

values of ε. We start with $\varepsilon = 1.98$, a parameter value for which the curve is close to a triangle. The plots of ρ and Λ are in figure 2.5. As compared to the results for $\varepsilon = 1.82$ there are more and smaller intervals in which an attractor exists. The rotation number has a wider range for the same interval of κ-values. Also the negative peaks for the Lyapunov exponent are deeper and narrower. The interval around $\kappa = \sqrt{3}$, where no attractor is found numerically, is very small.

Figure 2.6 shows results for $\varepsilon = 1.33$. In this case less attractor windows are visible than for $\varepsilon = 1.82$. The curve for the rotation number is monotonously increasing with just a few small intervals on which it is constant. Also the range of ρ is smaller than for $\varepsilon = 1.82$ on this scale, although for the full range of Λ all values $0 < \rho < 1$ must be adopted. The structure of the Lyapunov exponent curve is very simple with just a few negative peaks. This is in sharp contrast with the abundance of structure for $\varepsilon = 1.98$. The depth of the peaks in κ for $\varepsilon = 1.98$ and $\varepsilon = 1.33$ differs by almost a factor 10. There is no attractor detected in a relatively wide range of κ around $\kappa = \sqrt{3}$.

The behaviour of the map is self-similar in the sense that when part of the plot is enlarged,

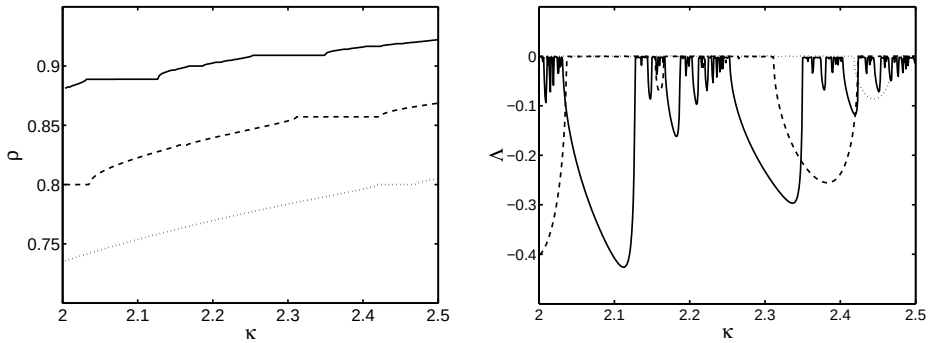

Figure 2.7: *(a)* Rotation number and *(b)* Lyapunov exponent for $\varepsilon = 1.98$ (solid line), $\varepsilon = 1.82$ (dashed line) and $\varepsilon = 1.33$ (dotted).

it will show the same features as the 'original' plot, just on a different scale. This is illustrated in figure 2.7 where ρ and Λ are plotted for all three values of ε. Especially for $\varepsilon = 1.98$ the self-similarity is clear. Between two relatively large scale attractors a pattern arises that is similar to the original picture, with smaller and larger scale attractors, the Lyapunov exponent peaks becoming deeper and less deep again. If we enlarge part of the enlarged section we again find this structure. The structure of the enveloping line is reproduced also. On every scale we find patterns with the same structure. For $\varepsilon = 1.82$ the structure is also self-similar, but since the original picture did not show much structure in between the attractors we cannot expect different behavior (much small scale structure). The structure for $\varepsilon = 1.33$ is very plain again. If we enlarge strongly we can also discern small negative peaks for Λ in the interval around $\sqrt{3}$ where no attractor was visible in the original picture.

So far, the pattern of the dots in the Poincaré plot within a window with an attractor was continuous. We chose the starting point on the z-axis and the attractor shape was smoothly varying with the parameter value. However, if one chooses a random starting point (kept constant for the Poincaré plot), a discontinuity might arise in the Poincaré plot. An example is shown in figure 2.8. This occurs when the characteristics that are attracted towards one attractor are attracted to the mirror image of this former attractor for a slightly different value of κ. It happens very abruptly in parameter space and it can only occur for attractors that are not symmetric with respect to the z-axis themselves, but have a conjugate attractor that is its mirror image, like the period 2 attractor.

To summarize the results and sweep through the complete parameter space a picture is made which shows the strength of convergence for all parameter combinations. This is shown in figure 2.9. Instead of κ the angle $\pi/2 - \theta = \arctan\kappa$ was used. This is done in order to show the whole parameter space. The strength of convergence is indicated by $\log_{10}(-\Lambda)$. Regions of strong convergence can be beautifully recognized as broad 'tongues' at large values of ε, becoming very narrow at low values of ε and all bending towards $\arctan\kappa = \arctan\sqrt{3}$, which is the limiting value for all attractors at $\varepsilon = 2$. This is also the value for which the standing mode arises for all values of ε (black line). The tongue-like structures are called Arnol'd tongues, after Arnol'd (1965). Between the large scale tongues, corresponding

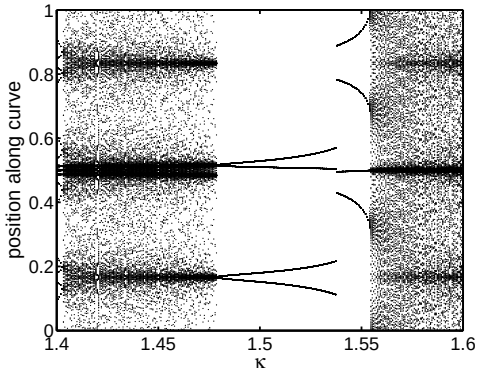

Figure 2.8: Discontinuity in Poincaré plot for $\varepsilon = 1.82$, characteristics start at $z = -0.6$ instead of at $z = z_{max}$ on the z-axis.

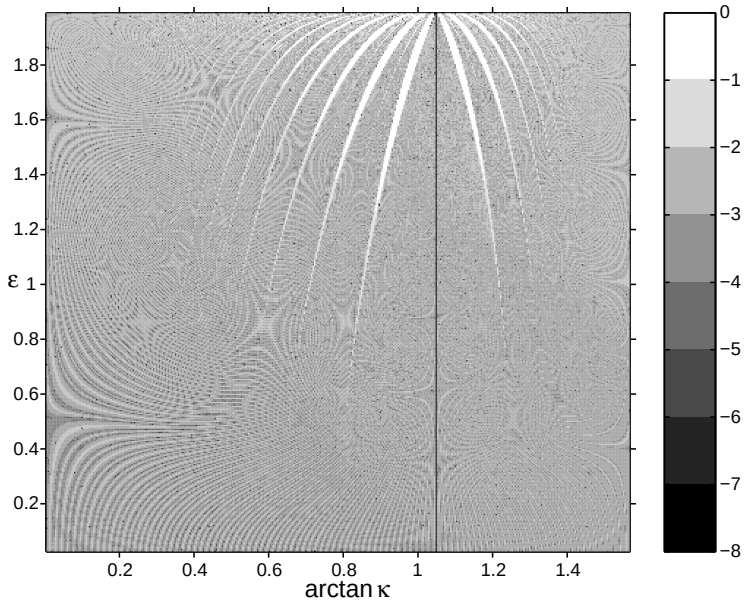

Figure 2.9: Strength of convergence $\log_{10}(-\Lambda)$ of characteristics for the whole parameter space.

to the major peaks in the Lyapunov exponent plots, there are smaller tongues corresponding to the smaller scale peaks. As stated earlier, because of the self-similarity of the structure for different scales, there must be an infinite number of smaller scale tongues. However, they are not resolved here, both because of the spatial scale of the plot and because the value of Λ becomes very small. Outside the tongues there is an interference pattern, known as Moiré pattern. This is due to the finite resolution and not a feature of the map itself.

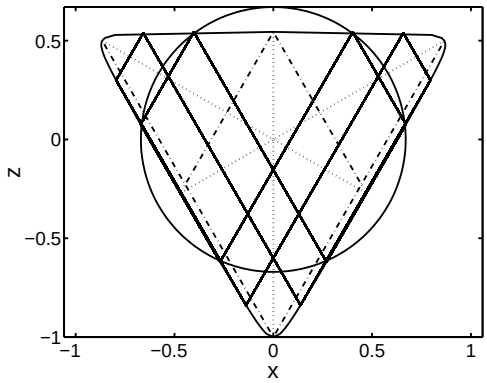

Figure 2.10: Standing wave mode, $\kappa = \sqrt{3}$. The axes of symmetry are dotted, the special characteristics, connecting the critical points in pairs, are dash-dotted, solid lines are two arbitrary periodic characteristics. The circle, centered at the origin, connects the reflection points at the boundary of a single periodic characteristic. For every characteristic in this standing wave mode such a circle can be drawn.

2.4 Special trajectories

As we have indicated before, a standing wave mode appears for $\kappa = \sqrt{3}$ for all values of ε. This can be explained by the symmetry of the curve, see figure 2.10. The curve has three axes of symmetry: the z-axis and the lines $z = \pm(1/\sqrt{3})x$. For $\kappa = \sqrt{3}$ all characteristics are orthogonal to the last two symmetry axes. The map can then be interpreted as a pure reflection in these two lines. For every single characteristic the boundary reflection points lie on a circle centered at the origin. There are two special orbits: one connecting the long axes of the curve (leading to the circle with largest diameter) and one connecting the short axes (leading to the circle with smallest diameter). These orbits connect the critical points. All characteristics intersect themselves on the z-axis.

There is an important difference in the behaviour of the characteristics for $\kappa < \sqrt{3}$ and $\kappa > \sqrt{3}$. For the triangle ($\varepsilon = 2$) we know that either the lower corner or the two upper corners act as attractor. For $\varepsilon < 2$ the curve has no real corners where the characteristics are trapped. But what we can observe is that for $\kappa < \sqrt{3}$ the characteristic reflects more often near the lower 'corner' whereas for $\kappa > \sqrt{3}$ the characteristic reflects more often in the two upper 'corners'. This is illustrated in figure 2.11 for two different period 5 attractors. The attractor for $\kappa < \sqrt{3}$ and $p = 2$, $\rho = 2/5$ has more reflections near the lower 'corner', the one for $\kappa > \sqrt{3}$, $p = 4$, $\rho = 4/5$ has more reflections near the upper 'corners'. Both attractors correspond to large peaks of Λ.

We also want to investigate the structure of the windows and the role of symmetric orbits and critical characteristics. In figure 2.12 the periods of the strongest attractors are indicated. Only the period 4 attractor for $\kappa > \sqrt{3}$ is not visible, as it is weak and its interval of existence is extremely small. In Table 2.1 the corresponding properties are indicated for increasing value of κ. Figure 2.13 illustrates the paths of the characteristics at the boundary of the window for an odd and an even period window. It appears that windows with symmetric

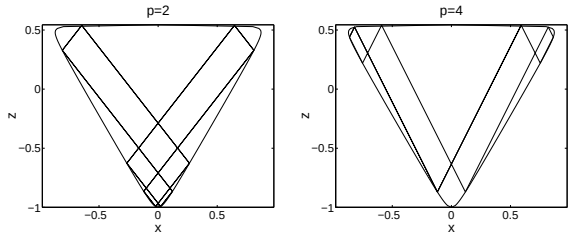

Figure 2.11: Two attractors with the same period (q =5) but a different location. For $\kappa = 1.28, p = 2$, reflection occurs mainly near lower 'corner', for $\kappa = 1.99, p = 4$, reflection occurs mainly near two upper 'corners'.

attractors (odd periods) are bounded by values of κ for which two (symmetric) critical points are mapped onto each other, on one boundary the upper, on the other boundary the lower. Windows with asymmetric attractors (even period) are bounded on one side by a value of κ for which two (asymmetric) critical points are mapped onto each other. On the other side, the two coexisting asymmetric attractors, that are each other's mirror image, merge into one single periodic orbit.

At the boundaries of the windows, there are no singularities or jumps in Λ. It smoothly goes to zero, attraction is no longer exponential but algebraic. Because the two asymmetric attractors are attractors for opposed sense of the map, it seems natural that attraction is cancelled when they merge. Similar behaviour was observed for the spherical shell Rieutord *et al.* (2001), when the attractor reflects at the inner sphere at the equator. This also corresponded to the merging of two coexisting attractors that are each other's mirror images with respect to the equator.

Table 2.1 and figure 2.12 also illustrate the difference in the ordering of the windows for κ larger and smaller than $\sqrt{3}$. The properties of the attractors are in a sense symmetric around $\kappa = \sqrt{3}$. But the ordering of the periods of the windows is different. For $\kappa < \sqrt{3}$ the periods of the largest windows, starting from the large period 2 windows, are 2, *5*, 3,*7*, 4, *9* ... For $\kappa > \sqrt{3}$ it is a continuously increasing series with the odd periods for the large windows and the even periods for the smaller windows.

Smaller peaks in between the large peaks in figure. 2.12 correspond to attractors of rather low period, but higher than the adjacent large windows (for example the period 9 and 7 attractors in between the period 2 and the period 5 attractor). The characteristics have a more complex reflection pattern than the characteristics that belong to the large windows. The even smaller peaks have intermediate period like 25 at $\kappa = 2.648$. But again these smaller windows are bounded by characteristics connecting the critical points or forming a symmetric orbit.

2.5 Breaking of basin symmetry

We investigated the role of symmetry breaking with respect to the z-axis. This was effectively done by rotating the curve around the origin by 0.15 rad. The angle of rotation was chosen such that it is not a rational fraction of 2π, but apart from this the exact value is rather arbitrary.

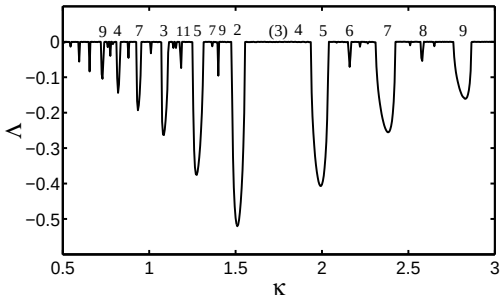

Figure 2.12: Lyapunov exponent for $\varepsilon = 1.82$ with indication of the periods of the attractors and the standing wave.

q	p	symmetric	κ_{min}	κ_{max}
9	2	yes	C-C	c-c
4	1	no	C-c	sym
7	2	yes	C-C	c-c
3	1	no	C-c	sym
5	2	yes	C-C	c-c
2	1	no	C-c	sym
3	2	-	-	-
4	3	no	sym	C-c
5	4	yes	C-C	c-c
6	5	no	sym	C-c
7	6	yes	C-C	c-c
8	7	no	sym	C-c

Table 2.1: Typical properties of the strongest attractors regarding their symmetry and their structure at the beginning and end of their window of existence. The c means that the periodic orbit starts and ends in critical points: C indicates a critical point in the upper part of the curve, c in the lower. If the end of the window consists of a symmetric attractor formed by the merging of two asymmetric attractors this is denoted by 'sym'.

The characteristics remain symmetric with respect to the vertical axis. The rotation number is plotted in figure 2.15. The strength of convergence over the whole parameter space is shown in figure 2.14.

The results look similar to the results with symmetry. The most striking difference is the absence of the standing wave mode. When we look in more detail and inspect the plot of the rotation number, we also note that the ordering of the periods of the attractors is different. With the period 2 window somewhere in the middle of the parameter space again, the periods of the attractors in the major windows have period 3,4,5,6... for increasing and decreasing values of κ. Like in the case with symmetry, the critical points play an important role in defining the beginning and end of a window in parameter space. The windows with attractors

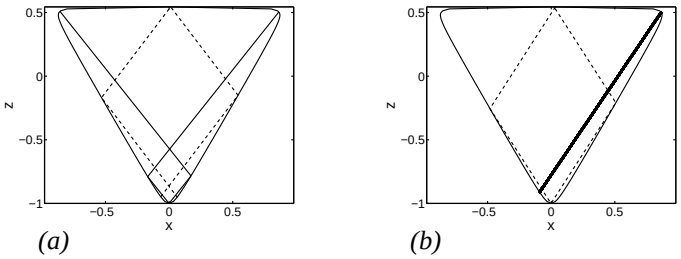

Figure 2.13: Periodic characteristics that determine the boundary of a window: solid characteristics belong to the beginning of the window, dashed characteristics to the end of the window. *(a)* Period 5 window (p=2). *(b)* Period 2 window.

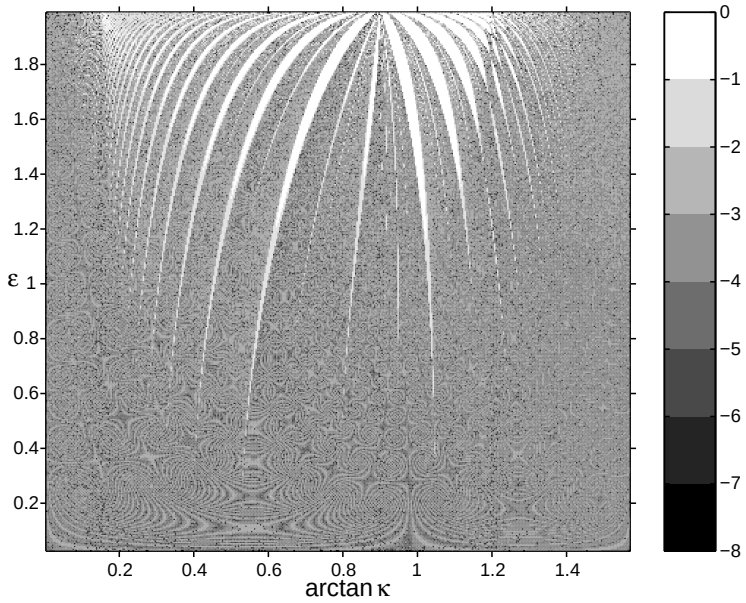

Figure 2.14: Strength of convergence of characteristics over whole parameter space. The curve is rotated over 0.15 rad to break the original axial symmetry.

with even period begin and end where critical points with the same tangent slope are mapped onto each other. The windows with odd period attractors begin and end where critical points with different tangent slope are mapped onto each other.

2.6 Perturbed circle

In this section we consider the dynamics of a composition of two reflections for a general perturbation of the circle. A criterion is derived that states if attractors are present or not at

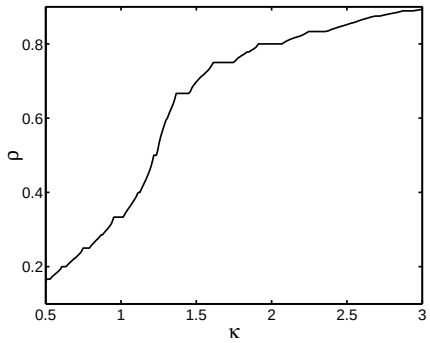

Figure 2.15: Rotation number for $\varepsilon = 1.82$, curve rotated over 0.15 rad.

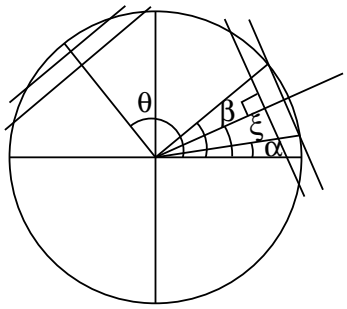

Figure 2.16: Illustration of composition of two reflections for the circle. Reflection of characteristics in lines that make an angle ξ and θ with the positive horizontal axis.

first order of the perturbation.

For the circle, the composition of two reflections is a rotation. Consider the circle with radius equal to one. The coordinate on the boundary is represented by α, with $0 \leq \alpha < 1$. The characteristics reflect in lines that make an angle ξ and θ with the horizontal axis. The situation is illustrated in figure 2.16. The involution with respect to ξ, denoted by $i_\xi(\alpha)$, maps α into $\beta = 2\xi - \alpha$ and $i_\theta(\alpha) = 2\theta - \alpha$. The composition $i_\theta(i_\xi(\alpha))$ yields $2(\theta - \xi) + \alpha$. The dynamics of the map is either periodic ($(\theta - \xi)/\pi = p/q$, period q) or quasiperiodic ($(\theta - \xi)/\pi$ irrational).

Now we consider perturbations to the unit circle. The radius varies with α according to $r_\varepsilon(\alpha) = 1 + \varepsilon r_1(\alpha) + \ldots$, the circle is parameterized by $(r_\varepsilon(\alpha)\cos(2\pi\alpha), r_\varepsilon(\alpha)\sin(2\pi\alpha))$. First, the effect of a perturbation on a single reflection is investigated. We denote $i_{\varepsilon,\xi}(\alpha)$ by β and expand:

$$\beta = i_{\varepsilon,\xi}(\alpha) = i_{0,\xi}(\alpha) + \varepsilon \frac{\partial}{\partial \varepsilon} i_{\varepsilon,\xi}(\alpha)|_{\varepsilon=0} + \ldots \approx 2\xi - \alpha + \varepsilon\beta_1 \tag{2.12}$$

An extra index ε was introduced to i to discern the perturbed and unperturbed case. The first order term β_1 can be calculated as follows. Reflection in the line $z = \tan(\xi)x$ implies that β

must satisfy

$$r_\varepsilon(\alpha)\cos(2\pi(\xi-\alpha)) = r_\varepsilon(\beta)\cos(2\pi(\beta-\xi)) \tag{2.13}$$

which relates the projections of $z = \tan(\alpha)x$ and $z = \tan(\beta)x$ on this line. The expansion (2.12) is substituted and both sides are differentiated with respect to ε in $\varepsilon = 0$. With the definition

$$\sigma_1(\alpha) = \frac{\partial r_\varepsilon(\alpha)}{\partial\varepsilon}|_{\varepsilon=0}$$

the expression for β_1 is given by

$$\beta_1 = \frac{1}{2\pi}\left(\sigma_1(2\xi-\alpha) - \sigma_1(\alpha)\right)\cot(2\pi(\xi-\alpha)) \tag{2.14}$$

With this result we can proceed to consider the composition of two reflections. To simplify things without loss of generality, ξ is set equal to 0 so that $i_{0,\xi}(\alpha) = i_{0,0}(\alpha) = -\alpha$. The orientation preserving map is defined by $T_{\varepsilon,\theta}(\alpha) = i_{\varepsilon,\theta}(i_{\varepsilon,0}(\alpha))$. We consider the composition $T^q(\alpha)$

$$T_{\varepsilon,\theta}(\alpha) = \alpha + 2\theta + \varepsilon\frac{\partial T(\alpha)}{\partial\varepsilon}|_{\varepsilon=0} + O(\varepsilon^2) \tag{2.15}$$

$$T^q_{\varepsilon,\theta}(\alpha) = \alpha + 2q\theta + \varepsilon\frac{\partial T^q(\alpha)}{\partial\varepsilon}|_{\varepsilon=0} + O(\varepsilon^2) \tag{2.16}$$

We choose $2\theta = p/q$ so that $T^q_{0,\theta}(\alpha) = \alpha$, the identity, and p and q must have no common factors, $q > p$. We define $\tau_{1,\theta}(\alpha) = \frac{\partial T(\alpha)}{\partial\varepsilon}|_{\varepsilon=0}$. It can be calculated using the expressions for β_1:

$$\begin{aligned}\tau_{1,\theta}(\alpha) &= \beta_{1,\theta}(-\alpha) - \beta_{1,0}(\alpha)\\ &= \frac{1}{2\pi}(\sigma_1(2\theta+\alpha) - \sigma_1(-\alpha))\cot(2\pi(\theta+\alpha))\\ &\quad + \frac{1}{2\pi}(\sigma_1(-\alpha) - \sigma_1(\alpha))\cot(2\pi\alpha)\end{aligned} \tag{2.17}$$

We further can use that $T^j_{0,\theta} = \alpha + jp/q$ and $\frac{\partial T_{0,\theta}}{\partial\alpha} = 1$. This gives

$$\begin{aligned}\frac{\partial T^q}{\partial\varepsilon}|_{\varepsilon=0} &= \tau_1(\alpha + \frac{(q-1)p}{q}) + \tau_1(\alpha + \frac{(q-2)p}{q}) + \ldots + \tau_1(\alpha)\\ &= \sum_{j=0}^{q-1}\tau_1(\alpha + j\frac{p}{q})\end{aligned} \tag{2.18}$$

We have to determine $\frac{\partial T^q}{\partial\varepsilon}|_{\varepsilon=0} (= \tau^q_{1,\theta}(\alpha))$ for a general form of the first order perturbation to the unit circle $\sigma_1(\alpha)$. Because $\sigma_1(\alpha)$ is periodic of period 1, it can be expressed as a Fourier series.

$$\sigma_1(\alpha) = a_0 + \sum_{k=1}^{\infty} a_k\cos(2\pi k\alpha) + \sum_{k=1}^{\infty} b_k\sin(2\pi k\alpha).$$

Then the expression for $\tau^q_{1,\theta}(\alpha)$ becomes, after a long but straightforward calculation in which the complex representation of a Fourier series was used,

$$\begin{aligned}\tau^q_{1,\theta}(\alpha) =& \frac{q}{\pi}\sum_{l\geq 1}\{b_{2l}(\cos(2\pi l\frac{p}{q})-1)+a_{2l}\sin(2\pi l\frac{p}{q})\}\\ &-\frac{2q}{\pi}\sum_{m=1}^{\infty}\sum_{l\geq 1}\{b_{2l+mq}(\cos(2\pi l\frac{p}{q})-1)\\ &\qquad +a_{2l+mq}\sin(2\pi l\frac{p}{q})\}\cos(2\pi mq\alpha)\end{aligned} \tag{2.19}$$

If $T^q_{\varepsilon,\theta}(\alpha)=\alpha$ has solutions for a finite number of values α, then there are attractors (or repellors) for these values of α. Since we explicitly chose θ such that $T^q_{0,\theta}(\alpha)=\alpha$, we can state that there are attractors (or repellors) if $\tau^q_{1,\theta}(\alpha)=0$ for a finite number of values α.

However, if $\tau^q_{1,\theta}(\alpha)=0$ holds for all values of α the theory is inconclusive. This holds for example for curves of which $\sigma_1(\alpha)$ does not contain Fourier coefficients of period four or higher. In such case, Arnol'd tongues may narrow stronger than linearly in ε (as is the case in Arnol'd (1965)) and it is necessary to extend the analysis to a higher order. Alternatively the solution can be a standing mode. This notion puts a limitation to the practical value of the theory. But the theory clearly shows that for a variety of smooth geometries of a basin, attractors are possible, even with a tongue opening linearly in ε. Therefore the effect of corners turns out not to be crucial.

2.6.1 Application to ellipse and third degree curve

For the ellipse the radius r can be expressed as

$$\begin{aligned}r_\varepsilon(\alpha) &= \sqrt{1-\varepsilon\sin^2 2\pi\alpha}\\ &\approx 1-\varepsilon\frac{1}{4}(1-\cos 4\pi\alpha)\end{aligned} \tag{2.20}$$

with ε equal to the squared eccentricity. This yields nonzero Fourier coefficients a_0 and a_2 only and τ^q_θ equals zero. So there is not a finite number of solutions for α for which τ^q_θ=0. This correctly represents the fact that the ellipse does not allow for wave attractors Franklin (1972); either all characteristics are periodic or no characteristic is periodic. Therefore, higher order tems in the perturbation series would yield zero also. In fact the ellipse is equivalent to the circle, there is a linear transformation that maps the ellipse to the circle and the parallel characteristics get a slightly different orientation but remain parallel.

Equation (2.19) is also applied to the third degree curve. For the third degree curve the radius of the convex part follows from

$$1-\frac{1}{3}\varepsilon = r^2-\varepsilon r^3(\sin(2\pi\alpha)\cos^2(2\pi\alpha)-\frac{1}{3}\sin^3(2\pi\alpha)). \tag{2.21}$$

This results in the approximation

$$r(\alpha) \approx 1 + \varepsilon(-\frac{1}{6} + \frac{1}{6}\sin 6\pi\alpha) \tag{2.22}$$

which has the nonzero Fourier coefficients a_0 and b_3 for $\sigma_1(\alpha)$. This gives $\tau_\theta^q = 0$ also. From closer inspection of (2.19) it follows that $\sigma_1(\alpha)$ must contain at least period four terms (a_4 or b_4 unequal to zero) in its Fourier expansion. If not, τ_θ^q does not depend on α. If we directly take characteristics parallel to the x- and z-axis, we find a standing mode of period 2 due to the symmetry of the curve in the z-axis.

Still we know from the previous results that attractors are indeed present. The numerically obtained figure showing Arnol'd tongues (figure 2.9) suggests that these tongues are not a first order effect but must be sought in higher order. To avoid elaborate general second order analysis we restrict ourselves to second order analysis of the period two attractor. Also, it is necessary to rescale and reorientate the curve in order to fit the curve in the conventions of this theory.

First we derive the expression for $\partial^2 T^2_{\varepsilon,\theta}(\alpha)/\partial\varepsilon^2|_{\varepsilon=0}$, which will be denoted by $\tau^2_{2,\theta}(\alpha)$ for convenience. The expression for β (2.12) can be extended with the next term in the Taylor expansion, $\beta \approx 2\xi - \alpha + \varepsilon\beta_1 + \varepsilon^2\beta_2$, with

$$\beta_2 = \frac{\partial^2 i_{\varepsilon,\xi}(\alpha)}{\partial\varepsilon^2}|_{\varepsilon=0}.$$

In order to determine β_2 expression (2.13) must be differentiated twice with respect to ε and evaluated in $\varepsilon = 0$. With the definition

$$\sigma_2(\alpha) = \frac{\partial^2 r_\varepsilon(\alpha)}{\partial\varepsilon^2}|_{\varepsilon=0}$$

this yields

$$\begin{aligned}\beta_2 =& \frac{1}{4\pi}\cot 2\pi(\xi-\alpha)\Big(\sigma_2(2\xi-\alpha) - \sigma_2(\alpha) - 4\pi^2\beta_1^2 + 2\beta_1\frac{\partial\sigma_1(\alpha)}{\partial\alpha}|_{2\xi-\alpha}\Big)\\ &- \beta_1\sigma_1(2\xi-\alpha)\end{aligned} \tag{2.23}$$

The term $\tau^2_{2,\theta}(\alpha)$ can be determined by straightforward differentiation of the composition $i_{\varepsilon,\theta}(i_{\varepsilon,0}(i_{\varepsilon,\theta}(i_{\varepsilon,0}(\alpha))))$. Using the expressions for β_1, β_2 and $\tau_{1,\theta}(\alpha)$, this can be expressed as

$$\begin{aligned}\tau^2_{2,\theta}(\alpha) =& \beta_{2,\theta}(-2\theta-\alpha) + 2\beta_{1,0}(2\theta+\alpha)\frac{\partial\beta_{1,\theta}(\alpha)}{\partial\alpha}|_{-2\theta-\alpha} - \beta_{2,0}(2\theta+\alpha)\\ &+ 2\tau_{1,\theta}(\alpha)\frac{\partial\tau_{1,\theta}(\alpha)}{\partial\alpha}|_{2\theta+\alpha}\\ &+ \beta_{2,\theta}(-\alpha) + 2\beta_{1,0}(\alpha)\frac{\partial\beta_{1,\theta}(\alpha)}{\partial\alpha}|_{-\alpha} - \beta_{2,0}(\alpha)\end{aligned} \tag{2.24}$$

For the circle, in the above notation with $\xi = 0$, the angle θ is $1/4$ and the characteristics are parallel to the x- and z-axis. The problem of the third degree curve was however consequently put in terms of two characteristics with opposed slopes, and only in the limit for

small ε the characteristics belonging to the period two attractor become orthogonal. In order to use the first order analysis and extend it to a second order analysis we have to translate our problem to the appropriate coordinate system with one reflection in $\xi = 0$ and one in $\theta = 1/4$.

In the limit case $\varepsilon = 0$ the characteristics, belonging to period two, do have $\kappa = \pm 1$ and are perpendicular. The curve only needs to be rotated over $\pi/4$ to be in the right coordinate system. However, as soon as $\varepsilon > 0$ the tongue bends away from $\kappa = 1$. In order to have perpendicular characteristics for the period two attractor we rescale the curve by replacing x by $(1 - C\varepsilon^2)x$. The values of C for which the tongue is found will follow from the analysis. Polar coordinates are introduced and the curve can be rotated over $\pi/4$. This results in the expression

$$\begin{aligned} r_\varepsilon(\alpha) =& 1 + \varepsilon\left(-\frac{1}{6} - \frac{1}{12}\sqrt{2}(\cos 6\pi\alpha + \sin 6\pi\alpha)\right) \\ &+ \varepsilon^2 \frac{1}{144}\left(3 + 72C + 72C\sin 4\pi\alpha + 4\sqrt{2}(\cos 6\pi\alpha + \sin 6\pi\alpha) + 5\sin 12\pi\alpha\right) \\ &+ O(\varepsilon^3) \end{aligned} \tag{2.25}$$

Substituting this expression in (2.24) yields a periodic function for $\tau^2_{2,\theta}(\alpha)$. In figure 2.17(a) this function is plotted for $C = 0.2$. It has 8 zeros for approximately the interval $0.06 < C < 0.3$, representing the two periodic orbits (attractors). For $C < 0.06$ the function is completely positive, for $C > 0.3$ completely negative. So we found the boundaries of the Arnol'd tongue belonging to the period two attractor to be $\kappa \approx 1 + 0.06\varepsilon^2$ and $\kappa \approx 1 + 0.3\varepsilon^2$. In figure 2.17(b) the boundaries of the Arnol'd tongue are plotted together with results representing parameter values for which numerical convergence to a period 2 periodic orbit was reached. It can be compared with figure 2.9 around $\arctan\kappa = \pi/4$. Apparently the tongue, as described by the second order perturbation theory, is subject to narrowing for $\varepsilon > 0.02$. This was confirmed by calculating the boundaries of the tongue by numerically solving the values for which z_{max} and z_{min} are mapped onto each other by a single application of the map, and the values for which the two critical points are directly mapped onto each other. These special trajectories are known to form the boundaries of the period two window for each value of ε from section 2.4.

2.7 Discussion

This study shows that smooth convex geometries bear the possibility of wave attractors. Even small (smooth) perturbations to the circle can lead to wave attractors, with an Arnol'd tongue with an opening that is linear in ε, provided that the perturbation can be described in Fourier components of period four or higher. So no singularities like corners or critical latitude singularities are needed. But for such period 4 perturbations it becomes hard to investigate the parameter space analytically, as expressions for ray tracing become difficult to handle.

For the third degree curve, the attractor only appears in the second order in the perturbation theory. But for this curve the expressions needed for ray tracing are easily obtained analytically, although when iteration of the map is involved a numerical approach is required. The parameter space was investigated in detail to study the structure of the windows with

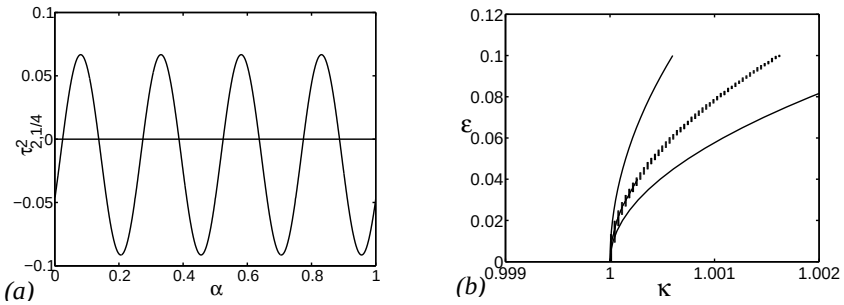

Figure 2.17: *(a)* $\tau^2_{2,1/4}(\alpha)$ for C=0.2. The eight zeros of the function correspond to the values of α on the two attractors. *(b)* Arnol'd tongue, bounded by $\kappa = 1 + 0.06\varepsilon^2$ and $\kappa = 1 + 0.3\varepsilon^2$. The vertical stripes indicate values for which convergence to a period 2 orbit was detected numerically.

attractors and the role of symmetry. Windows containing an attracting periodic orbit are bounded by parameter values that imply either periodic orbits connecting critical points, or imply a 'merging' of two attractors of the same period, that are each other's mirror image with respect to the z-axis in the rest of the window, resulting in a single z-symmetric attractor. The periodic orbits belonging to the boundary of a window are only weakly attracting, the Lyapunov-exponent vanishes. A single standing mode is detected, present for all values of ε and owing its existence to an additional symmetry of the system for this specific value of κ. This standing mode disappears when this symmetry is destroyed by rotation of the curve. Then the mirror-symmetry with respect to the z-axis is also broken, resulting in a different ordering of the windows regarding the period of the attractor.

For inertial waves in the spherical shell, windows with periodic orbits (attractors) are bounded by characteristics that touch the inner or outer sphere at the critical latitude (Israeli, 1972). The strength of these attractors was investigated by Rieutord *et al.* (2001). The Lyapunov exponent either vanishes or becomes $-\infty$ at the boundary of a window. It equals zero (only algebraic convergence) when the characteristic goes from the equator or pole of one sphere to the equator or pole of the other sphere, or to the critical latitude of the outer sphere. When the equator or the pole is part of the attractor, the attractor is symmetric with respect to the equator or the rotation axis, and will also be accompanied by the 'merging' of two attractors. When the characteristic reflects at the critical latitude of the inner sphere $\Lambda = -\infty$.

Also the structure of the parameter space of the parabolic basin with a horizontal surface (Maas & Lam, 1995) can be described by inspecting special characteristics. Windows of z-symmetric attractors are bounded by parameter values for which the corner is mapped to the other corner of the basin and values for which the two critical points are mapped onto each other. The windows with asymmetric attractors are bounded by values for which a corner and a critical point are mapped onto each other and by values for which the two asymmetric attractors come together in a single symmetric attractor. This is analogous to the third degree curve, where the corners are replaced by critical points.

For the bucket (Maas & Lam, 1995) the situation is different. The bucket is a trapezoid with flat top and bottom and two sloping walls of opposite constant slope. Windows with

symmetric attractors start with values of κ for which a characteristic joins the two upper corners and end with values of κ for which the two lower corners are mapped onto each other. Therefore reflections at the corners can be interpreted as critical reflections. The asymmetric attractors do not occur because focusing at one side wall is compensated by defocusing at the other side wall. All rays are periodic when this happens (standing mode) and in particular the upper corner is connected to the opposite lower corner.

The 'half bucket' with one sloping wall (Maas *et al.*, 1997) is closely related. A ray is focused towards a periodic orbit (attractor) that has an odd number of reflections at the sloping wall. When it has an even number of reflections at this wall, a downward, focusing reflection will always be balanced by a defocusing upward reflection so that no net focusing occurs. For the full bucket, focusing on one sloping wall is not compensated at the other sloping wall, but reinforced for a symmetric attractor, since also the sense in which characteristics travel is mirror symmetric. For the half bucket this corresponds to a connection from the upper corner of the sloping wall to the lower corner of the sloping wall. Thus the z-symmetry is not of essential importance for the existence of attractors or standing modes.

When comparing the structure of the variations of the Lyapunov exponent with κ in the different geometries mentioned above, it was noticed that, contrary to the other geometries, for the third degree curve the values of Λ varied smoothly. For the parabolic basin this was only the case at the beginning of a window, for the end of the window there was a jump from a finite value of Λ to 0. The continuous variation of Λ corresponds to the cases where the window is bounded by κ-values for which the true critical points are mapped onto each other or the attractor becomes symmetric, the jump corresponds to the boundary where the corner points are connected to each other or to a critical point. For the bucket shaped basin, indeed, both boundaries of the window are characterized by a jump in Λ. This indicates the singular nature of these corner points.

This chapter is accepted for publication in *Physica D* under the title "Wave attractors in a smooth convex enclosed geometry" by A.M.M. Manders, J.J. Duistermaat and L.R.M. Maas

Appendix: Lyapunov-Exponent

The distance between two parallel characteristics is not uniquely determined in terms of the periodic coordinate ϕ; it depends on which of the two sets of intersection points is chosen. This is illustrated in figure 2.18(a), where $d\phi_1 < d\phi_2$. The distance along the curve between the two parallel characteristics has the same problem. This makes these definitions of distance unsuitable to determine the Lyapunov exponent.

Therefore the perpendicular distance $\mathcal{D}$ between the characteristics is used. This also seems an appropriate choice from a physical viewpoint, where classically a beam of waves, emanating from a generation area is considered, and concentration of energy is related to the beam itself rather than to its contact area with the boundary. The ratio of the distance before and after application of the map T can be used to compute the Lyapunov-exponent, as will be shown here.

Figure 2.18(b) shows two characteristics, starting on boundary Γ at (x_1, z_1) and (x_2, z_2) and extrapolated outside the boundary. The line connecting (x_1, z_1) and (x_3, z_3) is horizon-

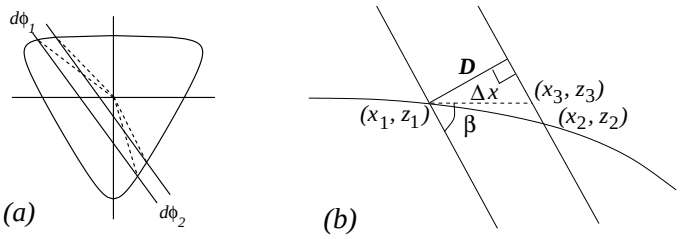

Figure 2.18: *(a)* The angular distance between two rays and the distance along the curve between two rays depends on the precise location of the intersections, here $d\phi_1 < d\phi_2$. *(b)* Part of the curve with two characteristics to illustrate the definitions in the derivation of the Lyapunov exponent.

tal, $z_3 = z_1$, the angle β is related to κ via $\beta = \arctan\kappa$. This gives for the perpendicular distance between the characteristics $\mathcal{D}$

$$\begin{aligned} \mathcal{D} &= \Delta x \sin\beta && \text{(A-1)} \\ &= (x_3 - x_1)\sin\beta && \text{(A-2)} \\ &= \left(\frac{z_1 - z_2}{-\kappa} + x_2 - x_1\right)\sin\beta. && \text{(A-3)} \end{aligned}$$

For a given value of z, the x-coordinate of a point on the curve is known from the parameterization of the curve, $x = \mathcal{F}(z)$ up to a sign, that can be found by selecting a specific point on the curve and characteristic to start with, and is taken into account in the computation of $\mathcal{F}$. Substitution leads to

$$\mathcal{D} = \left|\left(\frac{z_1 - z_2}{-\kappa} + \mathcal{F}(z_2) - \mathcal{F}(z_1)\right)\right|\sin\beta. \qquad \text{(A-4)}$$

The same procedure can be followed to find the distance between the characteristics through the points obtained by iteration of the map T for the points (x_1, z_1) and (x_2, z_2). The new points are denoted by their z-coordinate only, $z_{n+1} = T(z_n)$. The distance after applying the map is denoted by $\mathcal{D}_T$.

$$\mathcal{D}_T = \left|\left(\frac{T(z_1) - T(z_2)}{-\kappa} + \mathcal{F}(T(z_2)) - \mathcal{F}(T(z_1))\right)\right|\sin\beta. \qquad \text{(A-5)}$$

The quantity $\frac{\mathcal{D}_T}{\mathcal{D}}$ is closely related to the Lyapunov-exponent. If the quantity is larger than 1 the map defocused the two characteristics, if the quantity is smaller than 1 the map focused the characteristics. To derive the definition of the Lyapunov-exponent we proceed as follows.

We choose z_2 very close to z_1 so that we can write $z_2 = z_1 + \epsilon$. This results in

$$\frac{\mathcal{D}_T}{\mathcal{D}} = \frac{\left|\frac{T(z_1) - T(z_1+\epsilon)}{-\kappa} + \mathcal{F}(T(z_1+\epsilon)) - \mathcal{F}(T(z_1))\right|}{\left|\frac{\epsilon}{\kappa} + \mathcal{F}(z_1+\epsilon) - \mathcal{F}(z_1)\right|}. \qquad \text{(A-6)}$$

After multiplying numerator and denominator with $\frac{\kappa}{\epsilon}$ and considering the limit $\epsilon \to \infty$ we obtain the formula

$$\frac{\mathcal{D}_T}{\mathcal{D}} = \frac{\left|\frac{dT}{dz}|_{z_1} - \kappa \frac{d\mathcal{F}}{dz}|_{T(z_1)} \frac{dT}{dz}|_{z_1}\right|}{\left|1 - \kappa \frac{d\mathcal{F}}{dz}|_{z_1}\right|}. \tag{A-7}$$

If we apply this formula on and on for the successive iterations of the map T this gives the total divergence or convergence of the map. The definition of Λ as measuring the exponential 'separation' of two adjacent points (Schuster, 1984), here translated in terms of the distance between the rays, reads

$$\mathcal{D} e^{N\Lambda(z_0)} = \mathcal{D}_{T^N}. \tag{A-8}$$

This can be written as

$$e^{N\Lambda(z_0)} = \frac{\mathcal{D}_{T^N}}{\mathcal{D}_{T^{N-1}}} \frac{\mathcal{D}_{T^{N-1}}}{\mathcal{D}_{T^{N-2}}} \cdots \frac{\mathcal{D}_T}{\mathcal{D}}. \tag{A-9}$$

Note that individual $\mathcal{D}$-terms cannot be eliminated, since an expression for the *ratio* has been obtained (equation A-7) and individual distances have no meaning. Rewriting and taking the limit $N \to \infty$ yields an analogon for the 'classical' formula for the Lyapunov-exponent Λ

$$\Lambda(z_0) = \lim_{N\to\infty} \frac{1}{N} \sum_{n=1}^{N-1} \log \frac{\mathcal{D}_{T^n}}{\mathcal{D}_{T^{n-1}}}. \tag{A-10}$$

Chapter 3

Observations of inertial waves in a rectangular basin with one sloping boundary

3.1 Introduction

Fluids in solid-body rotation are stably stratified in angular momentum (see for example Greenspan, 1968*b*). In the same way that a fluid, stably stratified in density, can support internal gravity waves, a uniformly rotating fluid can carry inertial waves. These are sometimes called gyroscopic waves to distinguish them from the limiting case of inertial oscillations in a rotating, density stratified fluid, when the frequency equals twice the rotation frequency (LeBlond & Mysak, 1978). Inertial waves and internal waves share the property that their vertical direction of propagation is restricted. It depends on the wave frequency and, respectively, on the rotation rate and the strength of the stratification. They travel obliquely through the fluid, as shown experimentally by Görtler (1943) for internal waves and Oser (1958) for inertial waves. Owing to the strong analogy between inertial and internal waves for two-dimensional flow (Veronis, 1970), it is possible to investigate internal waves and thereby obtain information for inertial waves. This justifies that results for internal waves are included in the discussion. The most important difference between these waves is that internal wave particle motion is rectilinear, so that also in a three-dimensional container two-dimensional waves can be realized, whereas inertial wave particle motion is intrinsically two-dimensional (circular) due to the Coriolis force, which gives inertial waves a distinct three-dimensional character.

The restriction on the propagation direction has consequences for reflection. In general, the waves do not reflect according to Snell's law, but will be focused or defocused (Phillips, 1963), since parallel incident wave rays must remain parallel after reflection. The only exceptions are walls that are parallel or perpendicular to the rotation axis or the direction of gravity, for inertial and internal waves respectively. In an enclosed basin, if focusing is not balanced by defocusing, repeated reflection will lead to the appearance of a limit cycle. This

cycle is called the *wave attractor* (Maas & Lam, 1995) since all wave rays will approach this cycle. Here the wave energy is concentrated. But the wave rays will not actually reach the attractor in finite time (Greenspan, 1968*a*).

The notion of such 'pathological' behaviour in fluids is rather old. Görtler (1943), (1944) already mentioned that there might be regularity problems along the wave rays, which may disappear if viscosity is taken into account. Stern (1963), Bretherton (1964), Stewartson & Rickard (1969) and Stewartson (1971), (1972) found trapping of low frequency oscillations near the equator for a thin spherical shell, all using different concepts and approximations. Israeli (1972) found that this trapping does not occur for isolated frequencies but for continuous frequency intervals, bounded by frequencies for which reflection takes place at critical latitudes of the inner and outer sphere. Numerical models were used to further study the occurrence and behaviour of the wave attractors, and the structure of the shear layers that occur when viscosity is included in the model (Rieutord *et al.*, 2001).

The spherical shell is a geometry of special interest in geophysics (oceans, liquid outer core of the earth) and astrophysics (stars). But there are other geometries for which wave focusing towards a limit cycle takes place. A relevant case is an internal wave approaching a beach, represented by a wedge. If the bottom slope is less steep than the slope of the wave ray, the wave energy can be reflected up-slope. After repeated reflection at the surface and the bottom the wave approaches the corner of the wedge (Wunsch, 1969), which can then be interpreted as a (point) attractor. Maas & Lam (1995) investigated internal waves reflecting in different simple geometries and found various attractors for a parabolic basin and a trapezoidal basin ('bucket'). They also investigated the distribution of attractors in frequency space and found a self-similar structure with small frequency intervals with weak attractors in between the larger frequency intervals with stronger attractors.

The studies mentioned so far are purely theoretical work. In laboratory experiments one often works with basins in which no wave focusing takes place, with basin walls parallel or perpendicular to the axis of rotation or the direction of gravity. This reveals a discrete set of standing waves. Especially the rotating cylinder is a widely studied object. McEwan (1970) studied standing waves, corresponding quite well with inviscid linear predictions, but he also reported a resonant collapse for larger amplitudes, leading to disorder. Manasseh (1992) reports various breakdown mechanisms for standing waves in a rotating and precessing cylinder. Aldridge & Toomre (1969) observed standing inertial waves in a rotating sphere, a geometry for which focusing is balanced by defocusing.

Experiments in which internal gravity wave energy is attracted towards the corner of a wedge were carried out by Wunsch (1969) and Cacchione & Wunsch (1974). Greenspan (1968*a*) and Beardsley (1970) investigated this for inertial waves in a cone. Beardsley (1970) also observed inertial waves in a truncated cone. Such a geometry has the same cross section as the bucket described by Maas & Lam (1995) and enables focusing. Although Beardsley interpreted his results in terms of standing waves, they can be interpreted alternatively in terms of wave attractors, as will be argued in the discussion.

A visually clear experimental realization of an internal wave attractor that is really a limit *cycle* was done by Maas *et al.* (1997) in a rectangular tank with a sloping side wall for internal gravity waves. This is the most simple geometry to study wave focusing towards an attractor. That this also works for inertial waves in a homogeneous, rotating fluid was shown by Maas (2001).

In the present study, the experiments described in Maas (2001), where a single inertial wave attractor is observed, are extended. We use different forcing frequencies to generate attractors of different shape and one standing wave. The predicted boundaries of the frequency interval over which the most simple attractor exists are checked experimentally, and the difference with the standing wave will be illustrated. We took measurements at various horizontal and vertical cross sections to investigate the changes of the wave field in the horizontal direction.

The results by Maas (2001) already confirm that focusing towards an attractor, predicted by the two-dimensional theory, exists. However, because of the intrinsic three-dimensional nature of inertial waves, the finite extent of the basin is expected to influence the horizontal structure of the wave field. Since we have not been able to solve the Poincaré equation, that describes the full three-dimensional wave field (as is possible for a rectangular tank without sloping wall, Maas, 2003), we are depending on the experimental results to get insight in the three-dimensional structure. In the next sections, first the theory of inertial waves will be briefly outlined and the concept of a wave attractor is illustrated. Then the experimental set-up is discussed. To illustrate the attractor shapes, results of measurements in vertical cross sections are shown. Next, vertical cross sections at different positions are compared to study changes in the horizontal direction and a small selection of measurements in horizontal cross sections will be presented. Finally the results are discussed.

3.2 Theory

The basic equations governing a rotating, inviscid, homogeneous fluid are the momentum equations and the continuity equation. In this paper we will consider waves in a frame of reference that is nearly in solid body rotation. The angular velocity of the frame will be $\Omega = \Omega_0 + \epsilon\Omega_1(t)$, where $\epsilon \ll 1$ and Ω_0 is the background rotation rate while $\Omega_1(t)$ is its time periodic modulation. The strength of the periodic modulation determines the scale of the perturbations. The linearized momentum equations for the perturbation velocities and perturbation pressure then read

$$\begin{aligned} \frac{\partial u}{\partial t} &= 2\Omega_0 v + y\frac{\partial \Omega_1}{\partial t} - \frac{\partial p}{\partial x}, \\ \frac{\partial v}{\partial t} &= -2\Omega_0 u - x\frac{\partial \Omega_1}{\partial t} - \frac{\partial p}{\partial y}, \\ \frac{\partial w}{\partial t} &= -\frac{\partial p}{\partial z}, \end{aligned} \tag{1}$$

with u, v, w the perturbation velocity components in the x, y and z-direction with z parallel to the rotation axis. The gradient of the pressure P and gravitational and centrifugal forces form a dynamic equilibrium at zeroth order. In the linear equation, they are combined in the perturbation pressure term $p = P - (x^2 + y^2)\Omega^2/2 + \rho g z$, where ρ denotes the uniform density and g gravity.

The remaining right hand side terms due to rotation and modulation of the frame are the

Coriolis and Euler force respectively (Tolstoy, 1973). The continuity equation reads

$$\nabla \cdot \mathbf{u} = 0. \tag{2}$$

At solid boundaries the normal velocity of the fluid must vanish, leading to the boundary condition

$$\mathbf{u} \cdot \mathbf{n} = 0, \tag{3}$$

with $\mathbf{n}$ the inward normal.

In the experiments we are interested in the inertial wave field. The behaviour of these waves for a uniformly rotating fluid ($\Omega_1 = 0$) will be treated first, the generation of these waves via modulation of the angular frequency ($\Omega_1 \neq 0$) will be discussed afterwards.

3.2.1 Inertial waves

In this section we look at a free, monochromatic waves $\propto \exp(-i\omega t)$ of frequency ω in a uniformly rotating fluid with angular velocity Ω_0. Equations (1) can then be reduced to a single equation for the pressure:

$$p_{xx} + p_{yy} - \lambda^2 p_{zz} = 0, \tag{4}$$

with

$$\lambda^2 = \frac{4\Omega_0^2 - \omega^2}{\omega^2}. \tag{5}$$

This so-called Poincaré equation (Cartan, 1922) can be reduced to two dimensions by assuming an infinitely long channel in the y-direction and y-independent waves, so that derivatives with respect to y vanish. The resulting two-dimensional equation is a wave equation (hyperbolic equation) if $\omega < 2\Omega_0$. Note that, due to the Coriolis force, the *particle* motion itself does have a component in the y-direction, as can be seen from the linearized Euler equations (1).

For a very limited class of two-dimensional geometries, the equation can be solved using separation of variables. The boundaries must then be parallel or perpendicular to the rotation axis (rectangular), with the circle (or more general, the ellipse) as exceptions. The solution then reveals a discrete set of standing waves. For an arbitrary geometry one can use the method of characteristics. These characteristics correspond physically to rays along which the energy propagates (see Maas & Lam, 1995). Every characteristic carries information on the pressure on the boundary into the interior. Along a characteristic, the *partial pressure* (half the pressure on the boundary) is conserved. In a point in the interior, the pressure is the sum of the partial pressure values on each of the two characteristics through this point.

If one substitutes the plane wave solutions $p(x, z) = \mathcal{P} \exp i(kx + mz)$, the dispersion relation is

$$\frac{k}{m} = \pm\lambda \tag{6}$$

This shows that for a given frequency only four directions of propagation are possible. Phillips (1963) gives a very general treatment of the physics of these waves. Wave energy travels along characteristics (wave rays) $x \pm z \tan\theta = constant$, with $\tan\theta = 1/\lambda$ the slope of the group velocity vector with respect to the rotation axis. Lines of equal phase are parallel to these rays. The phase propagates in a direction perpendicular to the energy, with the horizontal component opposite to the horizontal direction of energy propagation.

Wave attractors

For reflection at boundaries parallel and perpendicular to the rotation axis, incoming and reflected waves are symmetric with respect to the normal of the boundary, and nothing special occurs. However, for an arbitrarily sloping wall, the symmetry with respect to the normal is broken because of the constraint on the direction of propagation. Hence waves will be geometrically focused or defocused. In an enclosed basin repetitive focusing can lead to the appearance of a 'wave attractor', a limit cycle where ultimately all wave energy ends, although not in finite time (Greenspan, 1968*a*). In figure 3.1(a) this is illustrated for the most simple case: a rectangular basin with one sloping side wall. This sloping side wall provides the possibility of wave focusing. Every time a wave ray reflects downwards from this wall it gets closer to the limit cycle, the central square. This limit cycle is the only periodic orbit for this frequency.

The period is defined as the number of reflections for this orbit to close onto itself. The total convergence or divergence along a wave ray is represented by the Lyapunov exponent Λ (Maas & Lam, 1995). Negative values indicate convergence, positive values do not occur for this system, since the parameter space is one-dimensional (Rieutord *et al.*, 2001). The value of Λ is proportional to $\log|(\lambda - s)/(\lambda + s)|$ for $s = H_0/B$ the slope of the wall. Its only singularities occur for $\lambda = \pm s$ when critical reflection causes immediate focusing and Λ goes to $-\infty$. Λ is inversely proportional to the period of the attractor (Maas & Lam, 1995).

A wave attractor exists over a parameter interval (figure 3.1b). Over this interval, the attractor gradually deforms, but the number of reflections at the boundary of the limit cycle is constant. The intervals are bounded by values for which the attractor degenerates, connecting two corners of the basin. Standing waves exist for isolated frequency values, when focusing is exactly balanced by defocusing. Then all wave rays return back onto themselves and Λ equals 0. They are surrounded by frequencies for which the attractor period approaches infinity and hence the Lyapunov exponent approaches zero.

We wish to study a number of patterns experimentally. The simplest attractor, which is called a (1,1)-attractor, since it has one reflection at the bottom and one reflection at the sloping wall, is investigated for several values in the frequency interval of its existence (window, interval II figure 3.1), including the limiting values. The corresponding shapes are illustrated in figure 3.2. On approaching the lowest value of $\tan\theta$, the (1,1)-attractor appears as a diagonal line from the upper left corner to the lower right corner. For the specific geometry with the bottom length being half the top length, this coincides with the frequency for which the wave rays are parallel to the slope, which results in a single V-shaped structure (figure 3.2a). This combination of attractors is called the 'critical slope' attractor and $\Lambda \rightarrow -\infty$ due to the immediate focusing at the wall. This immediate focusing at the sloping wall disables the

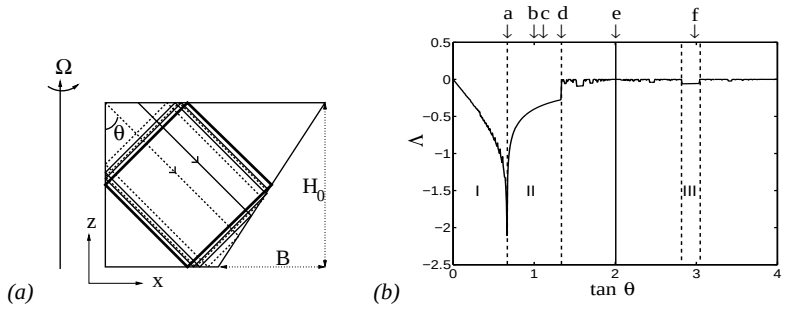

Figure 3.1: *(a)* Cross section of rectangular basin with sloping side wall. Two parallel wave rays (thin solid and dashed lines), making an angle θ with the rotation axis, reflect and their distance decreases (focusing). They approach a limit cycle (thick solid square) due to repeated focusing at the sloping wall. *(b)* Lyapunov exponent Λ as a function of the slope of the characteristics with respect to the rotation axis. It illustrates that wave attractors occur over an interval (window) in parameter space. Interval I: all wave rays are attracted towards the upper right corner. Interval II: (1,1)-attractor. Interval III: (1,3)-attractor. Solid line: (1,2) standing wave. The arrows and labels indicate the values of $\tan\theta$ for which experiments are carried out. The corresponding (attractor) shapes are shown in figure 3.2.

possibility of focusing towards the diagonal structure, but when the wave energy propagates parallel to the slope and reflects at the bottom it will travel along this diagonal. For increasing θ, the pattern changes towards a parallelogram, with the square (figure 3.2b) and self-similar (figure 3.2c) attractor as examples. The latter is called self-similar since reflection at the top and the bottom of the tank occurs at positions where the relative distances to the left and right corner are identical. The upper limit case is reached when the attractor degenerates into a single line connecting the upper right to the lower left corner (figure 3.2d).

The next simple closed structure has one reflection at the bottom and two reflections at the sloping wall (figure 3.2e). However, this (1,2)-structure is not an attractor. Focusing for the downward reflection at this wall is cancelled exactly by the other, upward, reflection. So every ray reflects back onto itself. The result is a standing wave mode of which the stream function consists of two (counterrotating) cells (figure 3.2h), separated by the line on which every ray intersects itself (dotted in figure 3.2e). This is in remarkable contrast with the square attractor, of which the stream function has patterns that are repeated but become extremely small close to the attractor (figure 3.2g). In figure 3.2(e), the characteristics connecting the corners of the basin are plotted (thick dashing); where they intersect there is no motion, these two points are the centres of the two cells. The other dashed line shows an arbitrary characteristic, returning back onto itself. This mode exists for a single, isolated frequency.

The most complicated structure that is studied is the (1,3)-attractor, which exists over a much smaller frequency interval than the (1,1)-attractor (interval III in figure 3.1b, shape illustrated in figure 3.2f). Convergence is weaker than for the (1,1)-attractors (Λ less negative), both due to the fact that focusing is weaker for this value of θ and due to the larger period.

In frequency space, in between these attractors all kinds of complicated weak attractors and standing modes exist, as illustrated by Maas *et al.* (1997) and as can be seen from figure 3.1(b). They will be more difficult to realize and observe experimentally. In general: the

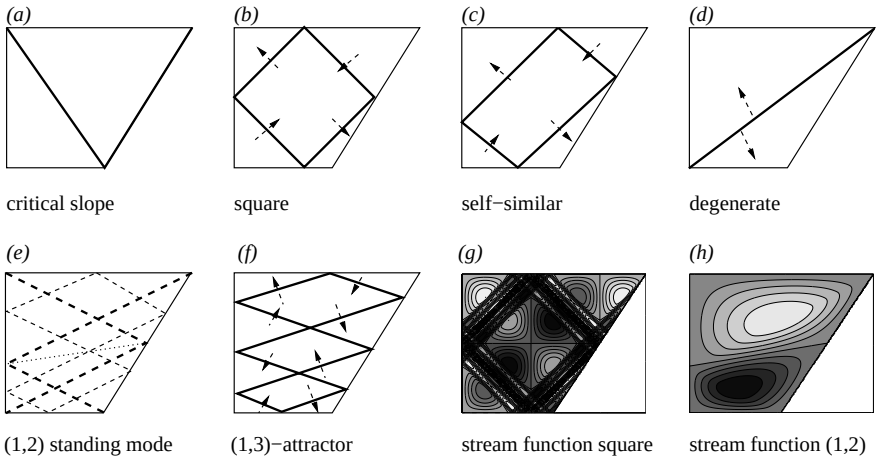

Figure 3.2: Shapes of the attractors and the resonant mode in terms of wave ray paths (solid lines) with direction of phase propagation indicated with arrows *(b, c, d, f)* and corresponding stream function of square attractor *(g)* and (1,2)-mode *(h)*. See text for more explanation.

more complex the structure, the weaker the attractor and the smaller the window in which it occurs.

Three-dimensional aspects

So far the inertial wave problem was reduced to a two-dimensional problem. It is extremely difficult to solve the inertial wave field in three dimensions. No general solution is available, one needs a simplifying argument like separation of variables (Stewartson & Rickard, 1969), which is only possible for a limited class of domain shapes (a cylinder (Kelvin, 1880), a sphere (Bryan, 1889) and a rectangular box (Maas, 2003)), and even then only when the main axes of the domain are parallel and perpendicular to the rotation axis.

Unlike for internal gravity waves, where particle motion is truly two-dimensional (rectilinear), there is particle motion in the y-direction due to the Coriolis force. Particles move anticyclonically along circles in planes along the characteristics $x \pm z \tan\theta = constant$. Only the projection of this motion on the xz-plane yields rectilinear motion for plane waves. In a finite basin, the two-dimensional structures must be modified by the front ($y = 0$) and end ($y = L$) wall in order to fulfill the boundary condition of no flow. This could result in a standing wave structure in the y-direction, if the wavelength in the y-direction matches the dimensions of the basin. It is also possible that waves travel along the attractor in the horizontal direction, thus describing a kind of helix through the basin.

A phenomenon that could be encountered is a combination of inertial Poincaré and Kelvin waves (Maas, 2003). These waves are the purely inertial counterparts of the conventional Poincaré and Kelvin waves, that are rotationally modified gravity waves (LeBlond & Mysak, 1978). Assuming standing waves in the vertical, in a rectangular tank inertial Poincaré and Kelvin waves combine to give patterns in the horizontal direction for eigenfrequencies of

the system. Typically modal structures were obtained, with regions moving in unison, and amphidromes, with phase lines circling around them. In the horizontal, particle motion is dominantly anticyclonic. The resulting patterns have small scale structures near the walls of the basin and increase in scale with increasing frequency. Whether these waves lead to similar structures in a basin with a sloping wall is still an open question.

3.2.2 Vorticity-conserving flow

In the previous section free waves were considered. In the experiments, these are generated via continuous, weak modulation of the rotation rate $\Omega_1(t) = \Omega_0 \sin \omega t$. The fluid, previously considered being in solid-body rotation, will react on changes in Ω by the generation of a vorticity-conserving horizontal flow (see appendix).

There are two mechanisms via which inertial waves are excited. Firstly, the horizontal vorticity-conserving flow has a component through the sloping wall, that will be compensated by the generation of waves. In a cylindrical container, this inviscid mechanism is not operating, since the vorticity-conserving flow would be everywhere parallel to the walls. In that case only the second generation mechanism applies: Ekman pumping and suction. The flow parallel to the boundaries generates Ekman layers in which fluid transport converges and diverges periodically, which generates waves (Greenspan, 1968*a*; Aldridge & Toomre, 1969).

The forced equations with time variations of the angular frequency form a system that is closely related to the spin-up problem of a container with a sloping bottom, that was studied by van Heijst *et al.* (1994). For a shallow tank ((height/length)^2 $\ll$1) the shallow-water approximation was used to enable the calculation of an analytical solution. This implies vertically uniform solutions, which is only an approximation of the actual flow field. However, the exact solution for the problem of a wedge shaped container shows that the flow is nearly vertically uniform for the ratio of height H_0 and length L in the tank that will be used in our experiments. This justifies the use of the shallow-water approximation.

Therefore, we solved the shallow-water equations for the basin with one sloping wall. This can be done without further approximations. The detailed derivation of the flow field can be found in the appendix. The resulting horizontal velocity field is plotted in figure 3.3. The pattern of the vorticity-conserving flow will change sinusoidally with time. To get absolute velocities, the expressions found in the appendix must be multiplied by a factor $A\bar{r}\sin\omega t$. Here $\bar{r}$ is the distance from the centre of the tank to the rotation axis and A an amplitude factor chosen to match the observed vorticity conserving flow. A appeared to be close to 1 (to within 20 percent for the various observations). The inviscid forcing mechanism appears particularly relevant near $y = 0$ and $y = L$ where the flow is predominantly cross-isobath.

We have not been able to explicitly link the vorticity-conserving flow and the inertial wave field. However, the inertial wave field in the vertical is expected to be dominated by wave attractors, whose location is independent of the forcing location and mechanism.

3.3 Experimental set-up

The experiments were carried out at the 13 m diameter rotating platform of the Coriolis Laboratory (Grenoble, France). The set-up is a larger version of the one described in Maas

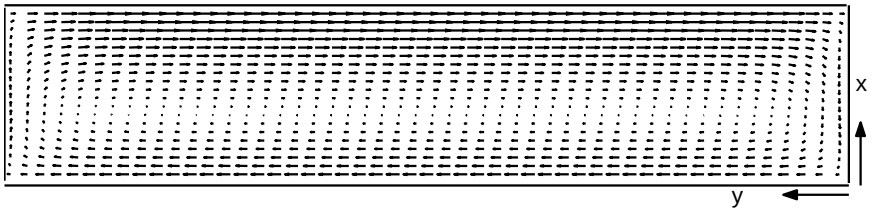

Figure 3.3: Calculated vorticity-conserving horizontal flow for the tank with sloping wall. The sloping part occupies the upper half of the figure. The centre of the flow cell is above the flat part of the bottom.

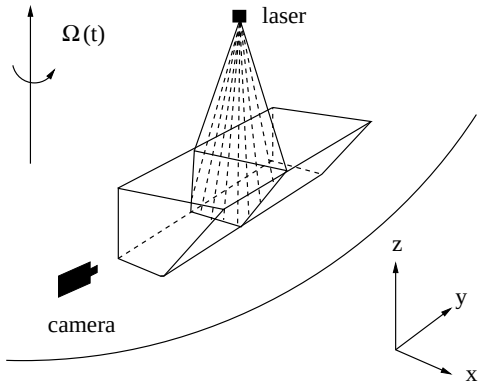

Figure 3.4: Schematic picture of experimental set-up

(2001). A schematic picture of the set-up is shown in figure 3.4. On the platform, a tank with size 107×500×80 cm^3 (width $2B$×length L×height H_0) was placed near the outer rim ($\bar{r} \approx 4$ m). A sloping wall was placed in the tank, reaching from the outer upper corner to half way the bottom (x=53.3 cm=B). The tank had a glass front and a lid consisting of glass plates of 100 cm width with metal strips around them. The tank was filled with ordinary tap water.

The platform was rotating with a background period of 48 s ($\Omega_0 = 0.13$ rad/s). To generate the waves of frequency ω, as indicated, the rotation speed was perturbed periodically with a small amplitude perturbation, $\Omega = \Omega_0(1 + \epsilon \sin \omega t)$. The amplitude of 8 cm/s of the modulation at the outer rim of the platform, relative to the background rotation velocity of 85 cm/s yields $\epsilon \approx 0.1$. The velocities of the vorticity-conserving flow have maximum values of about 1.5 cm/s relative to the rotating platform. In table 3.1 the employed modulation periods, the frequency ratio $\omega/2\Omega_0$ and $\tan\theta$ are given.

For visualization of the flow almost neutrally buoyant particles were added to the water. These were illuminated by a sheet of laser light of approximately 2 cm thick. The particles within this sheet were detected by a digital camera (768×484 pixels, frame rate 30 Hz). With Particle Image Velocimetry (Fincham & Spedding, 1997) the pictures taken by the camera were translated into velocity vector fields after every 90 frames, using a subset of these frames. The ultimate results of these measurements are series of two-dimensional

	name	period (s)	$\omega/2\Omega_0$	$\tan\theta$
a	critical slope	43.17	0.5558	0.6685
b	square	33.89	0.7092	1.0000
c	self-similar	32.24	0.7445	1.1150
d	degenerate	29.97	0.8006	1.3362
e	(1,2) standing	26.82	0.8950	2.0060
f	(1,3)	25.32	0.9481	2.9802

Table 3.1: Applied modulation periods and corresponding parameter values

velocity fields on a 62×46 grid with time intervals of 3 to 4 s, depending on the exact frame subset settings. Particle motion in the direction perpendicular to the laser sheet cannot be detected, so the vector fields represent a projection of the motion onto the plane. Measurements were taken in xz-planes ('vertical-cross sections') like illustrated in figure 3.4 and in xy-planes ('horizontal cross-sections') where the position of the laser and the camera were interchanged.

Measurements of vertical cross-sections were taken from y=0.60 to 210 cm; measurements closer to the front wall ($y = 0$) and further into the basin caused practical difficulties. Measurements of horizontal cross-sections cover only a small part of the tank. This is because the camera cannot cover more than about 80×100 cm^2 in the xy-plane, at the height where it was placed. The depth range of the measurements is from z=23 to 63 cm. Only for the self-similar and square attractor measurements were taken at two different y-positions.

For the vertical cross-sections a time series consists of 120 vector fields, so about 16 wave periods. For the horizontal cross-sections a time series consists of 200 vector fields, spanning about 25 wave periods. In order to observe the wave field in the horizontal cross-sections, the vorticity-conserving flow must be subtracted from the measurements. Using the theoretically predicted vorticity-conserving flow field with an experimentally determined amplitude factor, this otherwise dominant flow was accounted for. The vertical cross-sections are hardly affected by the vorticity-conserving flow, since for the locations of these cross-sections, this flow is mainly perpendicular to the xz-plane.

To compare cross-sections at different locations and for different forcing frequencies, they should have the same phase with respect to the forcing. This was not arranged automatically in the experiment. Therefore, the time series must be reordered such that every series starts with the same phase. For the horizontal cross-sections this can be done using the phase of the vorticity-conserving flow, which is easy to determine. In the vertical cross-sections the vorticity-conserving flow can hardly be observed and a different method is needed. We can use the idea that a horizontal and a vertical cross-section must show the same values for the u-component at their line of intersection, when these sections represent the same phase of the flow. One can determine for which time shift of the vertical time series the u-components on this line match those of the horizontal cross-sections. The time shift, combined with the well-determined phases for the time series of the horizontal cross-sections, results in a phase for the time series of the vertical cross-section. To increase the accuracy of this method (an error in the phase of 10-20 degrees is possible), a single vertical cross-section series was matched

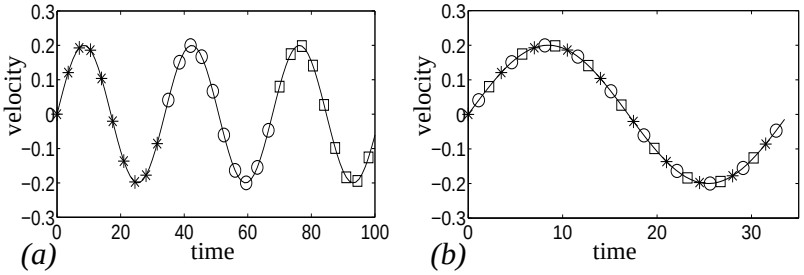

Figure 3.5: Example of asynchronous sampling and reorganization of data. *(a)* Synthetic time series. *(b)* The same data points, but reorganized with respect to the phase of the vorticity-conserving flow and with the application of asynchronous sampling.

with all the horizontal series available for the location. This gives fairly consistent results, except for the (1,3)-attractor and at y=60 cm for the (1,2)-mode.

Further the series can be reorganized such that instead of a long time series with few measurements per period one obtains a single period with high frequency sampling rate ('asynchronous sampling'). This is illustrated in figure 3.5 for synthetic data. It can only be used if the observed system is stationary and the motion has frequencies that are multiples of the modulation frequency. Then also frequencies that are higher than the original sampling frequency can be resolved and aliasing is prevented.

In addition to the PIV measurements, experiments with dye were done to observe the large scale flow. Also an experiment with a different forcing mechanism was done. The tank was not modulated but a paddle over the full length of the tank was oscillating in the upper left corner. Because of practical problems with the paddle, only a few experiments could be done.

3.4 Results

The first aim of the experiments was to find the theoretically predicted attractors. Therefore, we start with results from the vertical cross-sections. First, results for a fixed y-coordinate are shown to compare with the theoretically predicted patterns. Then the variation of these patterns with the y-coordinate will be discussed, with emphasis on the critical slope and the self-similar attractor. Finally the results for the horizontal cross-sections are presented.

All results will be presented in scaled coordinates. The x-coordinate is scaled with the half width $B = 53.5$ cm, the y-coordinate with the length of the tank $L = 500$ cm and the z-coordinate with the height $H_0 = 80$ cm.

3.4.1 Vertical cross-sections

Visualization of attractors

The results of PIV are vector fields. In these vector fields one can often observe relatively strong motion around the location of the theoretical attractor. But these vector fields are just

snapshots of time-varying motions, they do not fully represent the behaviour of the wave field. Furthermore, particle motion has a component of motion in a plane perpendicular to the plane of observation. So we measure only a projection of the motion.

To get an idea of the motion over a whole period, hodographs (lines joining the tips of the velocity vectors) were made. The asynchronous sampling method was used and seven vector fields with about the same phase were averaged. This can be justified since the motion appears to be nearly periodic; the forcing frequency is by far dominant in the spectrum. An example is plotted in figure 3.6(a). It illustrates that over a period, velocity vectors describe ellipses. On the attractor itself (see also figure 3.2c), these can be long and narrow, with the major axis aligned along the attractor. This is consistent with the theoretical prediction of circular motion with the other component of motion in a plane perpendicular to the plane of observation.

Where the attractor reflects from the boundaries, the motion is nearly circular, clockwise for reflection at the top and bottom, anticlockwise at reflection at the straight and sloping side walls, except at the wall itself where it must be parallel to the wall. This pattern can be explained by considering a beam of wave rays that reflects from a wall. The combination of an incoming and a reflected wave ray yields motions that add up to motions that are not parallel to one of the individual wave rays. Over a period, the projection of the motion can then be an ellipse, with ellipticity and orientation depending on the location in the beam.

Therefore, it seems natural to use ellipse parameters to describe the observed patterns. This is illustrated in figure 3.6(b). The ellipse can be characterized by its main axes U and V, phase φ and orientation ψ. However, when motion is nearly circular, slight perturbations determine the orientation ψ and therefore φ, resulting in incoherent pictures with phase jumps. Also, in our definition ψ varies between 0 and 360 degrees, with the consequence that φ is between 0 and 180 degrees, rather than the other (physically desirable) way round. In order to circumvent this, the ellipse is decomposed into two circles, one traversed clockwise and the other anticlockwise. These two circles are characterized by their radius W_- and W_+ and 'phase' θ_- and θ_+, with $U = W_+ + W_-$, $V = W_+ - W_-$, where V will take negative values for clockwise motion, $\varphi = (\theta_- - \theta_+)/2$ and $\psi = (\theta_+ + \theta_-)/2$. A more detailed description of this decomposition can be found in Maas & van Haren (1987). When interpreting pictures of θ_-, one must keep in mind that the smaller θ_-, the larger the true phase, since θ_- is defined as the anticlockwise angle with the horizontal axis, whereas the circle is traversed in clockwise sense (figure 3.6b). The advantage of this decomposition is that the time series can be summarized in a few pictures, with the restriction that flow other than this ellipsoidal motion with frequency equal to the forcing frequency is filtered out. Nevertheless, since ellipsoidal motion is thought to represent the field we are interested in, and it is clearly the dominant frequency in the spectrum, this approach is justified.

The observations are presented in terms of U, θ_+ and θ_-. Major axis U represents the intensity of motion. The values of the minor axis V indicate deviations from rectilinear motion. They are not shown separately, since they only seem to be significant near the walls, where the waves reflect. The phases θ_+ and θ_- do not represent the physical phase of the wave, since only a projection of the full 3-D motion is considered. Still, these phase parameters indicate the propagation of the waves in the xz-plane.

Pictures of U, θ_+ and θ_- of all different attractors and the standing wave mode are shown in plate I for y=0.24. At this y-coordinate a 2-D description can be justified, since it is not

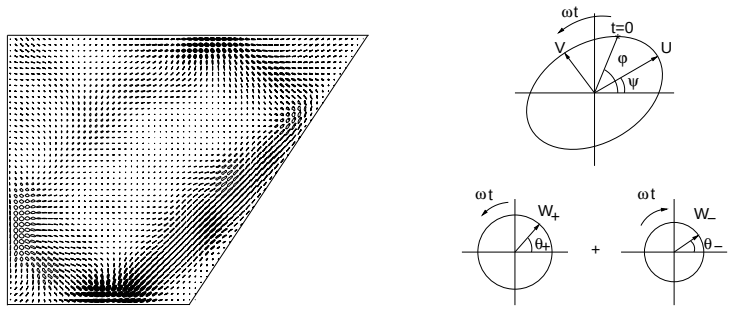

(a) *(b)*

Figure 3.6: *(a)* Hodographs of self-similar attractor (arbitrary scaling), based on asynchronous sampling of 120 measurements and averaging per seven measurements with nearly identical phase. For the solid ellipses motion is clockwise, for the transparent ellipses motion is anticlockwise. *(b)* Decomposition of a current ellipse into two counterrotating circles.

close to a vertical end wall and the vorticity-conserving flow is directed almost purely along the y-axis. It appears that all the predicted structures are visible here. The colour scale is equal for all attractors. The figures are constructed such that they start with the same phase with respect to the sinusoidal forcing ($t = 0$), except for the (1,3)-attractor for which this phase was not determined well. They are again based on asynchronous sampling and averaging over 7 vector fields with nearly the same phase.

In some pictures one can observe a narrow band from the top ($x \approx 1$) to the bottom ($x \approx 0.5$). This is caused by the laser. The laser beam is turned into a laser sheet by a prism to illuminate the fluid. But there is still a trace of the direct ray, which perturbs the measurements. In the data processing, we interpolated to get rid of this perturbation, but it was not always equally successful.

The *critical slope attractor* is not very well visible, only the part near the sloping wall shows intense motion. There is relatively much motion outside the attractor, as compared with the other frequencies. From the pictures of θ_+ and θ_- the V-shape becomes more clear. Lines of equal phase are roughly aligned along the attractor for θ_- near the sloping wall. The other part of the attractor coincides with the rapid phase changes. Outside the attractor, the phases are varying smoothly over the plane and lines of equal phase are not strictly parallel to wave rays.

The *square* and *self-similar attractor* are clearly visible. Motion is most intense near the sloping wall, where the actual focusing takes place. Following the attractor in clockwise sense, the intensity decays. Outside the attractor there is not much motion. Phase lines are parallel to the attractor. The theoretical directions of phase propagation, based on clockwise energy propagation along the attractor, are well reproduced by the observations: phase propagates outwards for characteristics with positive slope and inwards for characteristics with negative slope. In the middle of the cross-section, far away from the attractor, motion is weak. The observed phases cannot be fully trusted then, but structures are spatially coherent which gives the results credit.

Phase lines of θ_+ are circling around the top and bottom reflection points of the attrac-

tor, where the ellipses are completed in a clockwise direction. Phase lines of θ_- are circling around the side wall reflections of the attractor, where the ellipses are completed in anti-clockwise direction. This can be explained by the fact that at the location where all phase lines come together (amphidromic points) this phase is meaningless since the corresponding motion W_+ or W_- vanishes there.

The *degenerate attractor* is rather weak and the line of maximum U is a little bit below the predicted attractor location. There is a sharp phase contrast at the location of the theoretical attractor. This suggests that particle motion at one side of the degenerate attractor is opposite to that at the other side, which gives rise to high shear around it, such that the attractor itself is not visible.

The *(1,2)-mode* looks like a weak attractor at first sight. Motion is concentrated around a particular characteristic. On the line that connects the upper right corners to the lower right corner velocities are (nearly) zero (see figure 3.2e). Motion is clearly less intense than for the square and self-similar attractor. Phase lines are not everywhere parallel to the wave rays. The sharp phase contrast corresponds to the line connecting the upper right corner to the lower right corner of the basin, through the centers of the counterrotating cells. Evidence that this is a standing mode and not an attractor will be given further on.

The *(1,3)-attractor* is relatively weak. For this frequency, focusing is weaker than for the (1,1)-attractor. Also, the attractor length (perimeter) is larger so that viscous losses along the attractor may become more important. In the vertical, the scale of the attractor is smaller than for the square and self-similar attractor. Where two parts of the attractor with opposed particle motion are closely together, they may interact due to viscous effects, also reducing the strength of the motion. The location of high velocities in the measurements appear to agree well with the theoretical location of the attractor. It is difficult to give a clear interpretation of the phase pictures. The phase changes very rapidly across the line connecting the upper right corner to the lower left corner.

Phase propagation

As already mentioned, there is evidence that the (1,2)-mode behaves differently from the attractors. Phase changes take place at the same time over the whole cross-section. This is illustrated in figure 3.7. The parameter $\phi = \arctan(w/u)$ is plotted as function of time on a vertical line. Although this parameter is not equal to the phase, changes of ϕ are an indication of the phase changes. These sections are chosen such that for the square attractor the strongest branch of the attractor is included. The term *branch* refers to a part of the attractor between two boundary reflections. For the (1,2)-mode both cells are included and for the (1,3)-attractor the part where propagation is clearest. Asynchronous sampling was used to get a good time resolution. The pictures confirm that the flow field is nearly purely periodic. The single period is plotted twice to give a better impression of the continuity of phase propagation.

For the *square attractor*, phase shifts downwards with increasing time, implying wave propagation. This is in accordance with energy propagation downwards as expected from the clockwise energy propagation along the attractor. There is a phase shift around $z = 1/2$, related to the transition of one branch of the attractor to another, but this is not visible in the black and white figure.

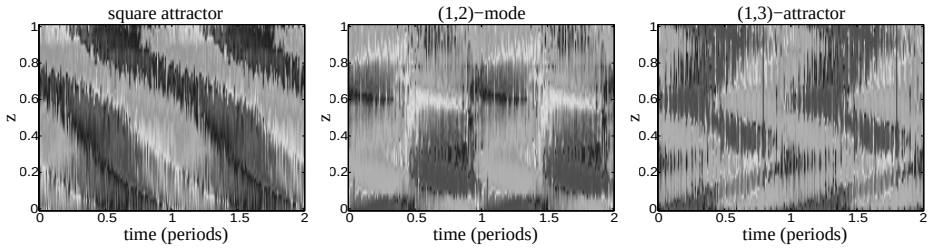

Figure 3.7: Angle $\phi = \arctan(w/u)$ as a function of depth and time on vertical lines for square attractor at $x = 0.99$, (1,2)-mode at $x = 0.84$ and (1,3)-attractor at $x = 0.32$. The pattern is shown twice (two identical periods, asynchronous sampling) to visualize the pattern of phase propagation better.

This is in strong contrast with the *(1,2)-mode*, which can be recognized as a standing wave. Patterns do not alter during half a period, then they change abruptly over the whole cross-section, to remain constant for the next half period. The upper part of the upper cell and the lower part of the lower cell have the same phase, as do the lower part of the upper cell and the upper part of the lower cell. This is consistent with the idea of two counterrotating cells (figure 3.2h).

For the *(1,3)-attractor* there is upward phase propagation in the lower part, downward propagation in the middle part and upward propagation in the upper part. This agrees well with the expected propagation directions and locations where this direction of phase propagation changes. Only in the uppermost part ($z > 0.9$) there is downward propagation again. This is not according to the predicted attractor shape, but can be attributed to a direct wave ray emanating from the upper left corner. Such a wave ray can be seen in the picture of U for this attractor in plate I.

Along-channel changes

Measurements were taken at different y-positions. These can be used to study the structure of the attractor in the y-direction. To get an overall idea of the strength of the motion for different distances to the front wall, an average of the absolute value of the velocity components is computed per cross-section. The quantity $\mathcal{U}$ is defined as

$$\mathcal{U} = \frac{1}{NM} \sum_{n=1}^{N} \sum_{m=1}^{M} |u|_{nm}$$

with M the number of gridpoints and N the number of time steps. $\mathcal{W}$ is similarly computed with w replacing u. This method does not distinguish wave motion from other types of motion, periodic or not. But the results appear to be instructive to compare the y-dependent behaviour at the different frequencies, when interpreted in combination with other observations. The results, a very strong compression of the data of almost all the observed vertical cross-sections, are presented in figure 3.8.

With increasing values of $\tan\theta$ (increasing frequency of the waves), u increases and w decreases. This implies that the difference between $\mathcal{U}$ and $\mathcal{W}$ increases. For a single frequency,

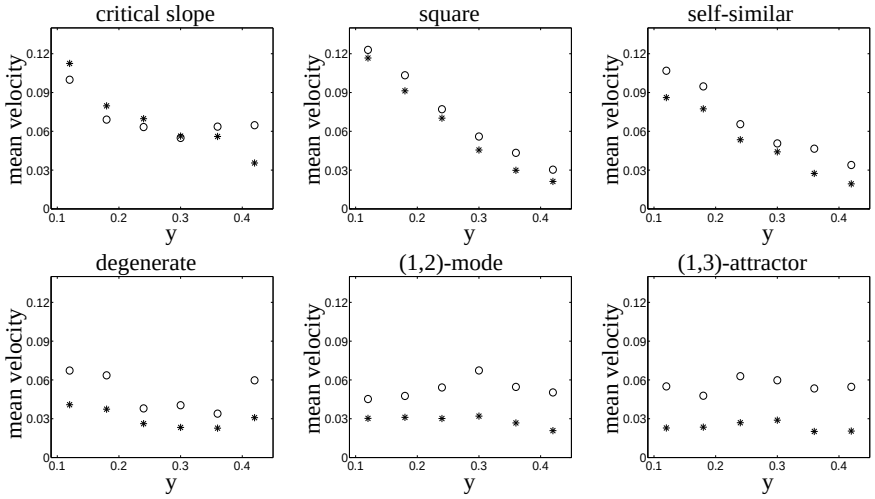

Figure 3.8: Mean speed in x ($\mathcal{U}$, circles) and z-direction ($\mathcal{W}$, stars) over the cross-section as a function of distance to the front wall for the different frequencies (table 3.1).

this difference must be constant if the 2-D approach is valid, as is observed in the figures of the square attractor and the (1,3)-attractor. Where this is not the case, for example for the critical slope attractor, other phenomena must contribute to the velocity field. In general the ratio $\mathcal{U}/\mathcal{W} \approx \tan\theta$ with the tendency to be a little too large; the u-component of the flow is somewhat too strong. For small y-values this might be an effect of the vorticity-conserving flow that is purely horizontal, but since the u-component of the vorticity-conserving flow should decrease rapidly with increasing y the ratio should also decrease, which is not observed. Another explanation is that slowly rotating steady vortices, that were observed over the flat part of the bottom in experiments with dye and that have nearly purely horizontal motion, account for this effect.

The most striking difference between the observations for the different frequencies is that for the critical slope attractor, the square and self-similar attractor there is a clear decay of $\mathcal{U}$ and $\mathcal{W}$ with increasing y where this is not the case for the other frequencies. This cannot be explained by the vorticity-conserving flow that contributes most near the front wall. There is no reason to expect that this contribution varies so strongly with the frequency.

Further and more detailed analysis of the structure of the wave field in the y-direction is obtained by comparing the ellipse parameters in the successive cross-sections. For the critical slope and the self-similar attractor all the vertical cross-sections are presented. For the other frequencies only a description will be given.

The *critical slope attractor* is shown in plate II at all observed y-coordinates since its behaviour changes considerably in the y-direction. For $y > 0.3$ the phase could not be determined by matching with the horizontal cross-sections, since the horizontal cross-sections do not extend further. But it could be determined by regarding the phase of the plane-averaged u-velocity, a method that does not work for the other frequencies but does reproduce the matching results for this specific frequency. The attractor is developed best at $y = 0.12$

where the motion is strongest. In the picture at $y = 0.18$ the left (diagonal) part of the attractor is clear but the part at the sloping wall is not, at $y = 0.24$ it is the other way round. At other locations either the left diagonal part or the part parallel to the sloping wall is well visible, but not in the same cross-section. Overall, the part near the sloping wall is best visible. The general structure of the phase lines is the same over all y-values. The V-shape can be recognized even up to $y = 0.42$. But the absolute values vary considerably between the different sections. It appears that the phase decreases with increasing y-value, implying energy propagation from $y = 0$ towards the centre of the tank. Phase pictures that are about 1/5 of the basin's length (100 cm) apart have almost the same phase, indicating a wavelength of this size in the y-direction.

Instabilities and turbulence in the bottom boundary layer at the slope, as reported by Cacchione & Wunsch (1974) and Ivey & Nokes (1989) for critical internal waves, were not observed. Our observations do not resolve small-scale motion as well as theirs (Schlieren-pictures), but on the scale of our observations the motion along the sloping wall is described reasonably well by the two-dimensional attractor model.

In plate III the ellipse parameters are shown for the cross-sections of the *self-similar attractor*. All pictures have the same phase with respect to the sinusoidal forcing. Only for $y = 0.42$ the phase is uncertain, matching with horizontal cross-sections did not work since the motion is very weak there. The most striking feature of U is the rapid decrease with increasing y, with maximum values near the sloping wall where the waves were focused. This part of the attractor is still faintly visible at $y = 0.36$. Also, at $y = 0.12$ the shape of the attractor is slightly different, it is more narrow, the reflection at the sloping wall occurs somewhat higher, the reflection point at the bottom is shifted a little to the left and the reflection at the straight wall is at a lower position. There is strong horizontal motion near the top of the tank, which is also observed in Maas (2001). At $y = 0.18$ the attractor is best visible. For $y > 0.3$, the motion for $x < 0.3$ is horizontal. The phase lines are well aligned along the attractor. Outside the attractor, where the motion is weak, the phases are still rather coherent. Only for large y, where the attractor is hardly visible, the structures become incoherent. The phases are more or less the same at the different y-positions; within the accuracy of the phase determination, no phase propagation can be observed. For the *square attractor* (not shown) the behaviour is similar, even the phases are the same as for the self-similar attractor, in the equivalent part of the attractor at the same y-position.

We will briefly discuss the results for the other frequencies, they are not shown. The *degenerate attractor* is badly developed at $y = 0.12$ where a lot of horizontal motion is present in the upper half of the cross-section. However, from the θ_--picture the line from the upper right to the lower left corner is clearly recognizable. The attractor is still visible at $y = 0.42$. U is somewhat larger at $y = 0.18$ and $y = 0.24$, but does not decay further with increasing y. There is no evidence for phase propagation in the y-direction, as far as could be observed.

The *(1,2)-mode* behaves a bit similar to the degenerate attractor. At $y = 0.12$ the cellular pattern is not visible from U although the θ_--pattern hints at a structure connecting the upper right to the lower right corner. The motion is again dominated by horizontal motion in the upper half. At $y = 0.24$ and $y = 0.3$ the cellular structure is most clear, but at $y = 0.36$ and $y = 0.42$ large parts can still be recognized from U. From the phase lines the structure is even clearer, especially the large upper cell with a sharp phase contrast diagonally through

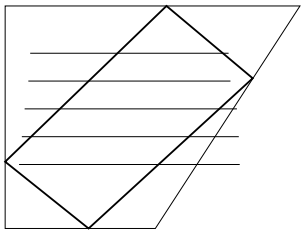

Figure 3.9: Location of horizontal cross sections at z =0.29, 0.41, 0.54, 0.66 and 0.79 with respect to a vertical cross section.

the cell. At $y = 0.12$ the phase with respect to the forcing could not be determined well, from the other cross-sections no significant phase propagation in the y-direction was observed.

The *(1,3)-attractor* is also not visible at $y = 0.12$, only in the middle of the cross-section some areas of higher U are visible. The phase structure has two more or less equal cells, one in the upper and one in the lower half of the section. At $y = 0.18$ parts of the attractor become visible, and at $y = 0.24$ the attractor is best visible. At larger y-coordinates the structure is not as clear anymore but large parts of the attractor are visible, U hardly decreases. There were serious problems in matching with the horizontal cross-sections, so no conclusions can be drawn regarding the phase propagation in the y-direction.

3.4.2 Horizontal cross sections

Measurements in horizontal cross sections at different z-level were taken for all frequencies. Unfortunately, only a small part of the tank could be observed for a single camera position, roughly from $x = 0.1$ to $x = 1.6$ and from $y = 0.1$ to $y = 0.3$. In figure 3.9 the positions of the horizontal cross sections with respect to the self-similar attractor are illustrated. For the self-similar and square attractor, also measurements were taken that extend from $y = 0.3$ to $y = 0.5$, but they are of poor quality. There were more problems in obtaining satisfactory results. The metal frames around the glass plates inhibited the detection of particle motion at the borders of the glass plates. By interpolation this was compensated more or less. At some locations the measurements were bad due to the absence of tracer particles, which settled to the bottom very slowly during the experiment, or due to stains on the glass plates. In the horizontal, the vorticity-conserving flow dominates the fluid motion. To investigate the structure of the inertial wave field, this flow must be subtracted from the observed fields. Subtraction of the theoretically predicted field, while not exact, is also a source of errors. But it does eliminate the most obvious vorticity-conserving flow features.

As can be concluded from the previous paragraph, except for the critical slope attractor, the wave field does not change significantly in the y-direction, apart from intensity changes. The behaviour of each attractor is illustrated with results from a single (most illustrative) cross section. The results are shown in plate IV in terms of the ellipse parameters U and θ_-. Motion was dominantly clockwise, only where the intensity was very low the motion was anticlockwise, therefore θ_+ is not shown. The black lines indicate the intersections with the theoretical attractor.

The cross section of the *critical slope attractor* at $z = 0.29$ has most intense (although weak compared to the intensities observed in the vertical cross sections) motion near the slope and around the theoretical line, but also closer to the straight wall. The change of intensity of the parts of the attractor that has been observed in the vertical cross sections is not observed clearly in the horizontal cross sections. In this area above the flat bottom some steady vortex activity was observed from dye experiments, but it is assumed to be filtered out by using the ellipse parameters. In the picture of θ_- one immediately sees the phase change in the y-direction, suggesting wave propagation in negative y-direction, implying energy propagation from the front wall ($y = 0$) into the interior, with a wavelength that is a little larger than the cross section, about $1/4$. In the other horizontal cross sections of this attractor there is no clear intense motion at the theoretically predicted locations. But again the phase propagation towards the front wall can be observed with a wavelength of about $1/4$. This is consistent with the observations in the vertical cross sections. Also a phase change across the attractor in the x-direction is reproduced.

Also for the *square attractor* the cross section at $z = 0.29$ is shown. At this level the intersections with the strongest parts of the attractor are clearly visible from the high values of U. It is remarkable that these values do not persist over the length of the cross section, especially the change around $x = 0.3$ for $y < 0.15$ is remarkable. The phase lines in this cross section are not fully parallel to the y-axis but there is no clear phase propagation in this direction. Near $x = 0.2$ there is phase propagation in the positive $x-$direction (energy propagation towards $x = 0$), as already observed in the vertical cross sections. From the other cross sections we cannot observe consistent phase propagation directions in the y-direction either. Locations of intense motion cannot always be attributed to the attractor and are not continuous in the y-direction, although this was suggested by the results in the vertical cross sections.

For the *self-similar attractor* the behaviour at $z = 0.54$ is illustrated. There is strong motion near the sloping wall, where the observations are slightly below the reflection point. The weak part of the attractor is not or hardly visible. Phase lines are almost uniform in the y-direction. Near the branches of the attractor the directions of phase propagation are consistent with the observations in the vertical cross sections: phase propagation towards the sloping wall near the sloping wall and towards the straight wall for the other branch. In the other cross sections the energy is concentrated near the sloping wall and sometimes also around the other (in practice weak) branch of the attractor. Phase lines are dominantly uniform in the y-direction.

The *degenerate attractor* has a remarkable line of weak motion around the theoretically predicted attractor, as already observed in the vertical cross sections. There is strong motion near the straight wall. At other levels of observation there is also stronger motion at the sloping wall side of the attractor. Structures do not extend over the full y-range of the cross sections. The attractor is visible by means of the phase jump. Phase lines are roughly uniform in the y-direction. This behaviour is observed at all levels of observation.

The cross section at $z = 0.66$ for the *(1,2)-mode* is through the centre of the upper cell ($x = 1$). In this centre there is no motion, which is confirmed by the observation. At both sides of this line of no motion there is rather strong motion. There is a phase jump over this line. The phase is clearly uniform in the y-direction. In all horizontal cross sections the phase is dominantly uniform in the y-direction. In the x-direction there is a rapid phase change

at the locations corresponding with the characteristic connecting the right upper corner to the right lower corner. The locations of intense motion are consistent with the vertical cross sections, but again not continuous in the y-direction.

For the *(1,3)-attractor*, the cross section at which most intense motion can be expected is the one at $z = 0.66$. Here the attractor is intersected close to the uppermost reflection at the sloping wall (focusing). For $y > 0.2$ there is indeed stronger motion. However, this motion is weaker than for the other attractors. At the other horizontal cross sections there is nowhere really intense motion that can be related directly to the theoretically predicted attractor. Motion is everywhere less intense than for the other forcing frequencies. The phase patterns at different z-levels vary both in x- and in y-direction when comparing them. The main phase changes for the different cross sections seem to be related to the characteristic connecting the upper right corner to the lower left corner of the tank. It is not possible to draw firm conclusions about propagation in the y-direction.

3.5 Discussion

The square attractor was already observed in experiments by Maas (2001), in a smaller tank of similar shape. His result is reproduced and extended with observations of other attractor shapes and a standing wave, which are predicted for different frequencies. This shows that also in three dimensions waves can be focused towards an attractor. The two-dimensional theory correctly predicts the frequency interval over which a certain attractor exists and the shape of the attractor. Although viscosity will prevent the existence of a true line attractor, as a first order description this theory is valuable.

A further aim was to study the three-dimensional behaviour of the waves. Separation of variables is not possible for the basin with a sloping boundary, and no alternative to find solutions is known to us. Therefore we have to rely fully on the observations.

The critical slope attractor is the only wave pattern with distinct three-dimensional behaviour on the scale of the observations. Its intensity decreases with increasing y and the location of the strongest motion on the attractor changes with y. There is clear phase propagation towards the front wall ($y = 0$) and energy propagation into the interior, with a wavelength in the y-direction between 1/5 and 1/4, as follows from the observations in the vertical and horizontal cross sections.

The other attractors do not exhibit clear phase propagation in the y-direction, only intensity changes are detected. The square and self-similar attractor are strong near $y = 0.12$ but their intensity decreases rapidly with increasing y. The degenerate and (1,3)-attractor and the standing mode are not as strong, but their strength is more or less constant for increasing y.

At least part of the variation of the strength of the motion with the y-position must be attributed to the forcing mechanism; in the present experiment weak modulation of the rotation rate. Another experiment was done in which waves were excited by a paddle in the corner of the tank (near $x = 0$, $z = 1$), extending over the full length of the tank. No modulation of the rotation was applied. This set-up had the disadvantage that a direct ray is visible, that is stronger than the wave attractor. It was difficult to provide enough energy to the fluid to generate an attractor without introducing nonlinear effects. The few measurements for this set-up, for an attractor in the (1,1)-domain, showed more intense motion towards the centre

of the tank ($y = 0.3$) than near the front wall ($y = 0.12$). So the distribution of energy in the y-direction seems not an intrinsic property of the wave field.

It is likely that when waves are generated by modulation, direct forcing near the end walls, where the vorticity-conserving flow has a cross-slope component, dominates the indirect generation (Ekman pumping). It remains puzzling why for the weaker attractors this decrease with increasing distance to the end walls is not observed.

The (1,2)-mode looks like an attractor in vertical cross sections, since the most intense motion is confined to narrow bands. However, in time the velocity-changes occur almost uniformly over the vertical cross section, the waves are not travelling waves. Contrary to the common idea that the standing modes are the strongest motions, the motion is weak, compared to the square and self-similar attractor. Therefore, and for the following reason, the term 'resonant mode' is not appropriate in this case. The standing wave does not suffer from nonlinear breakdown phenomena as studied by McEwan (1970) and Manasseh (1992) for resonant modes in a cylinder. Asynchronous sampling could be applied without any difficulty. This indicates a steady pattern for the full period of observation, which is more than half an hour and spans more than 70 rotation periods and several planes of observation. Apparently the rotation rate and excitation strength, which play an important role in the growth of the instabilities according to McEwan (1970), are low enough. We speculate that focusing of the waves during part of the oscillation period prevents instabilities from growing, since it forces unstructured motion back to structured motion, a process that will not take place in a rotating cylinder. Also, the damping rate may be increased due to the smaller scales imposed by wave focusing.

The wave rays connecting the corners of the tank for the (1,2)-mode are clearly visible as lines of low motion and sharp phase contrast. This is probably a result of the forcing function. Wood (1965) calculated the nature of such lines of discontinuity for a rotating and precessing cylinder. Their exact properties (discontinuity in velocity or velocity gradient) depend on the number of reflections it takes before the lines are reflected back onto themselves. Baines (1967) also made calculations regarding these lines, for a rotating cylinder (radius a) in which inertial waves were forced by oscillation of the end caps. At these end caps the vertical velocity is essentially prescribed as $f(r)\cos\omega t$ with r the radial coordinate. Lines of discontinuity of the velocity occur if $f'(r)$ has discontinuities and if $f'(a) \neq 0$ and in some cases if $f''(a) \neq 0$. Maas & Lam (1995) illustrate, for the bucket (two sloping walls), that the shape of the resonant mode is strongly dependent on the exact properties of a function on the boundary. This function prescribes the information carried by the characteristics (partial pressure) and replaces the prescription of the forcing mechanism. Only if this function has a derivative equal to 0 at the boundaries of the region for which it can be prescribed, the cells are smooth and there are no lines of discontinuity. In an experiment, one cannot prescribe this function at will. It is determined by the chosen setting and in general the condition of zero derivative will not hold. For example McEwan (1970) reports lines of strong shear emanating from the corners of the rotating cylinder. Also Greenspan (1968*a*) and Beardsley (1970) report wave rays stemming from the upper corners of rotating cones, that are seen to reflect a few times at the boundaries. They applied modulation of the rotation frequency to generate waves via Ekman pumping like we did. However, in the rotating cones the vorticity-conserving flow will not have a cross-slope component, which is the primary forcing in our case. We also sometimes observed a wave ray emanating from the corner at $x = 0$, $z = 1$ for

the square and self-similar attractor.

Not many experiments are known from literature in which focusing of inertial waves is studied experimentally. The emphasis has been on resonant modes and their interaction and the interaction with the background flow. At first sight, the article by Beardsley (1970) is not an exception, but his results for the truncated cone (frustum) can be interpreted in terms of wave attractors. Plotting the Lyapunov exponent for his configuration yields a structure similar to that of figure 3.1b, with windows of attractors and isolated frequencies for which resonances occur. The amplitude maxima in the pressure sensors that he used do not occur for the simplest resonant modes, but for frequencies close to the strongest windows of attraction. Henderson & Aldridge (1992) solve the equations for the frustum numerically and interpret the results in terms of eigenmodes. However, their numerical grid is not fine enough to resolve a wave attractor. They also analytically compute two special ray paths, connecting the upper and the lower corners respectively, and compare the corresponding propagation angle (frequency) with the numerically determined eigenfrequency (their figure 4). The two paths yield two slightly different values for the propagation angle. For an eigenmode, this angle should be unique. These special ray paths can be identified with the upper and lower boundary of the window of an attractor, thus explaining the appearance of the two different values.

To conclude: the two-dimensional theory correctly predicts the frequencies and basic shapes of the attractors and the standing mode, but the three-dimensional structure has not been resolved satisfactorily. It would be interesting to have observations near $y = 0$ and for the other half of the tank to see if the behaviour is more or less symmetric or antisymmetric with respect to $y = 1/2$ or if there is a preferential direction. Possibly, rapid changes near the walls, as predicted for inertial waves in a rectangular box (Maas, 2003) could not be resolved well in our experiments. Similar experiments have been carried out in a smaller tank. They can shed more light on the three-dimensional behaviour of the waves and hope report on them in chapter 4. Also numerical simulations would be instructive.

This chapter is accepted for publication in *Journal of Fluid Mechanics*, under the title "Observations of inertial waves in a rectangular basin with one sloping boundary", by A.M.M. Manders and L.R.M. Maas.

We gratefully acknowledge the help during the experiments from the team of the Coriolis Laboratory (Grenoble) and Frans Eijgenraam, Ronald de Leeuw and Theo Gerkema (NIOZ). We would also like to thank Maartje Rienstra for her contribution to the experiments, data processing and discussion. We thank M. Rieutord, J. Sommeria and an anonymous referee for constructive remarks. This project was financially supported by the European Community (program 'Access to major research infrastructures').

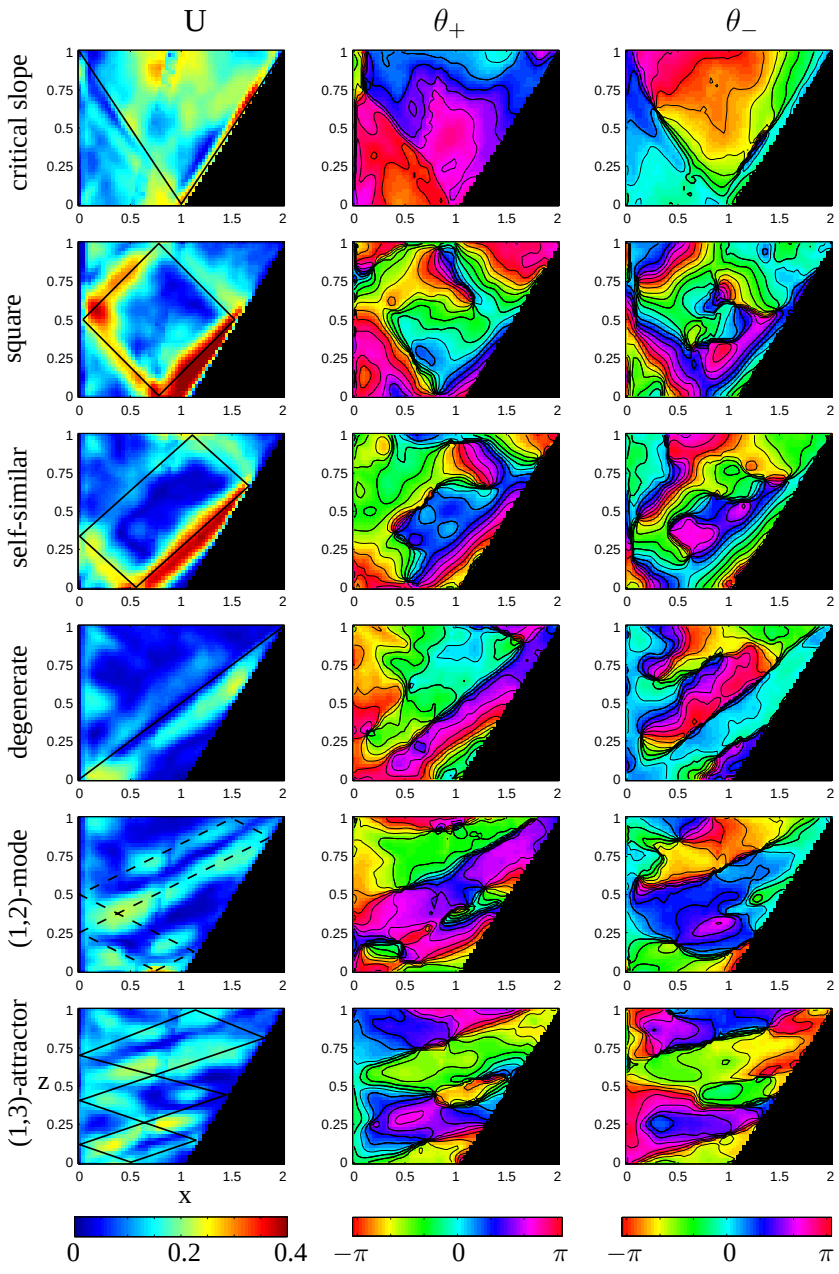

Plate I: Decomposition of hodographs (figure 3.6) for (1,1)-attractors (critical slope, square, self-similar and degenerate attractor), standing (1,2)-mode and (1,3)-attractor at $y = 0.24$. The scale for U ranges from 0 (dark blue) to 0.4 cm/s (dark red). The colour scale for $\theta_{+,-}$ is periodic. The black lines indicate the theoretically predicted attractor. In case of the (1,2)-mode a single, somewhat arbitrary periodic characteristic that matches the pattern is plotted (dashed).

Appendix: Vorticity-conserving flow

Here the structure of the vorticity-conserving flow is derived for a tank with a sloping wall. This tank has length L and height H_0 over the flat bottom, the water depth $H(x)$ itself is function of x only. The top of the basin has width $2B$ and the bottom has width B. The angular frequency $\Omega(t)$ consists of a weak modulation $\epsilon\Omega_1(t)$, $\epsilon \ll 1$, around the steady state value Ω_0.

When studying spin-up problems in tanks with a sloping bottom, van Heijst *et al.* (1994) found that the exact solution for a wedge-shaped tank ($2B = H_0, L \gg H_0$) showed almost no variation in the vertical direction. This justified the shallow-water approximation for a tank with sloping bottom, that is long in the along-slope direction ($L \gg H_0$). Since our tank has a closely related geometry, we follow their approach and also make this approximation. This enables the calculation of an exact solution for the approximated problem.

The first step is to compute the vorticity $\nabla \times \partial\mathbf{u}/\partial t$ for the linearised momentum equations (1). Because of the shallow-water conditions, variations of u and v with z are neglected. The vertical vorticity equation reads

$$\frac{\partial}{\partial t}\left(\frac{\partial v}{\partial x} - \frac{\partial u}{\partial y}\right) = -2\Omega_0\left(\frac{\partial u}{\partial x} + \frac{\partial v}{\partial y}\right) - 2\frac{\partial \Omega_1}{\partial t}. \tag{A-1}$$

Integrating the continuity equation (2) over the vertical, with boundary conditions of no flow through the bottom and the top, results in the equation for the conservation of mass:

$$\frac{\partial}{\partial x}(uH) + \frac{\partial}{\partial y}(vH) = 0. \tag{A-2}$$

Substitution in the vertical vorticity equation (A-1), division by H and introduction of ζ for the vertical vorticity, $\zeta = \partial v/\partial x - \partial u/\partial y$, gives

$$\frac{1}{H}\frac{\partial \zeta}{\partial t} = \frac{2\Omega_0}{H^2}\left(u\frac{\partial H}{\partial x} + v\frac{\partial H}{\partial y}\right) - \frac{2}{H}\frac{\partial \Omega_1}{\partial t} \tag{A-3}$$

Rearranging terms shows that the equation (A-3) is the lowest order of the total time derivative (material derivative)

$$\frac{D}{Dt}\left(\frac{\zeta + 2\Omega}{H}\right) = 0 \tag{A-4}$$

which means that individual particles conserve potential vorticity:

$$\frac{\zeta + 2\Omega}{H} = C.$$

Before the modulation starts, the fluid is in solid body rotation with angular frequency Ω_0. This gives the constant C the value $2\Omega_0/H$. Take the modulation of the form

$$\Omega = \Omega_0(1 + \epsilon \sin \omega t)$$

so that the perturbation vertical vorticity equals

$$\zeta = \frac{\partial v}{\partial x} - \frac{\partial u}{\partial y} = -2\Omega_0 \sin \omega t. \tag{A-5}$$

Introduce the mass transport stream function

$$\Xi(x, y, t) = \Psi(x, y) \sin \omega t \tag{A-6}$$

with the spatial part defined as

$$Hu = -\frac{\partial \Psi}{\partial y}, \qquad Hv = \frac{\partial \Psi}{\partial x}. \tag{A-7}$$

Substitution of these expressions into equation (A-5) leads to

$$\nabla^2 \Psi - \frac{1}{H}(\nabla H \cdot \nabla \Psi) = -2\Omega_0 H. \tag{A-8}$$

The boundary conditions are

$$\Psi = 0 \text{ at } x = 0,\ x = 2B \text{ and at } y = 0,\ y = L. \tag{A-9}$$

The bottom profile H of our tank is given by

$$H(x) = \begin{cases} H_0 & 0 \le x < B \\ H_0(1 - \frac{x-B}{B}) & B \le x \le 2B \end{cases} \tag{A-10}$$

Substitution of this bottom profile naturally splits the equation for the stream function in two parts: one for the flat bottom and one for the sloping bottom, denoted by Ψ_1 and Ψ_2 respectively

$$0 \le x < B \qquad \nabla^2 \Psi_1 = -2\Omega_0 H_0 \tag{A-11}$$

$$B \le x \le 2B \quad \nabla^2 \Psi_2 + \frac{1}{H_0(2 - x/B)} \frac{H_0}{B} \frac{\partial \Psi_2}{\partial x} = -2\Omega_0 H_0 (1 - \frac{x - B}{B}) \tag{A-12}$$

These equations can be solved separately but the solutions are subject to matching conditions at $x = B$, requiring continuity and smoothness.

For convenience the equations will be scaled.

$$\begin{aligned} y &= L(y' + 1/2) \\ x &= B(x' + 1) \\ \Psi &= -2B^2 H_0 \Omega_0 \Psi'. \end{aligned} \tag{A-13}$$

The dimensionless equations (primes dropped from now on) are

$$\Psi_{1xx} + \mu^2 \Psi_{1yy} = 1 \tag{A-14}$$

$$\Psi_{2xx} + \frac{1}{1 - x} \Psi_{2x} + \mu^2 \Psi_{2yy} = 1 - x \tag{A-15}$$

where $\mu = B/L$, with boundary conditions

$$\begin{array}{lllll} \Psi_1 = 0 & \text{at} & x = -1 & \text{and at} & y = \pm 1/2 \\ \Psi_2 = 0 & \text{at} & x = 1 & \text{and at} & y = \pm 1/2 \\ \Psi_1 = \Psi_2 & \text{at} & x = 0 & & \\ \frac{\partial \Psi_1}{\partial x} = \frac{\partial \Psi_2}{\partial x} & \text{at} & x = 0 & & \end{array} \tag{A-16}$$

A solution of the homogeneous equation for equation (A-14) is obtained by separation of variables, leading to

$$\Psi_{1h} = P \cosh(\frac{\lambda}{\mu} y) \sin(\lambda(1+x)) \tag{A-17}$$

A particular solution to the inhomogeneous equation is $\Psi_{1p} = \frac{1}{2}(x+1)^2 + c_1(x+1)$. The complete solution satisfies the boundary condition at $x = -1$. The constants P and c_1, and the eigenvalue λ are to be determined from matching of the solutions at $x = 0$ and the boundary conditions at $y = \pm 1/2$.

Separation of variables for the homogeneous part of equation (A-15) leads to a solution in terms of the first order Bessel function J_1

$$\Psi_{2h} = R \cosh(\frac{\lambda}{\mu} y)(1-x) J_1(\lambda(1-x)) \tag{A-18}$$

A particular solution to the inhomogeneous equation (A-15) is $\Psi_{2p} = \frac{1}{3}(1-x)^3 + c_2(1-x)^2$. The complete solution satisfies the boundary condition at $x = 1$, the constants R, c_2 and the eigenvalue λ are to be determined from matching at $x = 0$ and the boundary conditions at $y = \pm 1/2$.

Matching at $x = 0$ gives the values $c_1 = -7/9$ and $c_2 = -11/18$ and leads to the eigenvalue equation

$$J_0(\lambda) \sin\lambda + J_1(\lambda) \cos\lambda = 0 \tag{A-19}$$

which results in a discrete spectum of eigenvalues λ_n that can be approximated numerically and a series of P_n and R_n.

Now that the general structure of the solution is complete, the constants P_n and R_n can be computed from the condition $\Psi_h + \Psi_p = 0$ at $y = \pm\frac{1}{2}$ for both domains, using an orthogonal set of eigenfunctions. The eigenfunctions are:

$$e_m = \begin{cases} \frac{\sin\lambda_m(1+x)}{\sin\lambda_m} & -1 \le x < 0 \\ \frac{J_1(\lambda_m(1-x))}{J_1(\lambda_m)} & 0 \le x \le 1 \end{cases} \tag{A-20}$$

They are orthogonal with respect to the weight function w,

$$w = \begin{cases} 1 & -1 \le x < 0 \\ 1-x & 0 \le x \le 1 \end{cases}$$

and the orthogonality relation reads

$$\int_{-1}^{0} \frac{\sin(\lambda_m(1+x))\sin(\lambda_n(1+x))}{\sin\lambda_m \sin\lambda_n}dx + \int_0^1 (1-x)\frac{J_1(\lambda_m(1-x))J_1(\lambda_n(1-x))}{J_1(\lambda_m)J_1(\lambda_n)}dx$$
$$= \delta_{nm}\frac{1}{2}\left(\frac{1}{\lambda_n}\frac{\cos\lambda_n}{\sin\lambda_n} + \frac{2}{\sin^2\lambda_n}\right) \tag{A-21}$$

The matching condition at $x = 0$ relates the constants P and R as $P_n \sin(\lambda_n) = R_n J_1(\lambda_n) = Q_n$ where Q_n is introduced for convenience. Q_n is determined by the boundary condition at $y = \pm 1/2$. It is computed by inserting $y = 1/2$ in the full solution, multiplying by the eigenfunctions and integration over the domain

$$\int_{-1}^{0} \Psi_{1h}(x,\frac{1}{2})e_m dx + \int_0^1 \Psi_{2h}(x,\frac{1}{2})e_m dx$$
$$+ \int_{-1}^{0} \Psi_{1p}(x)e_m dx + \int_0^1 \Psi_{2p}(x)e_m dx = 0, \tag{A-22}$$

leading to

$$Q_n = \frac{2}{\cosh\frac{\lambda_n}{2\mu}\left(\frac{1}{\lambda_n}\frac{\cos\lambda_n}{\sin\lambda_n} + \frac{2}{\sin^2\lambda_n}\right)}$$
$$\times \left\{\frac{1}{J_1(\lambda_n)}\left(-\frac{1}{\lambda_n^3}J_1(\lambda_n)\ S_{2,0}(\lambda_n) - \frac{1}{2\lambda_n^2}J_0(\lambda_n)S_{3,1}(\lambda_n)\right.\right. \tag{A-23}$$
$$\left.\left. + \frac{11}{18}\frac{1}{\lambda_n}J_2(\lambda_n)\right) - \left(\frac{5}{18\lambda_n} + \frac{1}{\lambda_n^3}\right)\frac{\cos\lambda_n}{\sin\lambda_n} - \frac{2}{9\lambda_n^2} + \frac{1}{\lambda_n^3\sin\lambda_n}\right\}.$$

The functions $S_{2,0}$ and $S_{3,1}$ are Lommel's functions (Magnus *et al.*, 1966).

The complete solution in the original coordinates is given by

$$\Psi = -2B^2 H_0 \Omega_0 \tag{A-24}$$
$$\times \begin{cases} \displaystyle\sum_{n=1}^{\infty} \frac{Q_n}{\sin\lambda_n}\cosh\left(\frac{\lambda_n L}{B}\left(\frac{y}{L}-\frac{1}{2}\right)\right)\sin\left(\lambda_n\frac{x}{B}\right) + \frac{1}{2}\left(\frac{x}{B}\right)^2 - \frac{7}{9}\left(\frac{x}{B}\right) \\ \qquad 0 \le x < B \\ \displaystyle\sum_{n=1}^{\infty} \frac{Q_n}{J_1(\lambda_n)}\cosh\left(\frac{\lambda_n L}{B}\left(\frac{y}{L}-\frac{1}{2}\right)\right)\left(1-\frac{x-B}{B}\right)J_1\left(\lambda_n\left(1-\frac{x-B}{B}\right)\right) \\ \qquad + \frac{1}{3}\left(1-\frac{x-B}{B}\right)^3 - \frac{11}{18}\left(1-\frac{x-B}{B}\right)^2 \\ \qquad B \le x \le 2B \end{cases}$$

The velocities can be derived via

$$u = -\frac{1}{H(x)}\frac{\partial\Psi}{\partial y} \tag{A-25}$$

$$v = \frac{1}{H(x)}\frac{\partial\Psi}{\partial x}. \tag{A-26}$$

This results in an ‘ellipsoidal’ flow, with maximum velocities at the middle of the boundaries and with zero velocity above the flat part, at $x \approx 0.39 \times 2B$.

Chapter 4

On the three-dimensional structure of the inertial wave field in a rectangular basin with one sloping boundary

4.1 Introduction

Homogeneous fluids in solid-body rotation are stably stratified in angular momentum. They can carry waves for which motion is purely in the interior of the fluid. These *inertial* or *gyroscopic* waves have a frequency smaller than twice the rotation frequency (Greenspan, 1968*a*). They are potentially relevant for the liquid outer core of the earth (Malkus, 1968; Aldridge & Lumb, 1987; Aldridge *et al.*, 1989; Rieutord, 1995), spinning spacecraft that contain tanks filled with fluid (Aldridge *et al.*, 1989; Manasseh, 1993), and were found in homogeneous layers in the Mediterranean Sea (van Haren & Millot, 2003). In oceans (Maas, 2001) and lakes (Fricker & Nepf, 2000) they may also be modified by a stable density stratification and then occur as inertio-gravity waves. Inertial waves can redistribute energy via reflections in enclosed geometries. This may lead to regions of high energy concentration, which in turn can act as mixing areas.

An important property of these waves is that their direction of propagation is constrained to a double cone with its center line parallel to the rotation axis. This direction is purely determined by the ratio of wave frequency and rotation frequency and cannot be altered upon reflection. When inertial waves reflect at a sloping boundary, they may become focused or defocused, depending on the slope of the boundary and the angle of propagation, as the cone has no symmetry with respect to this slope. This has important consequences for wave propagation in enclosed fluids. For a quasi-two-dimensional setting (cross-section of an infinitely long channel), repeated reflection with focusing may lead to the appearance of wave attractors: limit cycles on which all wave energy converges (Stewartson, 1971; Maas & Lam,

1995). Such attractors were theoretically predicted for cross-sections of a spherical shell (Stewartson, 1971, 1972; Rieutord & Valdettaro, 1997) and were predicted and experimentally observed for a rectangular tank with one sloping side wall (Maas (2001) and chapter 3 of this thesis). These attractors behave differently from the standing waves for which focusing does not occur (horizontally positioned rectangular tanks or cylinders rotating around their axis) or for which focusing is exactly compensated by defocusing at a subsequent reflection, with the consequence that every individual wave ray returns onto itself (Maas & Lam, 1995) in a two-dimensional setting. Further, the attractors exist over parameter intervals (Israeli, 1972) bounded by parameter values for which the attractor degenerates into a line or two co-existing attractors merge, whereas the standing waves exist for isolated parameter values.

However, when the channel is not infinitely long, a two-dimensional approach is not justified. The angle of propagation in the vertical is conserved upon reflection, but in the horizontal direction waves are refracted when reflecting at a sloping boundary (Phillips, 1963). We were not able to mathematically describe the three-dimensional structure of the wave field in an enclosed basin with sloping wall. But three-dimensional ray-tracing will be used to reveal some properties of the wave field, like the possibility of focusing and the effect of refraction at the sloping wall. In Maas (2001) and chapter 3, mainly vertical cross-sections of different wave attractors were studied in the laboratory. The present study aims at clarifying the along-channel structure. A smaller tank was used, enabling observations of the full horizontal cross-section, with the additional advantage that the time needed to evolve to the desired stationary state is reduced considerably.

4.2 Theory

In this section, the equations of motion are given, from which the Poincaré equation, governing inertial waves, is derived. Then plane wave solutions are introduced. First, quasi-two-dimensional solutions are discussed briefly. Then reflection of these waves at a (sloping) wall is described explicitly, including refraction upon oblique incidence. Finally, wave rays in an enclosed tank are traced numerically.

The basic equations governing a rotating, inviscid, homogeneous fluid are the momentum equations and the continuity equation. In this paper we will consider waves in a frame of reference that is nearly in solid body rotation. The angular velocity of the frame will be $\Omega = \Omega_0 + \epsilon\Omega_1(t)$, where Ω_0 is the background rotation rate while $\Omega_1(t) = \Omega_0 \sin(\omega t)$ is its time periodic modulation. The strength of the periodic modulation ϵ determines the scale of the perturbations. For $\epsilon \ll 1$, the momentum equations can be linearized and the equations for the perturbation velocities and perturbation pressure then read

$$\begin{aligned} \frac{\partial u}{\partial t} &= 2\Omega_0 v + y\frac{\partial \Omega_1}{\partial t} - \frac{\partial p}{\partial x}, \\ \frac{\partial v}{\partial t} &= -2\Omega_0 u - x\frac{\partial \Omega_1}{\partial t} - \frac{\partial p}{\partial y}, \\ \frac{\partial w}{\partial t} &= -\frac{\partial p}{\partial z}, \end{aligned} \tag{1}$$

with u, v, w the perturbation velocity components in the x, y and z-direction with z parallel

to the rotation axis. The gradient of the pressure P and gravitational and centrifugal forces form a dynamic equilibrium at zeroth order. In the linear equation, they are combined in the perturbation pressure term $p = P - (x^2 + y^2)\Omega^2/2 + \rho g z$, where ρ denotes the uniform density and g gravity. The remaining right hand side terms due to rotation and modulation of the frame are the restoring Coriolis force and the Euler body force respectively (Tolstoy, 1973). The continuity equation reads

$$\nabla \cdot \mathbf{u} = 0. \tag{2}$$

At solid boundaries, with inward normal $\mathbf{n}$, the normal velocity of the fluid must vanish, leading to the boundary condition

$$\mathbf{u} \cdot \mathbf{n} = 0. \tag{3}$$

The flow field will be split into two parts, a particular solution of the forced equations and a solution for the homogeneous part. The vertically uniform Euler force induces an alternating horizontal, vorticity-conserving flow. For a theoretical description of the horizontal structure of the vorticity-conserving flow, based on the shallow-water approximation, the reader is referred to the appendix of chapter 3. This flow has an alternating cross-slope component at the sloping wall near the end walls of the tank, which needs to be compensated by inertial waves of frequency ω. Wherever the vorticity-conserving flow is parallel to the walls, inertial waves are also forced through Ekman pumping and suction via the viscous boundary layers (Greenspan, 1968*a*; Aldridge & Toomre, 1969). The inviscid mechanism is thought to be more important here, whereas it does not exist in rotationally symmetric containers. A plot of the theoretical flow field and details about the practical implications for the observations are presented in section 4.4.

Inertial waves, the subject of this study, are described by the homogeneous equations. The way in which the forcing drives these waves is not further resolved, as the equilibrium wave field is expected to be mainly determined by the basin shape and frequency, and in a lesser extent by their generation mechanism.

4.2.1 Derivation of Poincaré equation

To study inertial waves, we consider the case that the fluid is rotating uniformly with constant angular velocity Ω_0. Assuming all variables to be proportional to $\exp(-i\omega t)$ the system of equations (1) can be reduced to a single equation for the pressure:

$$p_{xx} + p_{yy} - \lambda^2 p_{zz} = 0 \tag{4}$$

with

$$\lambda^2 = \frac{4\Omega_0^2 - \omega^2}{\omega^2}. \tag{5}$$

For positive values of λ^2 ($\omega < 2\Omega_0$), this equation is called the Poincaré equation, in honour of H. Poincaré (Cartan, 1922). Separation of variables is no longer possible for a basin with sloping walls, which highly complicates the construction of solutions.

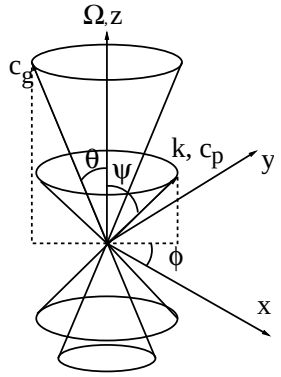

Figure 4.1: Directions of wave vector, phase velocity vector and group velocity vector.

4.2.2 Plane wave solutions

We consider plane waves $p(x, y, z) \propto \exp(i\mathbf{k} \cdot \mathbf{x})$ of arbitrary amplitude, with wave vector $\mathbf{k} = (k_1, k_2, k_3)$ of magnitude κ. This yields

$$\lambda^2 = \frac{k_1^2 + k_2^2}{k_3^2} = \tan^2 \psi, \tag{6}$$

stating that the wave vector makes an angle ψ with respect to the rotation axis, as is illustrated in figure 4.1. Together with the definition of λ (5), this implies that the wave frequency and the direction of the wavenumber vector angle are related via the ratio of angular and wave frequency, regardless of the wavenumber magnitude. The angle ϕ, the angle of the wave vector with the positive x-axis, is not restricted. So the wave vector lies on a cone with half opening angle ψ and is alternatively written as $\mathbf{k} = \kappa(\cos\phi \sin\psi, \sin\phi \sin\psi, \cos\psi)$.

The group velocity is given by

$$\mathbf{c}_g = -\frac{\omega}{\kappa^2}(k_1, k_2, -\lambda^2 k_3). \tag{7}$$

The group velocity vector is perpendicular to $\mathbf{k}$, with opposite horizontal component. The angle θ of the group velocity vector with the rotation axis is directly related to λ according to $\tan^2\theta = 1/\lambda^2$. Wave energy propagates along lines (wave rays) that are in the same direction as the group velocity vector. In analogy to the wave vector, the direction of the group velocity vector (wave rays) can be given as $(\cos\phi_g \sin\theta, \sin\phi_g \sin\theta, \cos\theta)$. Crests and troughs propagate away from the rays with rapidly-vanishing amplitude.

Regarding the chosen definition of ψ and θ, downward propagating waves will have negative values of ψ and θ, upward propagating waves will have a positive value. The absolute value of ψ and θ is conserved upon reflection. The term reflection will include refraction in the horizontal (change of ϕ).

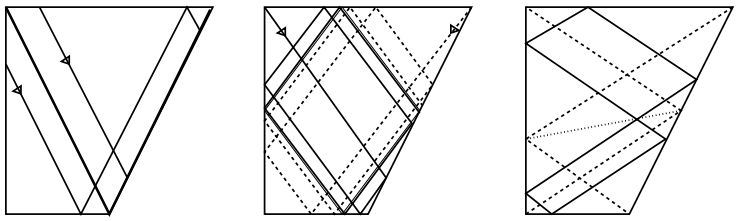

(a) critical slope *(b)* focusing *(c)* standing

Figure 4.2: Wave ray paths without refraction. *(a)* Critical reflection: wave rays are tangent to the slope after reflection. *(b)* Focusing, where every wave ray approaches the limit cycle (wave attractor). *(c)* Standing wave where for a single frequency all individual rays return back on themselves, and every ray intersects itself at the dotted line.

4.2.3 Solution in two dimensions

For a two-dimensional setting, a cross section of a channel that is uniform in one of the horizontal directions (y), we can take $k_2 = 0$ and $\phi = 0$, and the Poincaré equation reduces to the wave equation, albeit in two spatial coordinates instead of in time and space. The resulting problem is a boundary value problem. The waves still obey the above conditions regarding the constraint on the direction of propagation, and particle motion remains circular, according to equations (1).

For some basin shapes, the wave equation is easily solved using separation of variables. If this is not possible, in two dimensions, the method of characteristics can be used (John, 1978). These characteristics can be identified with the spatial paths of the wave rays (time has been eliminated). The pressure on the boundary, together with the structure of the characteristics (wave rays) determines the solution in the interior. The value of the pressure on the boundary on every boundary point is divided equally over the two characteristics with positive and negative slope through this point. Along a characteristic, this partial pressure value is invariant, and in the interior the value of the pressure in each point is determined by the sum of the partial pressures of the two characteristics through this point. For the moment we only deal with wave rays and study their spatial structure, keeping in mind that this structure forms the framework of the true solution.

Due to the constraint on the direction of propagation, ray-tracing becomes straightforward. But the constraint has the consequence that wave rays are focused or defocused when reflecting at a sloping wall, while remaining parallel. Repeated focusing may then lead to the appearance of a limit cycle, to which all wave energy is attracted, it is therefore called the *wave attractor*. This is illustrated in figure 4.2 for a cross section of the basin as will be used in the experiments.

Figure 4.2(a) is the critical case. Wave rays with positive slope are parallel to the slope. For incident wave rays this leads to an immediate concentration of the wave rays along the slope upon reflection. For the specific geometry where the bottom width equals half the top width the critical slope is connected to the degenerate form of the (1,1)-attractor, resulting in a V-shaped pattern. The waves propagate upwards along the slope, reflect backwards at the vertex, and then reflect at the bottom where they will be reflected towards the upper left

corner. There they will be reflected back towards the lower right corner and become tangent to the slope again. All wave rays will become part of this closed ray, when they reach the slope. Therefore it is called the *critical slope attractor*. Wave rays with a slightly larger slope would be reflected upslope, and would approach the vertex in successive reflections at the top and the sloping wall. The vertex acts as a point attractor, no closed ray path exists. This situation is equivalent to the progression of internal waves on a sloping beach (Wunsch, 1969; Cacchione & Wunsch, 1974).

In figure 4.2(b) a higher frequency (larger value of $\tan\theta$) is considered. Successive reflections at the sloping wall, where downward reflection implies focusing, bring the wave ray closer to the central parallelogram, the wave attractor. This holds for any ray of this slope for the presented basin shape. A wave attractor is not restricted to a single angle θ but exists for a range of θ-values (window), although the parallelogram will be stretched. The window $[\theta_{min}, \theta_{max}]$ is bounded by the value of θ for which a ray that starts in the upper left corner ends in the lower right corner. In these cases the parallelogram has degenerated into a line. All these attractors with one reflection at the side wall and one at the top and bottom are called (1,1)-attractors, classifying the attractors by the number of reflections at the top/bottom and the (sloping) side wall (Maas *et al.*, 1997).

In figure 4.2(c), for a still higher frequency, every individual wave ray reflects back onto itself. Focusing at downward reflection is followed by defocusing at upward reflection, no net focusing exists. In particular, wave rays that start in an upper corner end in the corner below at the same horizontal side. This case is called a standing mode and exists for a single value of θ. The periodic orbits are classified as (1,2) standing mode, because they reflect twice at the side walls and once at top and bottom wall. In cylindrical containers, such modes for which rays close onto themselves are usually classified as 'resonant modes'. They are the most energetic modes which have increasing amplitude under sustained forcing, eventually leading to breakdown (resonant collapse, e.g. McEwan, 1970). For inertial waves in a tank with a sloping wall however, the amplitude of the (1,2)-mode was found to be stationary and the velocities were smaller than for the (1,1)-attractor (chapter 3). Therefore the term 'resonant' seems inappropriate here.

There are several windows with attractors, and isolated values of θ with standing modes. For the standing modes, closed ray patterns have an even number of reflections at the sloping wall, such that focusing will always be balanced by defocusing. The limit cycles (closed ray paths) for the attractors always have an odd number of reflections at the sloping wall, and net focusing occurs. The values of θ for which periodic ray paths exist (standing or attracting) are separated by values of θ for which no closed ray path exists and the rays fill the whole cross section.

In three dimensions there is no such analogy of wave rays and characteristics. But, motivated by the success of the wave rays in describing the structure of the solutions, we will study the behaviour of wave reflections in the horizontal direction. Although it is not possible to find full solutions in this way, following wave ray paths may yield elementary properties of the solutions. For this purpose, the effect of wave refraction upon reflection at a sloping wall must be studied.

4.2.4 Refraction of plane waves

The effect of interaction with a wall on the direction of a wave ray will be described explicitly. This is most naturally done in terms of the velocity (LeBlond & Mysak, 1978) using the condition that there is no flow through the boundary. We will closely follow the notation by Phillips (1963). He used geometrical arguments to construct the reflected wave, but here the properties of the reflected wave are calculated, since this enables us to visualize the effect of reflection for the full range of possible incident waves. An alternative formulation is given by Eriksen (1982) for inertio-gravity waves.

The velocity $\mathbf{u}$ of the incident wave is given by (Phillips, 1963)

$$\mathbf{u}_{in} = \mathbf{a}\cos(\mathbf{k}\cdot\mathbf{x} - \omega t) + \frac{1}{\kappa}\mathbf{k}\times\mathbf{a}\sin(\mathbf{k}\cdot\mathbf{x} - \omega t). \tag{8}$$

The vector $\mathbf{a}$ is related to the particle motion. Its magnitude A determines the particle orbit speed (amplitude of the wave) and $\mathbf{a} \perp \mathbf{k}$: particle motion is perpendicular to the wave vector to guarantee incompressibility. For a wave in the interior of the fluid, particles move along circles that are tangent to the cone $\mathbf{c_g}$. Apart from this constraint, the direction of $\mathbf{a}$ is arbitrary, since a shift in the direction merely implies a phase shift.

We consider reflection at a wall that makes an angle α with the rotation axis, sloping upward in the positive x-direction. Its normal $\mathbf{n}$ is then $(-\cos\alpha, 0, \sin\alpha)$. The reflected wave is given by

$$\mathbf{u}_{re} = \mathbf{b}\cos(\mathbf{m}\cdot\mathbf{x} - \omega t) + \frac{1}{\mu}\mathbf{m}\times\mathbf{b}\sin(\mathbf{m}\cdot\mathbf{x} - \omega t), \tag{9}$$

where $\mathbf{b}$, $\mathbf{m}$ and μ take the role of $\mathbf{a}$, $\mathbf{k}$ and κ respectively, including the incompressibility condition $\mathbf{b}\cdot\mathbf{m} = 0$.

In an inviscid fluid it is required that there is no flow through the boundary for all times and locations:

$$\mathbf{n}\cdot(\mathbf{u}_{in} + \mathbf{u}_{re}) = 0. \tag{10}$$

This yields the following conditions:

$$\mathbf{n}\cdot\mathbf{a} = -\mathbf{n}\cdot\mathbf{b}, \tag{11a}$$

$$\mathbf{n}\cdot\frac{1}{\kappa}\mathbf{k}\times\mathbf{a} = \pm\mathbf{n}\cdot\frac{1}{\mu}\mathbf{m}\times\mathbf{b}, \tag{11b}$$

$$\frac{k_3^2}{k_1^2+k_2^2+k_3^2} = \frac{m_3^2}{m_1^2+m_2^2+m_3^2}, \tag{11c}$$

$$\mathbf{n}\times\mathbf{k} = \mathbf{n}\times\mathbf{m}. \tag{11d}$$

The first two conditions are amplitude conditions; the second condition can be simplified by taking $\mathbf{a}$ coplanar with $\mathbf{k}$ and $\mathbf{n}$ resulting in $\mathbf{n}\cdot\mathbf{k}\times\mathbf{a} = 0$, which may be done without loss of generality since it affects only the absolute phase of the wave. This also removes the sign, that depends on whether the wave reflects sub- or supercritically. Subcritical reflection ($\theta < \alpha$) means that a wave ray that travels in the direction of the slope reverses its vertical direction

of propagation upon reflection, supercritical reflection ($\theta > \alpha$) means that the wave reverses its horizontal direction of propagation. The set of amplitude equations must be completed by imposing that $\mathbf{b} \perp \mathbf{m}$. The third equation arises from the conservation of frequency, the last equation states that the wavenumber components in the reflection plane are equal, and is alternatively formulated as $\mathbf{s} \cdot \mathbf{k} = \mathbf{s} \cdot \mathbf{m}$ with $\mathbf{s}$ the unit vector tangent to the slope. Equations (11c) and (11d) can be solved to yield $\mathbf{m}$.

The reflected wave has wave vector components

$$m_1 = \frac{(\tan^2\alpha\tan^2\psi + 1)k_1 + 2\tan\alpha\tan^2\psi\, k_3}{\tan^2\alpha\tan^2\psi - 1} \tag{12a}$$

$$m_2 = k_2 \tag{12b}$$

$$m_3 = \frac{-(2\tan\alpha\, k_1 + (\tan^2\alpha\tan^2\psi + 1)k_3)}{\tan^2\alpha\tan^2\psi - 1} \tag{12c}$$

The angle of the wave vector with respect to the vertical is conserved up to a sign, the wave can be reflected upwards or downwards. In particular, for a horizontal wall ($\alpha = \pi/2$) we find that $m_1 = k_1, m_2 = k_2, m_3 = -k_3$ and for a vertical wall ($\alpha = 0$) that $m_1 = -k_1, m_2 = k_2, m_3 = k_3$, no refraction occurs and the wave vector retains its magnitude. For arbitrary values of α, the wave is refracted, altering the value of $\phi = \arctan(m_2/m_1)$. Also the magnitude of the wave vector will be altered upon refraction, crests and troughs will be more closely together (focusing) or further apart (defocusing).

These results can then be used to find the amplitude. The amplitude can be found by solving $\mathbf{b}$ from equations (11a) and (11b) and $\mathbf{b} \perp \mathbf{m}$. In fact, the transmission coefficient, the ratio $R = B/A$ with A and B the magnitudes of $\mathbf{a}$ and $\mathbf{b}$, is more relevant in describing the action of (de)focusing. It can be expressed as

$$\frac{B}{A} = \left| \frac{1 + \cos 2\alpha\cos 2\psi + \sin 2\alpha\sin 2\psi\cos\phi}{\cos 2\alpha + \cos 2\psi} \right|. \tag{13}$$

For an incoming wave with angle ϕ, the angle of the reflected wave ϕ_{re} obeys

$$\tan\phi_{re} = \frac{(\tan^2\alpha\tan^2\psi - 1)\sin\phi}{\cos\phi(1 + \tan^2\alpha\tan^2\psi) + 2\tan\alpha\tan\psi}. \tag{14}$$

The above calculations were all in terms of the wave vector. For ray-tracing, the direction of the group velocity vector must be considered. The angle of the group velocity with the x-axis ϕ_g equals $\phi + \pi$, since the horizontal components of the wave vector and the group velocity vector are opposite. In figure 4.3(a) the ratio of the smallest angle with the positive or negative x-axis of the reflected and incoming wave ray is plotted as function of horizontal (ϕ_g) and vertical θ incidence angles. In the figures, $0 < \theta < \pi/2$ indicates a downward propagating incident wave, such that the upper part of the figure contains downward propagating waves (coming from above). Furthermore, for the upward propagating waves not the full range of θ and ϕ_g are allowed, as for values outside the bell-shaped region the rays would come from the back of the slope. The present configuration enables easy comparison with figures in chapter 3 where the absolute value of θ is used to classify the parameter space. The behaviour for $\phi_{g,in} < 0$ and $\phi_{g,in} > 0$ is equivalent, there is no asymmetry for wave

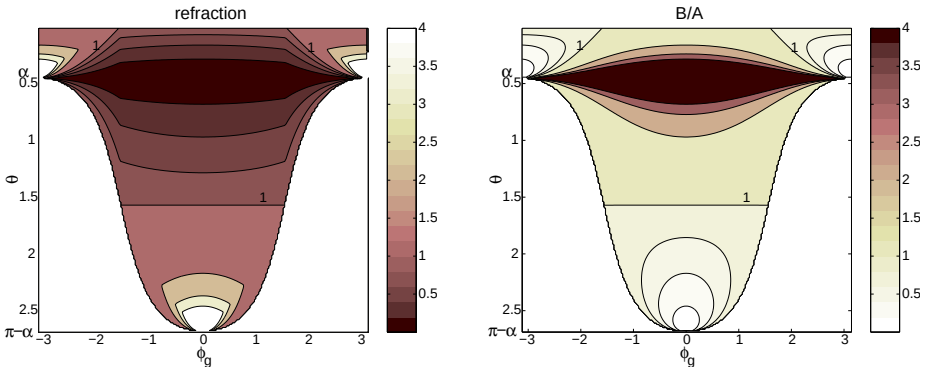

(a) *(b)*

Figure 4.3: Features of refraction for the slope that was used in the experiment ($\alpha = 0.45$). The unpatterned outer regions represents the parameters for which incident waves come from the back side of the slope and are therefore rejected. Here $\theta < \pi/2$ represents the *downward* propagating waves. *(a)* Ratio of the smallest angle with y=constant of the outgoing and incoming wave ray as a measure of the strength of refraction. *(b)* Transmission coeffi cient B/A. Contours are nonequidistant (0 0.25 0.5 0.75 1 2 3 4), in order to have a homogeneous distribution of contour values larger and smaller than 1.

reflection. Regions with ratio > 1 depict divergence in the y-direction, regions with ratio < 1 depict convergence.

In figure 4.3(b) the transmission coefficient B/A is plotted. Focusing takes place when $B/A > 1$, defocusing takes place when $B/A < 1$. This is necessary to guarantee conservation of energy flux: where wave rays are focused the wavenumber increases and the amplitude of the wave must increase to conserve the total energy flux. Where wave rays are defocused the wavenumber decreases and the amplitude must decrease.

A few regions can be distinguished. The most obvious features are that downward propagating wave rays which propagate towards the slope ($-\pi/2 < \phi_g < \pi/2$) converge in the horizontal upon reflection, but upward propagating waves diverge. These regions coincide with the parameter range for which waves are focused and defocused in the vertical respectively, and with the regions for which the amplitude increases and for which it decreases. Focusing is strongest is strongest for waves for which reflection is critical ($\theta = \alpha = 0.45$). For regions where the absolute value of ϕ_g is larger than $\pi/2$ (the incident wave ray propagating downslope) both focusing and defocusing in horizontal and vertical occur, depending on the exact angles. These waves come from above the wall, where they may reflect upwards and are defocused. Again focusing in the horizontal coincides with a increase in amplitude of the reflected wave and defocusing with a decrease.

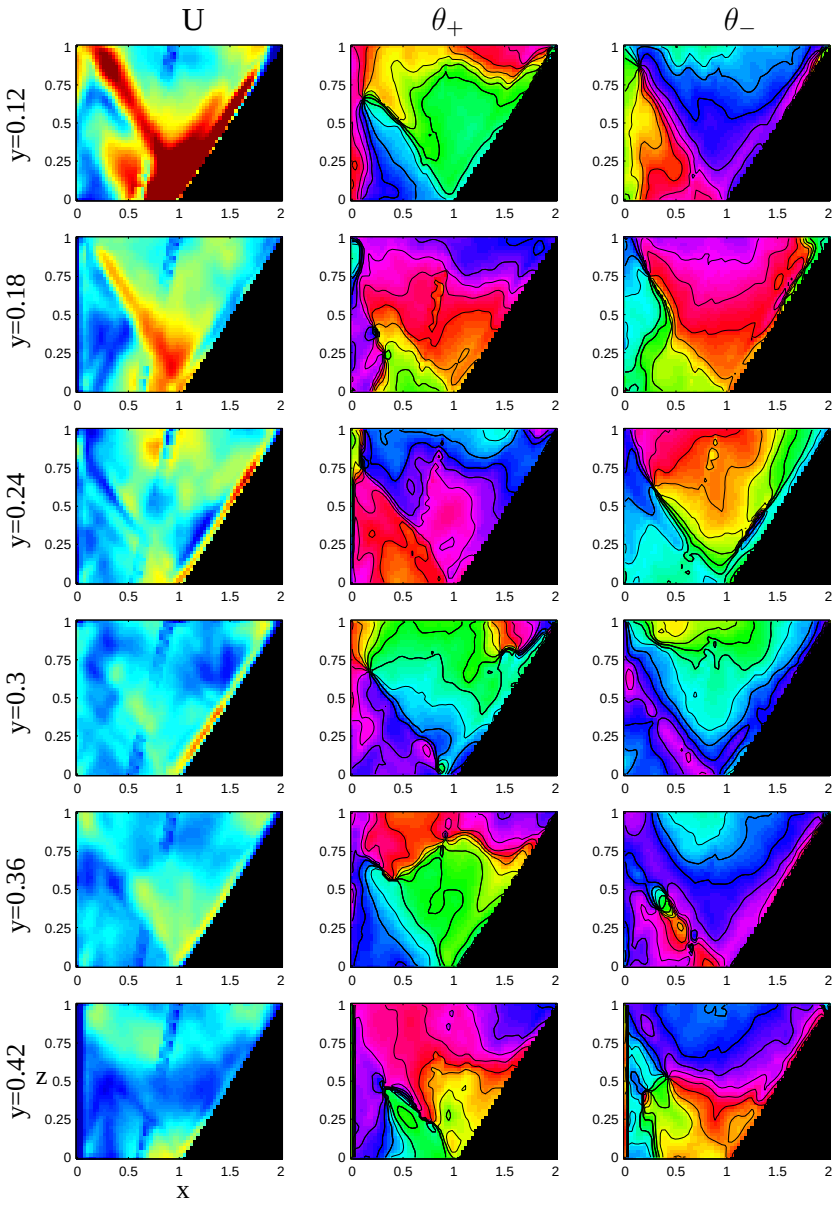

Plate II: Ellipse parameters U, θ_+ and θ_- for the critical slope attractor at $y = 0.12$, $y = 0.18$, $y = 0.24$, $y = 0.3$, $y = 0.36$ and $y = 0.42$. The scale for U ranges from 0 (dark blue) to 0.4 cm/s (dark red).

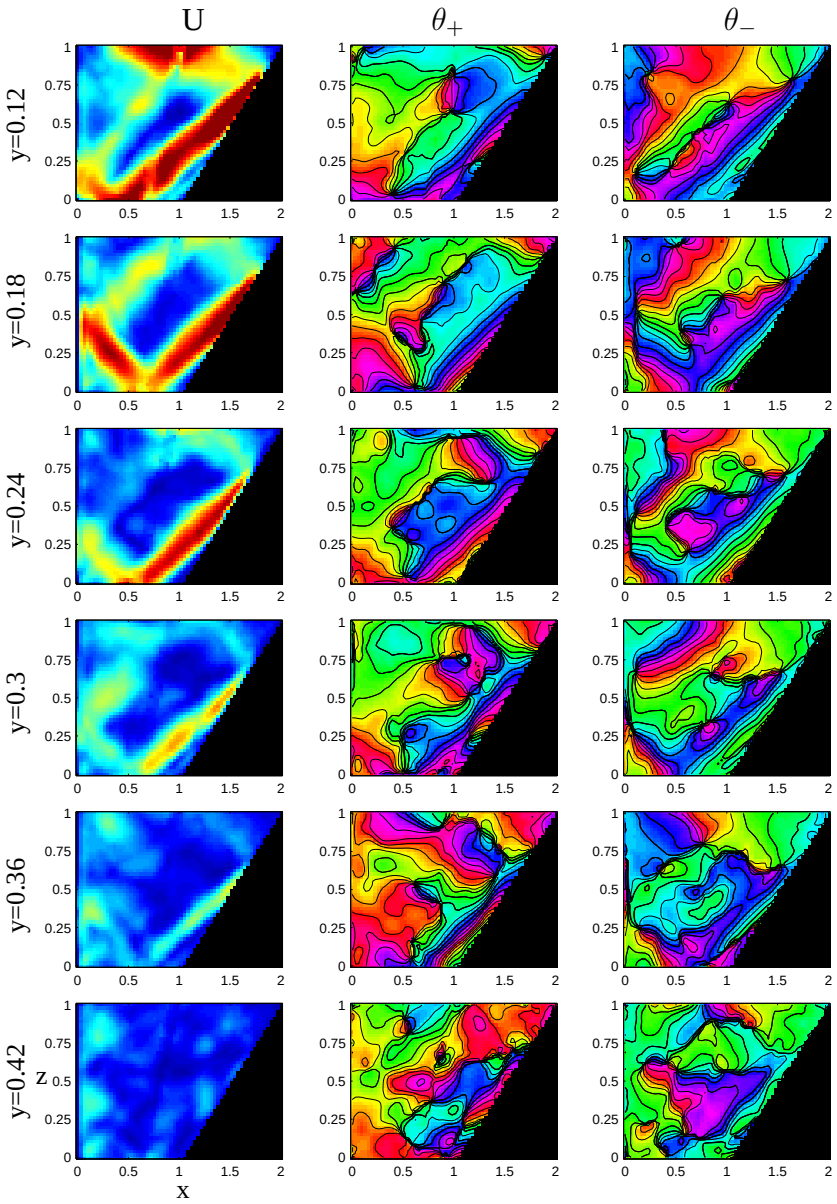

Plate III: Ellipse parameters U, θ_+ and θ_- for the self-similar attractor at $y = 0.12$, $y = 0.18$, $y = 0.24$, $y = 0.3$, $y = 0.36$ and $y = 0.42$. The scale for U ranges from 0 to 0.4 cm/s.

4.2.5 Three-dimensional ray-tracing

Now that the effect of a single reflection has been described, we will consider the fate of wave rays that experience many reflections. First, the behaviour in an infinitely long channel is investigated. Figure 4.4 shows rays with three different initial directions for the basin with sloping wall: (a) for subcritical reflection, (b) for the wave attractor and (c) for a standing mode. For the first two cases, convergence in the horizontal is achieved, for the standing wave rays do not converge and continue outside the depicted domain. Further, for the standing mode wave rays were observed that exhibit periodic behaviour in the y-direction, as they were reflected from the corner where the bottom and sloping wall come together and the pattern is 'retraced' in an xz-projection, but still with propagation in the y-direction.

Consider a wave ray with angle θ_{attr} within a window of an attractor $[\theta_{min}, \theta_{max}]$ and arbitrary ϕ_g. When the angle ϕ_g is reduced upon refraction such that the projection in the xz-plane, $\widetilde{\theta} = \arctan c_{g,1}/c_{g,3}$, is also within this window, convergence in the y-direction and the existence of an attractor is easy to understand. Focusing in the vertical occurs on the downward reflection at the sloping wall. Upon downward reflection at this wall ϕ_g becomes closer to π, the ray is refracted more towards $y = constant$, and $\widetilde{\theta}$ is closer to θ_{attr}. For subsequent reflections this converges further till $\phi_g \rightarrow \pi$ (or 0) and $\widetilde{\theta} \rightarrow \theta_{attr}$. Then the attractor is realized and the wave is trapped at a certain y-position. If $\widetilde{\theta}$ is not in this interval, then the attractor does not 'fit' in a two-dimensional cross section, but after a number of reflections the angle may be modified such that $\widetilde{\theta}$ is in the interval of existence of the attractor and convergence is again readily established. In contrast, for a standing mode, refraction at downward reflection is exactly balanced by refraction at upward reflection which makes it impossible to have convergence in the y-direction.

In figure 4.5, the y-position of the wave ray after 1000 reflections is indicated for rays emanating from a single starting position. Windows where wave rays have converged in the y-direction (attractors) are separated by intervals where no attractors, or very weak attractors for which convergence in the y-direction is slow, are present. In a band with an attractor there are some values of ϕ_g for which the ray propagates deep into the channel before eventually converging to a fixed y-position. This occurs when the wave ray is strongly refracted, such that for the refracted wave ϕ_g is close to $\pi/2$ and $\tilde{\theta}$ is small. This also implies that the ray reflects to the bottom and surface many times before it reflects at the slope again and can be refracted back. Some rays may reflect without ever converging in the y-direction. In interpreting the figure, one must note that only the final position is indicated, which is an indication for convergence, but not convergence itself. Thus, even in windows with standing waves, where no convergence can be expected, the final y-coordinate is not too large for waves that start with ϕ_g close to 0 or π.

The features can be partly explained by considering the combined effect of the steepness of the rays (steeper rays are subject to stronger refraction, increasing the strength of convergence in the horizontal) and the complexity of the attractor (the simpler the structure, the larger the window of existence of the two-dimensional attractor and the more likely the condition that $\widetilde{\theta} \in [\theta_{min}, \theta_{max}]$ is fulfilled and convergence towards a fixed y-position is realized). The asymmetry in y-position with respect to $\phi_g = \pi/2$ appears from the fact that waves with $\phi_g < \pi/2$ travel in the direction of the sloping wall and are focused directly, while the waves with $\phi_g > \pi/2$ travel to the vertical wall and are reflected a few times before

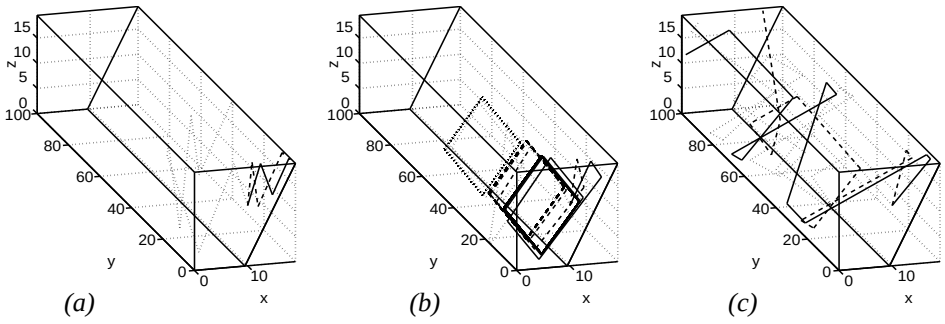

Figure 4.4: Progression and convergence of wave rays with $\phi_g = \pi/6$ (solid line), $\pi/3$ (dashed) and $5\pi/3$ (dotted) in a tank with sloping wall. *(a)* Subcritical reflection $\theta = 0.42$, *(b)* wave attractor $\theta = 0.63$, *(c)* standing wave $\theta = 0.97$.

the are focused, thereby travelling farther in the y-direction. For the weaker attractors, this difference in y-position is small compared to the total distance traveled in the y-direction.

Contrary to the two-dimensional case, where all waves approached the same limit cycle, regardless of their initial position, the final position of a ray is now very sensitive to the initial position and direction. This is expressed by the speckled appearance and the narrow bands of slow convergence in windows with attractors. The attractor is no longer a single limit cycle, but a limit surface to which wave rays approach. The manifestation of a standing wave in terms of wave rays that close onto themselves becomes questionable, as periodic orbits only exist for waves that do not propagate in the y-direction. The presence of a vertical wall at a fixed y-position would not alter the main results, since it would simply reverse the sign of k_2 and not the convergence behaviour, that is dependent on k_1 and k_3. However, closing the basin may result in isolated closed rays, connecting the corners of the basin. For standing waves, these are the only closed rays apart from the ones that do not propagate in the y-direction from the beginning. For attractors these closed rays are among the rays that do not approach an attractor. Their role is as yet unclear, they may play a role in the horizontal structure of the solutions in a closed basin.

4.2.6 Towards three-dimensional solutions

Ray-tracing illustrates the possibility of trapping of wave rays on an attractor at fixed y-position. However, it is not said that such patterns are physical solutions. It is for example possible, that in a fully enclosed tank the wave ray converges to an attractor at the vertical wall at $y = 0$. On the attractor, particle motion is large and also has a component in the y-direction, which violates the boundary condition of no motion through the boundary. Only the sum of all possible rays will describe the actual wave field. The phase will determine to which amplitude they add up locally.

For the axial cylinder (Kelvin, 1880) and the full sphere (Bryan, 1889), solutions to the Poincaré equation are known and their validity has been tested in the laboratory (Fultz, 1959; Aldridge & Toomre, 1969). For a horizontal rectangular tank, the structure of the three-

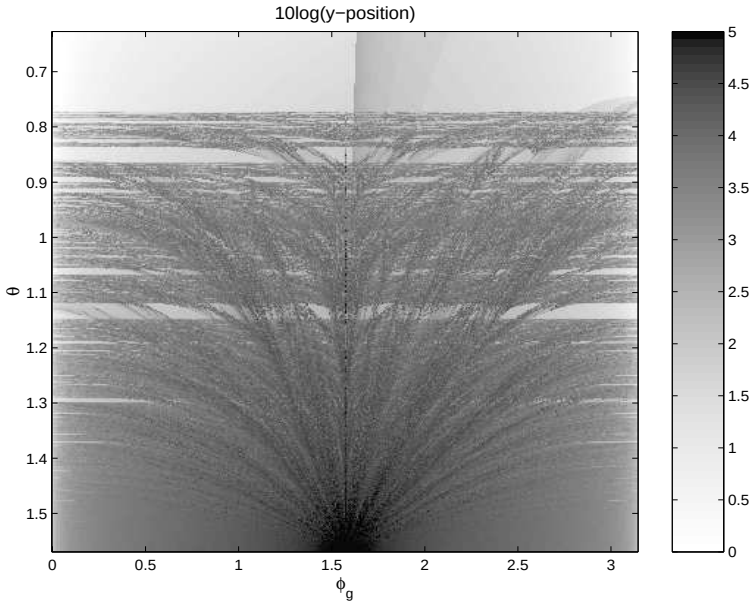

Figure 4.5: Final position of wave rays after 1000 reflections in an infinitely long basin of cross section equal to that in figure 4.2. All rays start at the same point (slightly above the middle of the cross section), in a downward direction. The subcritical reflection ($\theta < \alpha = 0.45$) and part of the (1,1)-window ($0.45 < \theta < 0.77$) are left out, since in these cases for all angles convergence was readily established.

dimensional wave field has been solved by Maas (2003). There, the Poincaré equation can be attacked by assuming standing waves in the vertical. The horizontal structure is then governed by a Helmholtz equation. It can be solved by a sum of fully internal (maximum vertical velocity in the interior, rigid lid) Kelvin and Poincaré waves, restored by the Coriolis force alone. Depending on the frequency, they yield amphidromic structures and standing wave patterns complementary to their classical free surface archetypes where gravity dominates (LeBlond & Mysak, 1978). Important features of the modes in the horizontal are the relatively large scale structures in the interior with rapid changes near the boundaries, and increasing mode number for decreasing frequency. Although these solutions do not apply for the tank with sloping side wall, they give an idea of what kind of structures would be possible in the horizontal direction. Laboratory experiments will help to answer to our questions regarding the three-dimensional structure of inertial wave fields.

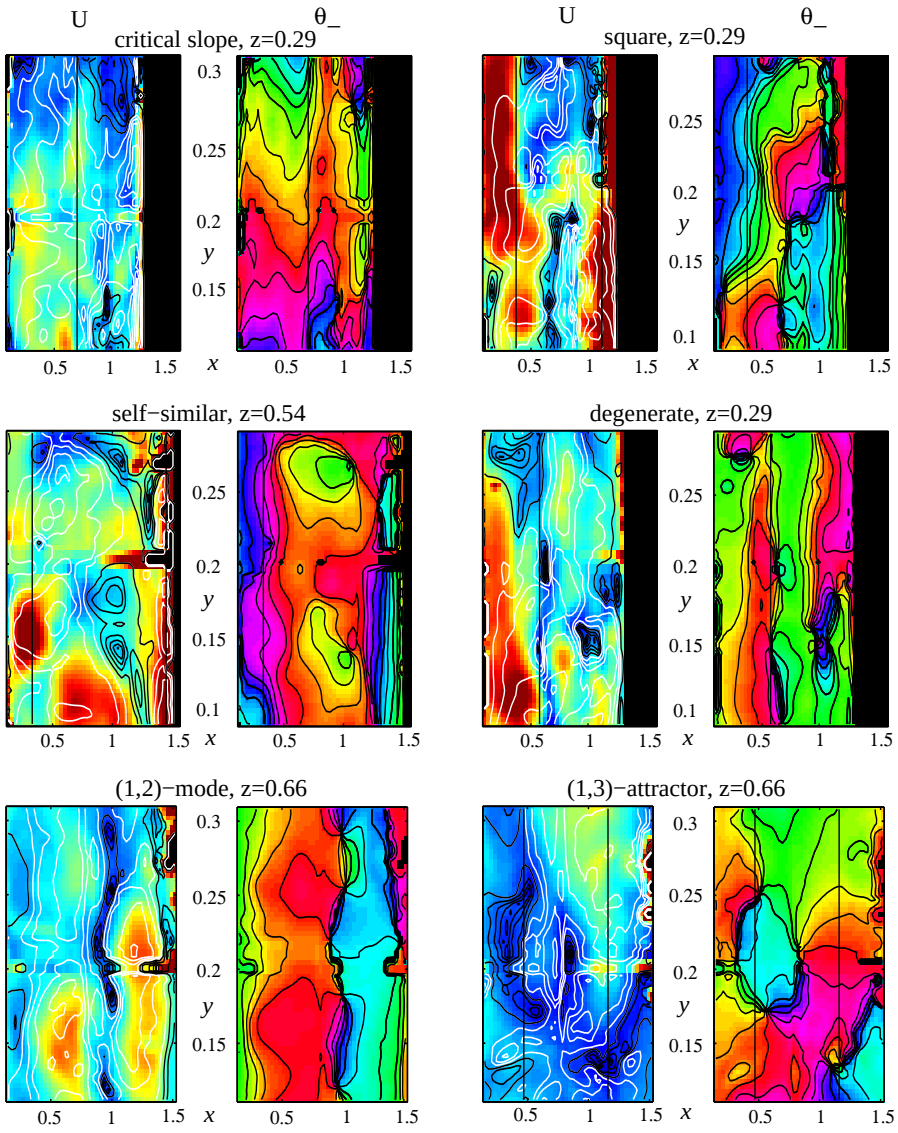

Plate IV: Horizontal cross sections: ellipse parameters U and θ_-. The critical slope, square and degenerate attractor are shown at $z = 0.29$, the self-similar attractor is shown at $z = 0.54$ and the (1,3)-attractor and the resonant mode at $z = 0.66$. The black lines indicate the intersections with the theoretical 2-D attractor. The scale for U ranges from 0 (dark blue) to 0.4 cm/s (red), white contour lines indicate areas of clockwise motion, black lines of anticlockwise motion. The scale for θ_- is periodic. The black area to the right is the sloping wall. Slight perturbations around $y = 0.2$ are due to the frames around the glass plates.

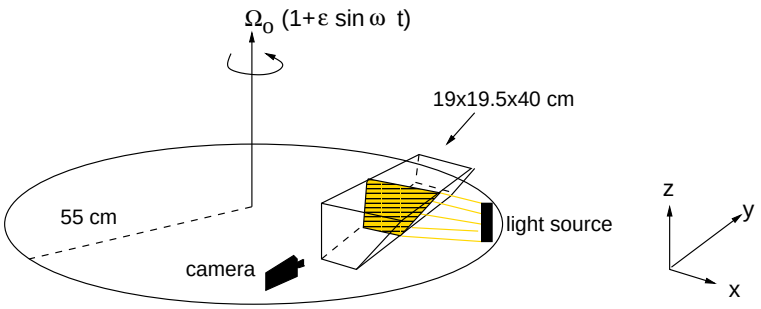

Figure 4.6: Experimental set-up

name	ω	$\omega/2\Omega_0$	$\tan\theta$
critical slope	0.6057	0.4382	0.4872
parallelogram	0.8156	0.5900	0.7303
(1,2) standing	1.1410	0.8255	1.4617

Table 4.1: Experimental modulation frequencies and corresponding parameter values

4.3 Experimental set-up

Experiments were performed in a perspex tank of width $2B$=19 cm, height $H_0 = 19.5$ cm and length $L = 40$ cm. The tank was provided with a sloping wall from the top to half way the bottom, so that the tank effectively has bottom width B and top width $2B$, and it had a rigid lid. It was filled with homogeneous fluid (ordinary tap water), that was thus fully enclosed.

This tank was placed excentrically on a rotating table of radius $r = 55$ cm. Figure 4.6 illustrates the set-up. The rotating table had an angular velocity $\Omega_0 = 0.6912$ rad/s. This rotation rate was modulated according to $\Omega(t) = \Omega_0(1 + \epsilon\sin(\omega t))$ to generate waves with frequency equal to the modulation frequency ω. The small parameter ϵ had a value of 0.1. The critical slope situation, the parallelogram shaped attractor and the (1,2)-resonant mode were investigated. Table 4.1 displays the forcing frequency, the ratio of wave frequency to twice the rotation frequency and $\tan\theta$.

For flow visualization the fluid was seeded with small, almost neutrally buoyant particles. The fluid was illuminated with visible light (slide projectors) shining through a slit in the black covering of the tank. This slit had a width of about 1.5 cm. The motion was recorded by a digital camera and, via particle tracking velocimetry (van der Plas & Bastiaans, 2000), velocity fields were obtained.

Measurements were taken in horizontal cross-sections (camera above the fluid, horizontal slit) and vertical cross-sections (camera in front of the tank, vertical slit, as in figure 4.6). These horizontal cross-sections were distributed evenly over the fluid: horizontal cross-sections were taken at $z = 5$, 10 and 15 cm for all frequencies. Vertical cross-sections were taken at $y = 20$ and $y = 3$ cm for all frequencies. At $y = 10$ cm only the critical slope

and the parallellogram shaped (1,1)-attractor were measured. The latter was measured again at $y = 30$ cm.

The frame rate of the camera was 30 Hz, which was reduced to an effective frame rate of 7.5 Hz in the processing of the data to velocity fields. The resulting time series consisted of about 240 vector fields, spanning about 33 seconds, so 3 to 6 wave periods. The particle tracking results were interpolated to obtain velocity fields on a structured grid with a spatial resolution of 0.5 cm.

A led-light was used as an indicator for the phase of the sinusoidal forcing. Knowledge of the exact phase of the data enables us to compare observations of the phases in different cross-sections and to compensate for the vorticity-conserving flow. Using the theoretical prediction of the vorticity-conserving flow field, of which the strength will vary sinusoidally in time, this flow can be subtracted from the observed flow field to reveal the wave field. Its amplitude must be matched with the experimental data.

Measurements were taken some time (10 min) after the onset of rotation and modulation to give the system time to evolve to what appears as a quasistationary state. The advantages of using such a small basin (as compared to the basins used in Maas (2001) and chapter 3) are that the time for spin-up and evolution of the wave field is shorter and, more important, that the full horizontal cross-section can be captured, which was not possible in the previous experiments. This enables the study of the horizontal structure of the wave field.

4.4 Results

The results are presented in terms of dimensionless coordinates. To facilitate comparison with chapter 3, the same conventions are applied. This means that the scaled coordinates (x', y', z') are defined as $x' = x/B$, $y' = y/L$, $z' = z/H_0$. Primes will be dropped in the rest of the text.

The horizontal cross-sections and the vertical cross-section at $y = 1/10$ must be corrected for the vorticity-conserving flow, since in these cross-sections the vorticity-conserving flow dominates the vector field. The synthetic flow field of the vorticity-conserving flow is based on the shallow-water approximation. This is applicable when $(H_0/L)^2 \ll 1$ and $B/L = O(1)$. For our experiment $(H_0/L)^2 = 0.24$ and this field is illustrated in figure 4.7. For the other vertical cross-sections this flow is mainly directed along the y-axis, the contribution to the flow in the xz-plane is negligible.

The synthetic flow field of the vorticity-conserving flow is based on $B/L = 0.48$. This implies that the theoretical flow field is a reasonable approximation of the true field but small deviations can be expected. Such deviations were indeed found. Upon matching the amplitude of the synthetic flow field to the real flow field, it appeared that the strength of the vorticity-conserving flow decreased with depth, instead of being constant. In addition, direct observations showed that the centre of the cell, that is above the flat part of the bottom (and not at $x = 1$) shifted a little towards $x = 0$ for decreasing z. This is in agreement with the results of van Heijst *et al.* (1994) who also observed a shift of the centre of the inviscid circulation cell towards the vertical wall in the solutions for the flow in a wedge-shaped tank, in the case that $(H_0/L)^2$ is not much smaller than 1.

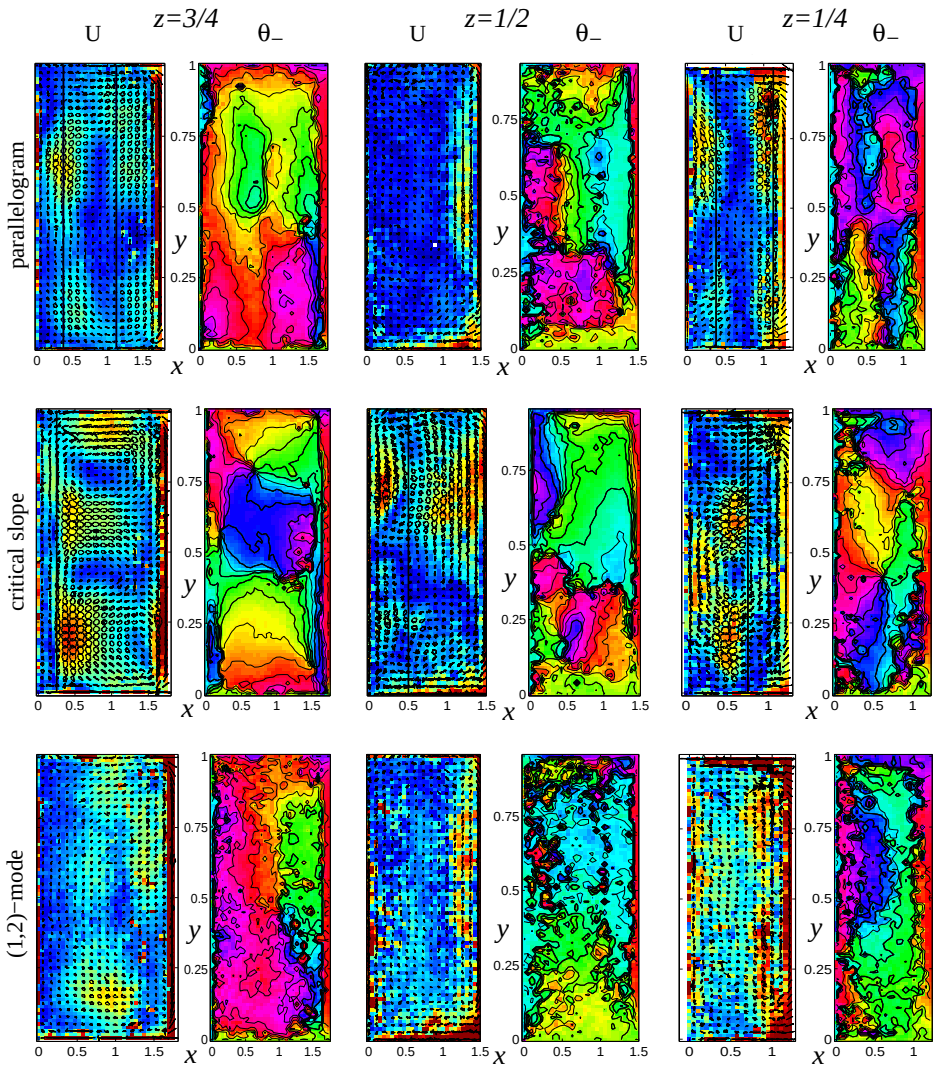

Plate V: Observed ellipse parameters U and θ_- in horizontal cross-sections at z =3/4, 1/2 and 1/4. Also hodographs of two wave periods are plotted, transparent for clockwise motion and fi lled for anti-clockwise motion. The parallelogram shaped attractor is shown in the upper panels, the critical slope attractor in the middle panels and the standing mode in the lower. The colour scale for U is from 0 (blue) to 0.2 cm/s (red) for the parallelogram and critical slope attractor, and from 0 to 0.1 cm/s for the standing mode. The phase is plotted in a cyclic color map. Black lines in the pictures of U indicate the location of the theoretical two-dimensional attractor.

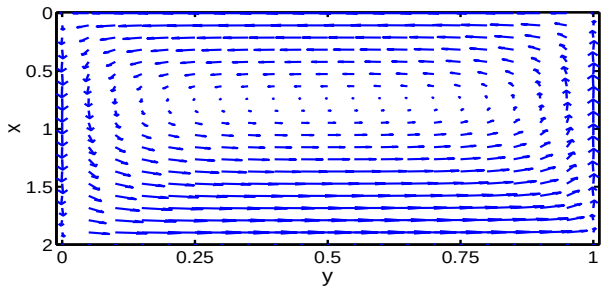

Figure 4.7: Theoretical prediction of vertically-uniform, vorticity-conserving flow field, based on the shallow-water approximation (see chapter 3). The slope is from $x = 1$ to $x = 2$. The flow field is not symmetric with respect to $x = 1$. The amplitude scale is arbitrary.

For correction of the horizontal cross-sections the matched amplitudes can be used. For the vertical cross-section at y =1/10, a linear change in amplitude with depth is used, based on the change in amplitude in the horizontal cross-sections. The amplitude is then given by $A = 0.001 * z + 0.023$ with z the level in centimeters. The shift in centre position was not accounted for as it was a minor effect.

It appeared that the most dominant features in the velocity field due to the vorticity-conserving flow can be eliminated using this simple model and there is no direct need for a more sophisticated model. The remainder contained weak vortices over the flat part of the bottom, that are also encountered in van Heijst *et al.* (1994), and a weak mean flow due to mixing of angular momentum near the slope, where energy is concentrated (Maas, 2001). Their velocities were smaller than those associated with the attractors and standing wave, and were therefore neglected in the study of the wave field.

To analyse the wave field, time series of the the tips of the velocity vectors (hodographs) were plotted. They appeared to be of elliptical shape, varying between nearly circular and nearly rectilinear. When hodographs were plotted over more than a period, patterns appear to be retraced almost exactly, which means that a stationary state is established and that the forcing frequency was by far the dominant frequency in the spectrum.

This justifies the description of the velocity field in terms of ellipse parameters, that summarize a whole time series. We will only give short definitions here, for more details we refer to Maas & van Haren (1987) and chapter 3. The ellipse is characterized by its long and short axis U and V, its orientation Ψ and its phase angle at $t = 0$, Φ. For clockwise motion (Φ decreasing in time) the value of V is negative. Although this is a clear graphic way of summarizing the time series, it is often problematic. When motion is nearly circular, Ψ is very sensitive to the relative strength of the two components of motion, which may lead to phase jumps of $\pi/2$. Furthermore, the same ellipse may be characterized by two values of Ψ that differ a factor π, at the expense of the more physical differences of π in Φ. This makes the pictures difficult to interpret, especially of locations where the shape does not change but the phase changes rapidly, like on the attractor. Therefore, this ellipse was decomposed into two circles of clockwise and anticlockwise rotation sense with radius W_+ and W_- and phase at $t = 0$ θ_+ and θ_-, respectively. A sketch is shown in figure 4.8. In this decomposition the

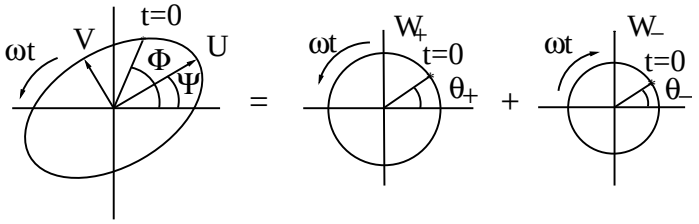

Figure 4.8: Definition of ellipse parameters

phase jumps disappear.

4.4.1 Vertical cross-sections

First, we discuss the *parallelogram shaped attractor*, since this (1,1)-attractor is the elementary form of a wave attractor. Velocity observations in vertical planes were obtained at y=1/10, 1/4, 1/2 and 3/4. In figure 4.9, the hodographs are plotted for two wave periods on a 1 cm grid with the major axis of the ellipse U in grey shades on the full grid in the background. Further θ_+ and θ_- are plotted. When interpreting the figure, one should note that the long axis U of the hodograph is a measure of the strength of the motion, rather than the area enclosed by the ellipse. The parameters θ_+ and θ_- do not represent the actual phase of the waves, since only projections of the three-dimensional wave field are observed. But they provide insight in the phase propagation patterns and relative phases.

The attractor is visible at all four y-positions, but there are differences in shape and strength. At $y = 1/10$ the attractor is very weak and in the middle there is relatively large circular motion, which is absent at the other y-positions. This might partly be due to imperfections in our correction for the vorticity conserving flow, but this does not explain the vertical motion. Purely vertical motion in the middle is present at $y = 1/2$.

At $y = 1/4$, the attractor is deformed slightly, it becomes more rectangular than square-like. Such a deformation was also reported in chapter 3 near $y = 1/8$, as well as the strong motion near the top wall. The branch of the attractor (i.e. part of the attractor connecting two reflection points) from the slope to the bottom is relatively strong. At $y = 1/2$ the attractor is less strong. Noteworthy is the dark line of nearly no motion along the bottom left part of the attractor, for which we do not have an interpretation. Phase lines are clearly parallel to the attractor, in agreement with the theory that phase propagation is perpendicular to energy propagation, with opposite horizontal component. This is less clear at the other cross-sections, where parallel phase lines are only present in part of the section, possibly due to three-dimensional character of wave propagation. At $y = 3/4$ the attractor is very strong, with almost linear hodographs aligned along the attractor. In chapter 3, hodographs were also linear and aligned along the attractor. In all sections circular motion can be observed near the reflection points. Linear interaction between incoming and outgoing waves yields anticlockwise motion at the top and bottom reflections and clockwise motion at the side wall reflections, as observed. The cross-sections at $y = 1/10$ and $y = 1/4$ roughly have the same phase values $\theta_\pm$, that differ nearly by π from the phases at $y = 1/2$ and $y = 3/4$. The

latter two have identical phases on the lower two branches of the attractor, but differ in the branches, for θ_+ even by π in the middle of the section.

The *critical slope attractor* is shown in figure 4.10. The triangular shape can be identified in all three figures of U, although the left branch is not visible as a a line of strong motion but as a line of weak motion. This is probably a result of strong shear due to opposed particle motion above and below the attractor. The hodograph patterns vary in the y-direction. Regions of clockwise and anticlockwise motion are separated by the attractor, and at $y = 1/10$ regions of clockwise and anticlockwise motion are interchanged as compared to $y = 1/2$. In between, at $y = 1/4$, the circular motion is more towards the middle, anticlockwise to the right and clockwise to the left. At $y = 1/2$, on the attractor itself the motion is nearly purely vertical, in the centre of the V-shape the ellipses are deformed such that they are curved, which points at motion with twice the forcing frequency, typical for nonlinear advection. Dauxois & Young (1999) take nonlinear advection for critical reflection of internal gravity waves into account to heal the infinite concentration of energy at the slope. Phase lines are mostly parallel to the attractor, or the phase changes rapidly across the attractor. The phase lines near the slope at $y = 1/2$ indicate downward propagating energy directly at the slope. Overall, the change of rotation sense and shape for the hodographs in the along-channel direction suggest that the wave field has a strongly three-dimensional character.

For the *(1,2) standing wave*, the two vertical sections are shown in figure 4.11. At both sections, motion is much weaker than for the two attractors by about a factor two. At $y = 1/10$, only in the triangular region between the sloping wall and the line connecting the upper right to the lower right corner (see figure 4.2) motion is significant. It is circular and clockwise. At $y = 1/2$ the two lines connecting the upper right and left corner to the lower right and left corner, respectively, divide the section in different regions with alternatingly clockwise and anticlockwise hodographs. Especially in the upper right part adjacent to the sloping wall, motion is strong and circular (clockwise). Where these lines cross each other motion is close to zero. The lines connecting the upper right corner to the lower right corner divide the section into a more and a less energetic part, where the lower (more energetic) part is subdivided by the line from the lower left corner. The phases θ_+ and θ_- vary only slowly at $y = 1/10$, but at $y = 1/2$ they vary clearly, being parallel to the lines connecting the corners at $y = 1/2$ and reproducing the pattern of U. There is no clear phase propagation direction predicted for the standing wave, phase changes are supposed to take place at the same moment in time over the full cross-section. Phase changes are partly associated with the change of velocity directions, that vary more than in case of an attractor. In the direct observations of phase propagation, the phase behaviour is not as clearly of standing character as observed in chapter 3, although the patterns of θ_+ and θ_- themselves are comparable.

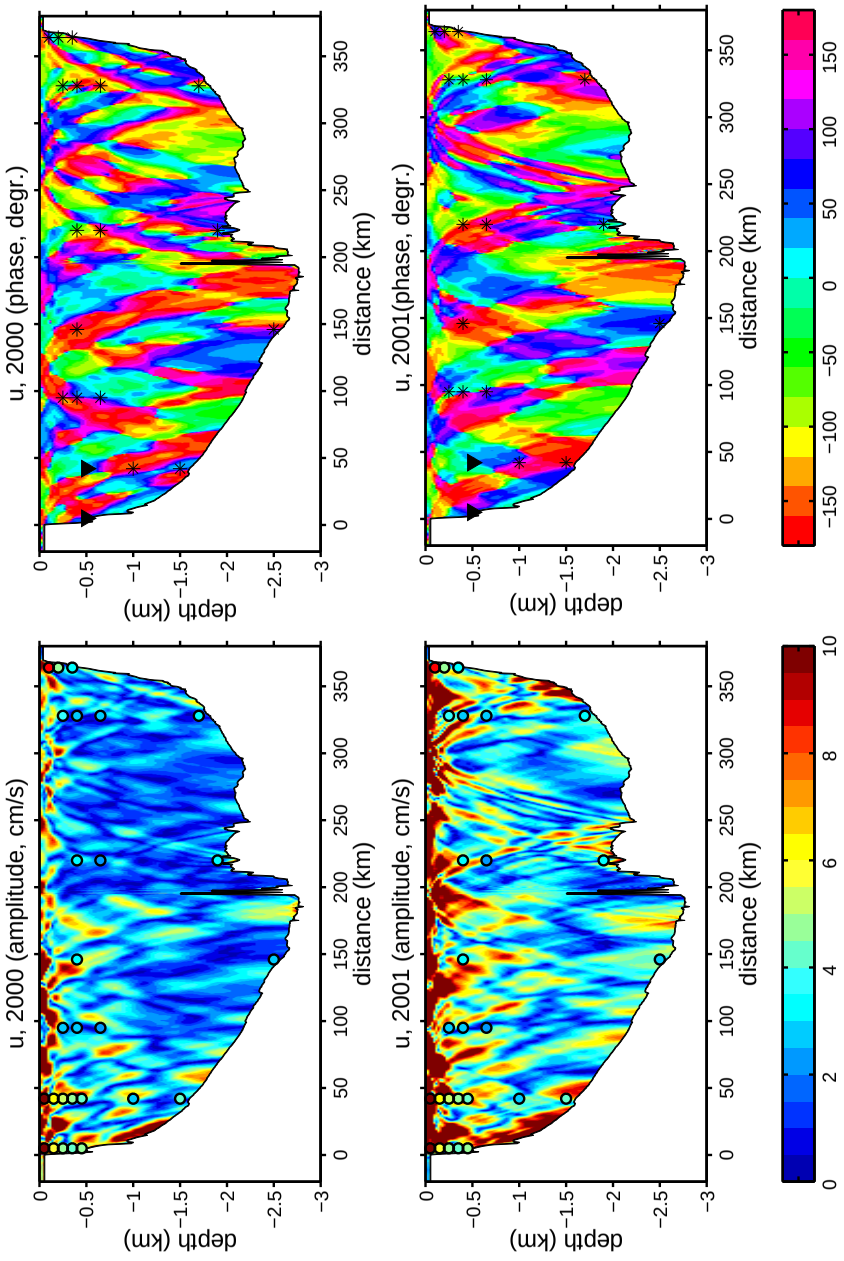

Plate VI: Amplitude (cm/s, upper panels) and phase (lower panels) of the velocities from the numerical internal-tide generation model, for both stratification regimes. Filled circles are the observed amplitudes, calculated from the integrated spectra of the semidiurnal band. Stars and triangles indicate the position of the ADCP's and the current meters in the phase pictures.

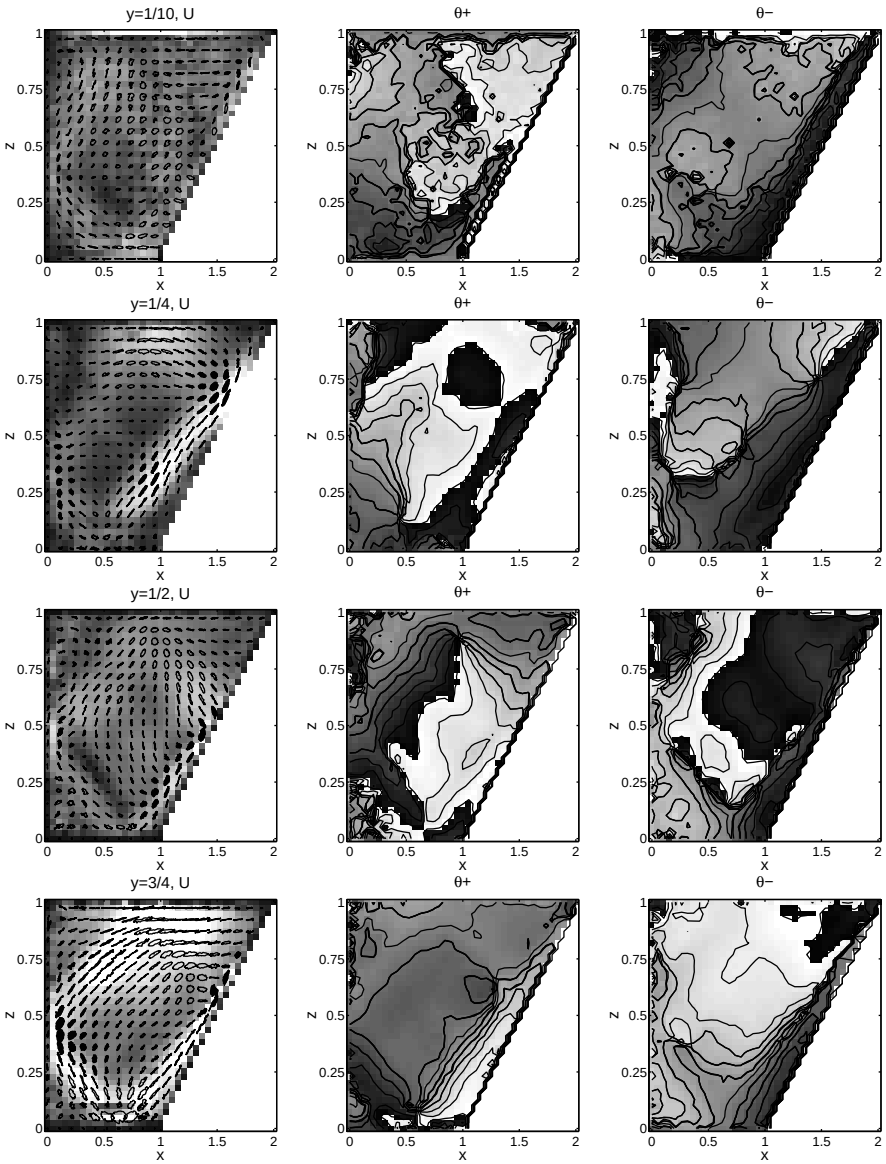

Figure 4.9: Observed ellipse parameters and hodographs for parallelogram shaped attractor. Scaling for U ranges from 0 (black) to 0.15 cm/s (white). Filled hodographs are traversed anticlockwise, transparent hodographs are traversed clockwise. The phase angles θ_+ and θ_- range from -π (black) to π (white). This causes the shock-like transition from black to white, which is in physical reality a smooth and continuous phase transition.

4.4.2 Horizontal cross-sections

The parameters U and θ_- for the horizontal cross-sections are plotted in plate V, together with the hodographs. It appears that motion is dominantly clockwise and the phase is almost

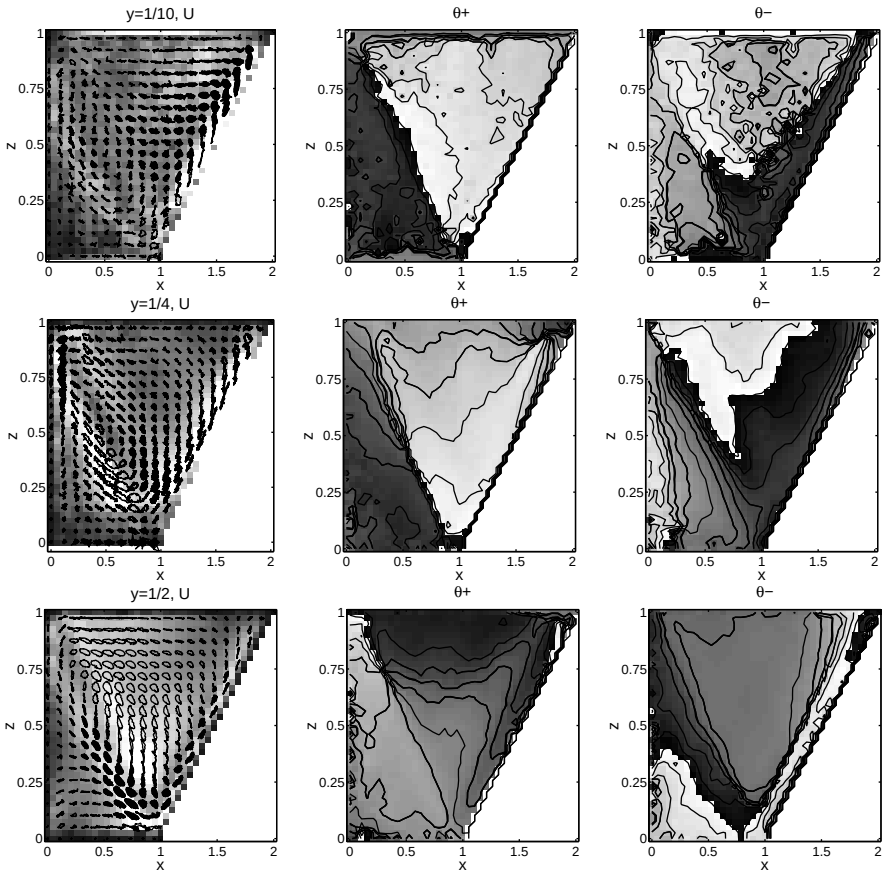

Figure 4.10: As in fi gure 4.9 for the critical slope attractor.

fully described by θ_-, therefore θ_+ was omitted. Only in regions of very weak motion this is not the case, but then noise may dominate. Near the walls, in a real fluid the velocity will be zero due to friction. However, the theoretical vorticity-conserving flow is inviscid and has maximum velocity at the walls. Then subtracting the vorticity-conserving flow gives an over-correction, resulting in unphysical strong motion of uniform phase near the walls. Further, the measurements are slightly less accurate near the walls, since due to light reflection at the perspex walls the contrast between background and particles decreases. In the rest of the section the correction works well, according to the circular hodographs, since the (correction for the) vorticity-conserving flow would give rectilinear motion which is not or hardly observed here.

Cross-sections of the *parallelogram shaped attractor* (plate V, upper panel) clearly have four regions of stronger motion at $z = 1/4$ and $z = 3/4$. Their x-position can be associated with the location of the theoretical (two-dimensional) attractor. At $z = 3/4$ the left part is in excellent agreement, at $z = 1/4$ it is the right part that coincides well with the prediction. In

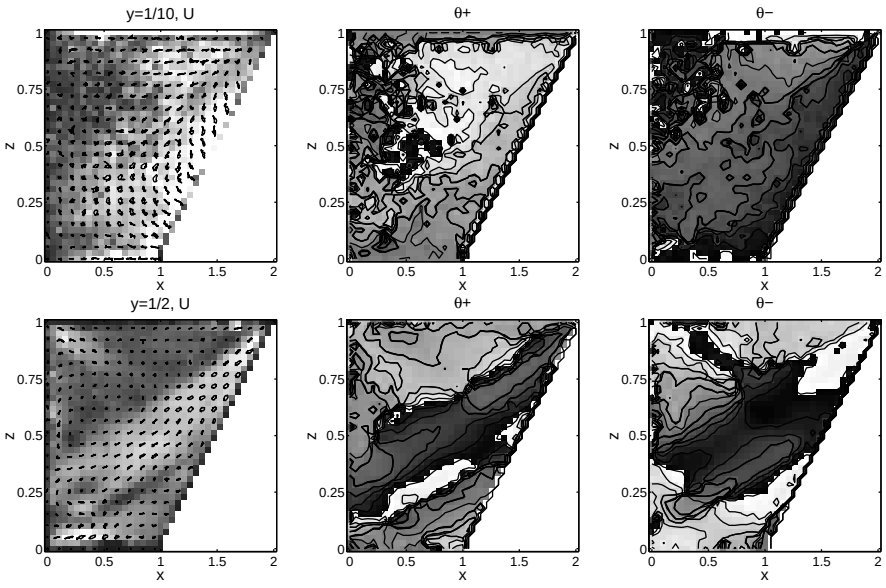

Figure 4.11: As in fi gure 4.9 for the (1,2) standing wave, except for the scaling of U that is now from 0 (black) to 0.075 cm/s (white).

the middle motion is weak. The phase pictures reproduce the four regions. For $y < 0.45$ and for $y > 0.45$ the left and the right part almost have the same phase, which can be interpreted in terms of the two branches of the attractor that must have the same phase in the x-direction. In the y-direction the phase difference between the parts $y > 0.45$ and $y < 0.45$ is about π for the sections at $z = 1/4$ and $z = 3/4$. At $z = 1/2$ the pattern is more or less in between the patterns of $z = 1/4$ and $z = 3/4$, that differ by a factor π. This is in accordance with the idea of energy propagation along the attractor with corresponding phase propagation towards the sloping wall for $z > 1/2$ and towards $x = 0$ for $z < 1/2$. At $z = 1/2$ motion is weak, except near the sloping wall where the attractor is predicted to reflect. Surprisingly, there the motion is strongest around $y = 1/2$ and $y = 0$. The phase picture does not exhibit the antisymmetric structure around $y = 0.45$.

The horizontal cross-sections of the *critical slope attractor* (middle panels) have a completely different structure. There are regions of strong circular motion, at $z = 3/4$ and $z = 1/4$, that have their maximum close to the theoretically predicted attractor. But there are also nearly motionless regions. Hodographs are more or less aligned around these regions. Phase lines tend to come together in the motionless, so-called amphidromic points, most clearly visible at (x, y) =(0.6,0.8) at $z = 3/4$ and (0.6, 0.4) at $z = 1/4$. At $z = 3/4$ there is phase propagation towards the vertical walls at $y = 0$ and $y = 1$, the wave length appears to be 1/2 in the y-direction. At $z = 1/2$ the structures are difficult to interpret. At $z = 1/4$ the structure is dominated by the amphidromic point. This point also corresponds with the purely vertical motion observed in the cross-section at $y = 1/2$ around $(x, z) = (1, 0.25)$ (figure 4.10). Such points of purely vertical motion are found in sloshing-mode solutions for

the rectangular basin (Maas, 2003).

The *(1,2) standing wave* (bottom panels) is weaker than the two attractors, as also observed in the vertical cross-sections. Motion is strongest near the sloping wall, and around $(x, y) = (0.8, 0.15)$ at $z = 3/4$ but there are no such prominent 'gaps' in the y-direction like for the two attractors. One can see smooth phase changes in the x-direction, as already noticed in the vertical cross-section, but in the y-direction the phase is nearly uniform. Because the motion is so weak, the effects of noise become more important, resulting in more irregular patterns. However, the large scale structures are still coherent, which gives the results more credit.

4.5 Discussion

The observed wave fields showed three-dimensional behaviour for the three different frequencies. This behaviour was not only frequency-dependent in vertical cross-sections, but also in the horizontal. In this section, the results are interpreted and compared with results from ray-tracing, previous experiments and theoretical solutions for a horizontal rectangular tank. Also an estimate will be given of the process that determines the width of an attractor, using present results and observations from earlier experiments.

4.5.1 The three-dimensional wave field

The *parallelogram shaped attractor* was clearly visible, with maximum intensity near $y = 1/4$ and $y = 3/4$ and a phase difference of π in the horizontal direction with the transition at $y = 0.45$. Waves propagate in the xz-plane, but are of standing nature in the y-direction. Part of the behaviour can be explained by considering ray-tracing. Ray-tracing predicts the formation of limit cycles where wave energy is concentrated due to focusing upon downward reflection combined with convergence in the horizontal due to refraction. The convergence in the horizontal direction could explain the high intensity at $y = 1/4$ and $y = 3/4$, which is not far from the generation areas, that are supposed to be near $y = 0$ and $y = 1$ where the vorticity-conserving flow has a considerable cross-slope component. This is supported by similar observations in the larger tank (chapter 3), where the attractor was strongest near $y = 0.12$ and waned towards $y = 0.5$, with uniform phase. In contrast, for forcing with a paddle, that was attached to the vertical wall and extended over the full length over the tank, the attractor became stronger towards the centre, $y = 0.5$, as discussed there.

Near the wall at $y = 0$, the attractor was hardly visible, although the generation should be strongest there. Ray-tracing does not take into account particle motion, so that convergence onto an attractor near the end walls at $y = 0$ and $y = 1$, and an attractor in the interior are equally possible. Particle motion on the attractor is however necessarily three-dimensional, which prevents the existence of a real attractor in the vicinity of the end walls.

It would be interesting to consider the structure of an ensemble of rays, starting at different points (ideally related to the generation mechanism) and in different directions, and test if there are regions where the majority of rays have their limit cycle. Still, for a physically realistic solution, information about the generation and phase of the waves must be included.

Currently, ray-tracing fails to predict the standing wave behaviour, with one nodal line, in the y-direction and is no substitute for solving the Poincaré-equation.

It appears that motion in the part $y > 0.45$ is slightly stronger than for $y < 0.45$, and that the phase jump does not occur exactly in the middle. We do not have a satisfactory explanation for this. If the set-up is compared with experiments in which Rossby waves are studied, which have a much lower frequency, the (infinitesimal) slope is defined as north, such that $y = 1$ would correspond to the western boundary and one could speak of 'western intensification'. But contrary to Rossby waves, inertial waves do not have an asymmetry with respect to eastern or western propagation.

The shape of the *critical slope attractor* is visible in all xz-cross-sections, even at $y = 1/10$. Motion is relatively strong, which is probably due to the immediate focusing at the sloping wall together with immediate trapping in the y-direction. This could also explain that the attractor is visible in all sections. The interchange of locations with clockwise and anticlockwise motion (open versus filled ellipses, figure 4.10) between the sections of $y = 1/10$ and $y = 1/2$ and the in-between situation at $y = 1/4$ is remarkable. For this attractor there is clear phase propagation in the y-direction: from the interior ($y = 1/2$) towards the walls at $y = 0$ and $y = 1$. This implies energy propagation from these walls into the interior. The wave length seems to be 1/2 in this direction, although patterns are not symmetric with respect to 1/2. In chapter 3 it was also observed that the critical slope attractor was strong and that there was phase propagation (and energy propagation) in the y-direction. There the wave length was estimated to be 1/4 of 1/5. These wave lengths may be related to the horizontal aspect ratio of the tank, $2B/L$, which gives 0.475 for the actual basin and 0.214 for the larger tank, which are nearly exactly the observed wave lengths.

The *(1,2)-standing wave* has the weakest motion and the most simple structure in the y-direction: that of a standing wave without nodal lines. The relatively weak motion can be explained by the fact that wave rays do not converge; not due to focusing due to downward reflection, nor due to refraction in the y-direction. Only wave rays that do not propagate in the y-direction, and possibly some isolated rays, can return back onto themselves. At this point it must be mentioned that the role of rays that close onto themselves, as pointed out in the two-dimensional approximation, may not have an equivalent in three dimensions. Rieutord *et al.* (2001) show that the frequency belonging to the first axisymmetric mode in a full sphere does not yield periodic wave rays.

4.5.2 Modal solutions

The patterns in the horizontal plane of observation have some features in common with those computed for a horizontal rectangular tank by Maas (2003). In such a tank, no focusing takes place and the solution can be determined mathematically. There, motion is dominantly clockwise, except in amphidromic points and near the boundaries at $y = 0$ and $y = 1$, where patterns and intensities can vary drastically on small scale. It is possible that these scales are not resolved in our measurements. The (1,2)-standing wave has a structure like his mode-1 solution, the parallelogram shaped attractor that of the mode-2 solution in that study, including the vertical motion at $y = 1/2$. The critical slope attractor is not really comparable to its mode-3 solution since it is of more propagating nature. Overall, the increase of complexity of the horizontal structures with decreasing frequency is seen both in the theoretical results

of Maas (2003) and in the observations. For decreasing frequency, rays are steeper in the vertical, resulting in smaller horizontal structures. However, the solutions presented in Maas (2003) cannot correctly describe the solutions of the tank with a sloping wall, since focusing and wave refraction are impossible in the rectangular tank, and play an important role in the observations. Therefore the similarity is the more striking.

We calculated the frequencies of rays that close onto themselves in a rectangular and square rectangular tank. These frequencies appear to be close to the true frequencies that belong to the modes in the rectangular and square basin. The approximations are good for the lowest modes, but for smaller scale structures (higher modes, especially in the rectangle) deviations of more than 10 % appear. We speculate that this is the effect of boundary layers, that are not accounted for in ray theory, and will play a more important role for more complicated structures and smaller basins. However, for the basin with the sloping wall, only individual wave rays will close onto themselves, for example rays that connect the corners.

It requires further research to determine the role of these rays in determining the horizontal structure of the wave field in a basin with a sloping wall. In that respect it is important to keep in mind that waves can exhibit propagating behaviour in the vertical direction and standing wave behaviour in the horizontal direction for the same frequency.

4.5.3 Limitation of energy concentration

It is interesting to directly compare the present observations with previous observations in larger basins by Maas (2001) ($54\times40\times120$cm), and chapter 3 ($107\times80\times500$cm). This enables us to directly compare the different measurements with respect to the relative thickness of the attractor. Beause of the different scales of the experiments, such a comparison reveals which processes balance the infinite concentration of energy predicted by linear theory. In figure 4.12 the values of U are plotted, divided by the maximum value U_{max} on the attractor. The different basins were plotted at the same size to enable observation of the relative width. Values smaller than 1/e are black. The relative width of the attractor appears to be comparable.

There are two processes that may determine the thickness of the attractor: viscous processes and nonlinear processes. Rieutord *et al.* (2001), (2002) investigated the width of the attractor assuming viscous processes to be the limiting factor, and found that it depended on a power of the Ekman number $E = 2\nu/(fH_0^2)$ with ν the molecular viscosity, according to $E^{1/3}$ (thinnest layer, Rieutord *et al.*, 2001) or $E^{1/4}$ (strictly two-dimensional approach, Rieutord *et al.*, 2002). The three different series of experiments have different Ekman numbers, as indicated in the figure and table 4.2. But taking into account the length scales of the basin, the attractor width is not proportional to a power of E.

Therefore we argue that nonlinear processes determine the width of the attractor in the experiments of figure 4.2, rather than viscous processes. To test this idea, the strength of the nonlinear and viscous term were estimated. As a length scale we take the distance b over which the motion increases from $U/U_{max} = 1/\mathrm{e}$ to 1. U_{max} is used as a velocity scale and the forcing period T as a time scale. The nonlinear terms are of order U^2/b, the viscous terms of order $\nu U/b^2$ (with $\nu = 10^{-6}$ m^2/s) and the inertial terms of order $2U/T$. Table 4.2 indicates that the nonlinear terms are in close agreement with the inertial terms, which means that the width of the attractor is determined by a balance between these two. The viscous

Experiment	H_0 (cm)	E	U (cm/s)	b (cm)	$\frac{U^2}{b}$ (m/s^2)	$\frac{\nu U}{b^2}$ (m/s^2)	2U/T (m/s^2)
Maas (2001)	40	$4.6 \cdot 10^{-5}$	0.3	4.5	$2 \cdot 10^{-4}$	$1 \cdot 10^{-6}$	$2 \cdot 10^{-4}$
chapter 3	80	$1.2 \cdot 10^{-5}$	0.4	8	$2 \cdot 10^{-4}$	$0.7 \cdot 10^{-6}$	$3 \cdot 10^{-4}$
present	19.5	$3.8 \cdot 10^{-5}$	0.2	1.5	$3 \cdot 10^{-4}$	$9 \cdot 10^{-6}$	$5.2 \cdot 10^{-4}$

Table 4.2: Estimated scales of processes.

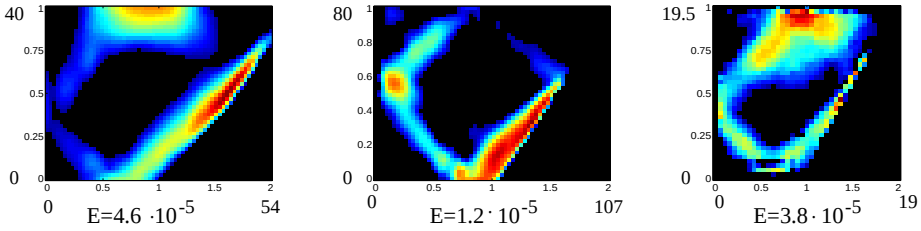

Figure 4.12: Scaled maximum velocity for experiments in different sized basins. The left pictures are for basic rotation rates of 0.13 rad/s, at y-positions of 1/5 and 1/4 of the basin's length (Maas (2001) and chapter 3, respectively). The rightmost fi gure displays the present observations at $y = 3/4$. Black parts indicate that the velocity is lower than 1/e. Large numbers indicate the actual sizes in cm.

term is much smaller. All of the square attractor shapes of chapter 3 have been investigated. Although at y-positions more close to $y = 0$ the balance was slightly worse, the difference was not more than a factor two. Another argument in favour of nonlinear processes is that in Maas (2001) a net (Lagrangian) flow is observed, apparently resulting from mixing. Future models should therefore include nonlinear terms close to the mathematical attractor.

4.6 Conclusions

Attractors and a standing wave in the vertical were observed in the laboratory at frequencies as predicted by theory for waves that do not propagate in the along-channel direction. Investigation of wave rays that do propagate in this direction revealed that wave focusing is accompanied by convergence in the along-channel direction. An attractor then appears as a surface to which wave rays converge, whereas for the standing waves wave rays do not close onto themselves anymore. In the three-dimensional basin, there appears no such strong link between closed wave rays and standing waves. In the laboratory observations, the horizontal structure of energy distribution and phase patterns of the wave fields indicated modal behaviour, with standing modes for the standing wave and the parallelogram shaped attractor and travelling modes for the critical slope. More research is needed to describe the observed wave fields mathematically. The energy concentration on the attractor appeared to be limited by nonlinear advection rather than viscous processes.

This chapter is submitted to *Fluid Dynamics Research* under the title “On the three-dimensional structure of the inertial wave field in a rectangular basin with one sloping boundary”, by A.M.M. Manders and L.R.M. Maas.

The authors thank G.J.F. van Heijst for the opportunity to use the laboratory facilities of the Fluid Dynamics Laboratory at the Eindhoven University of Technology. We gratefully acknowledge the technical support and enthusiasm of G.A.J. van der Plas during the experiments and the data processing. We appreciate the help of M.H. Rienstra and F. Eijgenraam in carrying out the experiments.

Chapter 5

Observations of internal tides in the Mozambique Channel

5.1 Introduction

Internal tides can be found nearly everywhere in the ocean. They are generated by barotropic tides over topography. It is thought that this conversion of barotropic to baroclinic tides (internal tides) is a major sink for the barotropic tidal energy (Sjöberg & Stigebrandt, 1992). The obliquely propagating internal waves are in turn subject to reflections and scattering. As we have seen in the previous chapters, reflection may lead to local concentration of energy, until the linear approximation breaks down and energy is transferred to even smaller scales. Thus they must form an important link in the process of energy transfer from large scale tidal motions to smaller scales.

Ultimately, the cascade to smaller scales makes the energy available for mixing. Where and by which mechanism mixing occurs in the ocean is a topic of active research (Munk & Wunsch, 1998). Observed diffusivity values in the open ocean are too low to account for the mixing rates that are necessary to maintain the global circulation. This implies that local mixing rates must be even higher than the required global average. Indeed, estimates have been made of the amount of dissipation of tidal energy. Satellite sea surface height measurements provide an accurate global tidal field, that can be used to feed numerical models that calculate the corresponding barotropic currents. These in turn can be used to study the effects of interaction with topography (Egbert & Ray, 2001), like friction and generation of internal tides. Where internal tides reflect at the bottom and especially where internal waves are parallel to the slope, mixing rates should be high. Thus, areas with strong topography are considered as sites of strong mixing. Submarine canyons play a special role, as they may act as a trap for internal waves (Petruncio *et al.*, 1998).

But the coverage of the ocean by in situ measurements is poor and observations are not equally spread. Observations are mainly in the generation areas, where the direct beams can be observed to large depth (Pingree & New, 1991), or completely confined to the shelf area. Recent examples include the upper 100 m above West Florida Continental Shelf (Leaman,

1980), the upper 1200 m across the Australian Shelf (Holloway *et al.*, 2001), the upper 500 m across the Californian shelf (Lerczak *et al.*, 2003), and the upper 700 m above the shelf in the Bay of Biscay (Lam *et al.*, 2003). In the open ocean, internal waves are observed hundreds of kilometres away from their generation area, as found from satellite altimetry (Ray & Mitchum, 1997) and direct observations (Morozov, 1995). They obviously survive a considerable number of reflections, although their beam-like nature is found to disappear, justifying the use of only the low modes in the open ocean.

Little is known about the structure of the internal wave field in enclosed basins. The existence of internal seiches in a lake was investigated by (Fricker & Nepf, 2000). Attention has been paid to the Faeroe-Shetland channel (van Veldhoven, 2000; Gerkema, 2002), but observations of the internal wave field with sufficient spatial resolution are still lacking.

In this chapter, the distribution of internal wave energy in the Mozambique Channel is studied. This narrow sea strait between Mozambique and Madagascar has a steep topography on the scale of internal waves and a reasonably strong surface tide, with elevations of about 1 m for lunar (M_2) and solar (S_2) semidiurnal tides (LeProvost, 2001), which makes the area favourable for the generation of internal tides. The observations consist of a year and a half-long moored current meter records and five 13-hour yo-yo measurements in the narrowest region of the Mozambique Channel. The mooring array was not specifically designed for the observations of internal tides, as it was primarily used to study the large scale currents in the channel (Agulhas Current Sources EXperiment, further referred to as ACSEX, see Ridderinkhof & de Ruijter, 2003). The horizontal separation of the current meters is larger than the wavelength, so too large to directly relate their records. Therefore a ray-tracing model and a numerical internal-tide generation model, in which the observed stratification and topography were incorporated, are used to support interpretation of the observations.

The structure of this chapter will be as follows. First, the most important currents and the stratification of the channel will be described briefly. A simple ray-tracing program is used to calculate the paths followed by the wave rays. A more sophisticated internal-tide generation model is used to predict the distribution of wave energy and the relative phase field for the cross section of the channel. Next the results from the yo-yo stations are shown and compared with the numerical tide generation model. Then the mooring section will be presented and the treatment of the data will be discussed. The barotropic and baroclinic currents are separated using harmonic analysis. After that, we will restrict ourselves to semidiurnal internal tide signals. The long records exhibited strong variability (intermittency). Amplitude and phase changes in the vertical of two moorings were monitored to describe the variation and vertical structure of the internal waves. To classify the full time records, differences and main features of the spectra are pointed out and the average energy in spectral bands is calculated. The results are compared with results from the numerical internal-tide generation models for interpretation.

5.2 Description of the Mozambique channel

The Mozambique Channel is a deep sea strait in between the African continent and Madagascar. It is only 370 km wide on its narrowest part, with a depth of up to 2700 m next to the Davie Ridge, over which the depth decreases rapidly to 2000 m. The bathymetry and

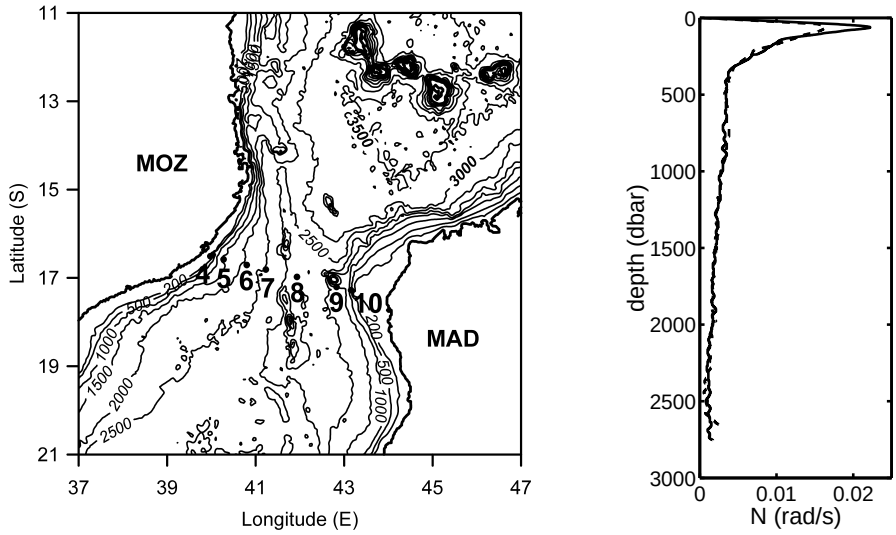

Figure 5.1: *(a)* Map of the research area. The mooring positions are indicated by the black dots. The islands around 12° S are the Comores. *(b)* Representative Brunt-Väisälä frequency for 2000 (dashed) and 2001 (solid), as determined from the ensemble of CTD-stations.

mooring locations are shown in figure 5.1(a). Little has been published about the flow in the Mozambique Channel. Schuman (1998) and DiMarco *et al.* (2002) did not find a persistent flow: the flow in the channel is variable, possibly due to the presence of eddies. Their observations were a collection of snapshots of the local flow field. Especially from the central part of the Mozambique Channel hardly any observation was available.

In the ACSEX-program, two cruises were undertaken with the Dutch Research Vessel Pelagia to study the flow in the channel, in March-April 2000 and 2001. An array of current meter moorings has been operating for more than a year and a half in the narrowest part of the channel. The data were completed with vessel mounted ADCP (Acoustic Doppler Current Profiler) and drifter data and several CTD (Conductivity-Temperature-Depth) sections. The present study is based on measurements that were done as part of the ACSEX-project. In addition to the current meter mooring and CTD-observations, yo-yo measurements were carried out to detect internal waves.

The large scale flow in the channel, based on these observations, is described in Ridderinkhof & de Ruijter (2003) and is briefly summarized here. It appears to be dominated by the southward passage of large anticyclonic eddies, with cross sections of about 350 km, which fill the Mozambique Channel at its narrowest part. They are formed in or slightly to the north of the region of the moorings and appear rather regularly, 4 to 5 per year. The eddies extend over the full water column with weakly depth-varying currents of more than 40 cm/s in the upper hundreds of metres. Near the African slope, at depths between 1500 and 2500 m, the Mozambique Undercurrent was observed, flowing northwards with a speed of about 4.5 cm/s.

The strength of the stratification is best represented by the Brunt-Väisälä-frequency N. It is defined according to

$$N^2(z) = -\frac{g}{\rho_0}\frac{d\rho_0}{dz} + \frac{\rho_0 g}{c_s^2}$$

where g represents gravity, directed against the vertical z, ρ_0 the density and c_s is the local sound speed in the water, as determined by pressure, temperature and salinity, accounting for compressibility effects. Based on CTD-sections of the two cruises, profiles of N were computed using running means over 16 decibar (dbar) in the vertical to avoid spikes in the derivatives.

Figure 5.2 shows the stratifications in the channel during the two cruises. The first cruise was during the passage of an eddy whereas there was no eddy present during the second cruise. During the passage of an eddy, the water in the middle of the basin is warmer and more saline, resulting in a depression of the isopycnals. Maybe even more important is the difference in the structure in the upper 300 m of the water column (see the enlargement in figure 5.2), with a much stronger stratification when the eddy is absent. In the absence of an eddy the pycnocline is much sharper and has an arch-like structure, especially in the western part of the channel, whereas in the presence of an eddy the structure of the pycnocline is more ore less hollow and less pronounced. The change in stratification due to eddies probably dominates seasonal changes. At this latitude the seasonal variation in temperature, the most important factor in the formation of a seasonal pycnocline, is far less than at higher latitudes. In the lower part of the water column the values of N are nearly equal for the two cruises.

5.3 Internal wave models

The angle θ of the internal wave rays with the direction of gravity depends on the frequency of the wave ω, on $N(z)$ and on the local Coriolis parameter $f = 2\Omega \sin\phi$ with Ω the rotation frequency of the Earth and ϕ the geographical latitude. For a stratification that varies slowly with respect to the wave length of the internal waves, this angle is locally given by

$$\tan^2\theta = \frac{N^2 - \omega^2}{\omega^2 - f^2} \tag{1}$$

The phase lines are parallel to the wave rays, the phase propagates in a direction perpendicular to the direction of energy propagation. They propagate in the same horizontal, but in the opposite vertical direction. The large scale eddies affected the stratification and therefore must affect the theoretical paths of the internal wave beams.

Two numerical models were used to study the internal wave field theoretically. These models use the observed topography and stratification. A horizontally uniform stratification has been used. This stratification is the average value for the part below the pycnocline, but for the upper part an artificial pycnocline peak is constructed, that has a peak value that is around the average peak value, at a depth that is around the average pycnocline depth. A pure horizontal average of the profiles of the different CTD-stations would have smoothed out the pycnocline and taking the profile of the deepest station as representative was not justified. Due to horizontal variations in the stratification, the predicted wave patterns will not be exact,

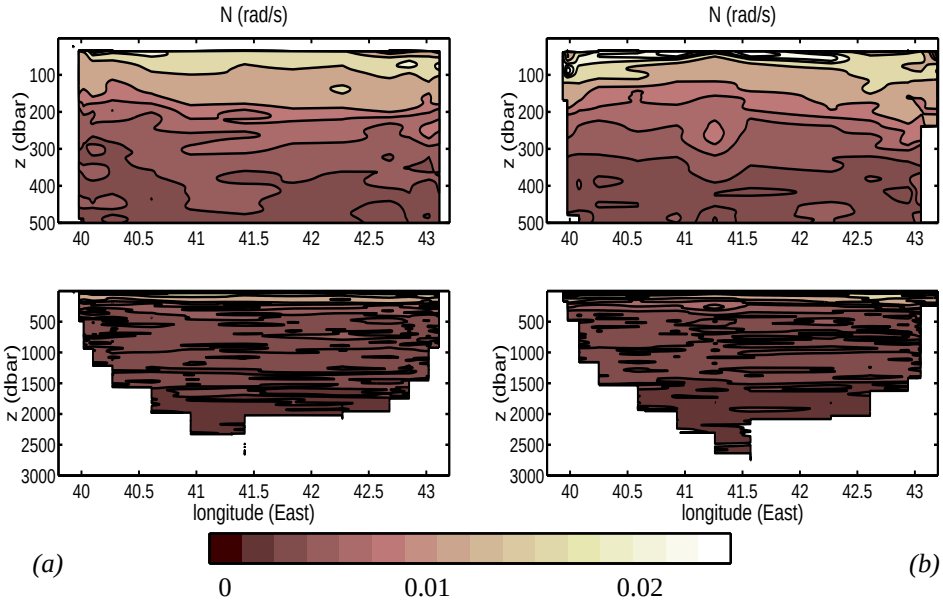

Figure 5.2: Brunt-Väisälä-frequency N (rad/s) for the CTD-profiles. The positions of the profiles can be determined from the block-shape channel depth representation. *(a)* 2000, in the presence of an eddy and *(b)* 2001 in absence of an eddy. The upper panel is an enlargement of the upper 500 m of the lower panel to illustrate the pycnocline structure.

but large scale features, like the number of reflections needed to cross the channel, will be represented correctly. The profiles are plotted in figure 5.1.

The first model is a simple two-dimensional ray-tracing model that indicates paths of wave rays. It only takes changes in direction due to changes in stratification and reflection at the bottom and surface into account. The steep, small-scale structures in the topography sometimes led to trapping or back-reflection of the wave. In reality, the waves will form beams of certain width and the fate of isolated rays is unimportant. Figure 5.3 shows the ray paths for M_2 for the two different stratification regimes. Only the rays starting from the Madagascar side are plotted for transparency. Wave rays cross the basin within 6 to 7 reflections. The two different stratifications lead to different ray paths, but major features are the same.

The ray-tracing model is a decent description under the restriction that the stratification does not change considerably on the scale of the wave length. In the pycnocline region this is not the case. Therefore, a more sophisticated model was used, that does not have this drawback and accounts for both the change in direction and internal reflections at the pycnocline, resulting in scattering of the waves. This internal-tide generation model (Gerkema, 2001) is a two-dimensional model, assuming along-slope uniformity. It again uses the observed topography and stratification $N(z)$ of the basin. The barotropic tide is converted into internal tides, using the cross-slope tidal flux. The tidal flux must be prescribed, but as the model is linear, its value only affects the absolute strength of the currents, not the relative. Ultimately the

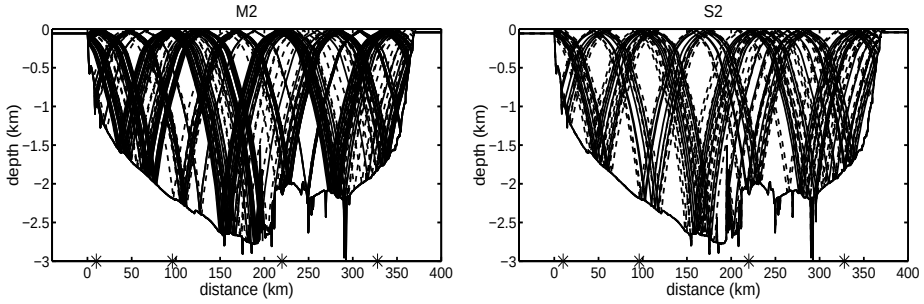

Figure 5.3: Ray paths starting on the Madagascar shelf (on the right), five upwards and five downwards, for the stratification with (dashed) and without eddy (solid). Left panel is for M_2, right panel for S_2. Stars indicate the yo-yo stations, that are discussed in the next section.

results were scaled as to roughly match the observed velocity amplitudes. The topography of the channel is transformed into a rectangular basin. In the vertical Chebishev-polynomials are used in a pseudo-spectral method. In the horizontal and for time integration a finite difference scheme has been used. A model run spanned 100 tidal periods, which appeared enough to overcome the transient response and find the equilibrium internal wave field. Although the amplitude was not completely constant, its variations were small and results did not change significantly. The results from this model will be shown together with the field observations.

5.4 Yo-yo results

During the 2001-cruise four 13 hour yo-yo measurements were carried out with a CTD-profiler over the full depth of the water column, close to the current meter mooring positions. Only the downcast measurements were used, as upcast measurements are less accurate due to the dragging of water by the CTD-frame. Since a single down and upcast takes nearly an hour at water depths of about 2000 m, the deep stations do not have a good time resolution (8-10 casts in 13 hours). This is still enough to capture semidiurnal waves but waves with higher frequencies cannot be resolved. Discrimination between the slightly different tidal components M_2 (lunar semidiurnal tide, period 12.42 hours) and S_2 (solar semidiurnal tide, period 12.00 hours), and components with smaller contributions to the spectrum, is not possible. There was one yo-yo station during the 2000-cruise, but since it is isolated in time its results were not used.

The excursions of the isotherms in time were analysed using harmonic analysis. Their amplitude A and phase ψ with respect to yearday 0 (January 1st 2000, 0 h00 UTC) were determined for the M_2 tidal frequency ω by calculating the fit to $z = A\cos(\omega t - \psi)$. In this convention, phase propagation is in the direction of increasing phase. The peak to trough amplitude is $2A$. Phase and energy propagation are opposite in the vertical direction. Thus locations of upward and downward propagating energy can be determined. The horizontal direction cannot be determined from observations in the vertical alone. When the same procedure was applied to the isopycnals nearly identical results were found.

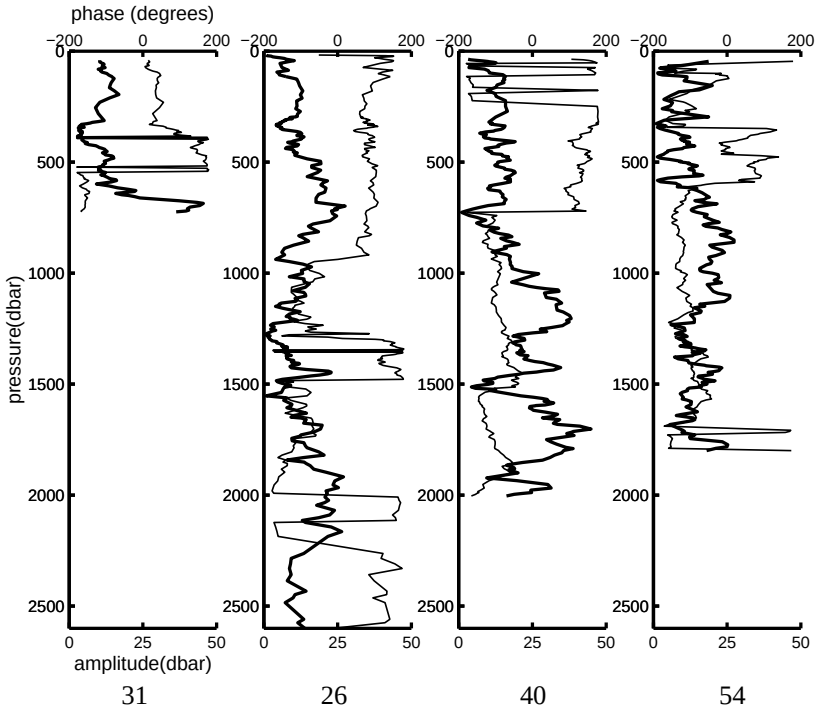

Figure 5.4: Amplitude (thick line) and phase (thin line) of harmonic analysis (M_2) of the isotherm displacement. The subplots are ordered such that they form a west-east cross section of the channel, their position is indicated in fi gure 5.5

In figure 5.4 the results are plotted. The fit of the isotherms to the M_2-frequency is in general successful, around 80 % of the isotherm displacement in time is explained. Only at some depths this is not the case. Locations where this occurs can be identified from the low amplitudes in small depth intervals and this is often accompanied by a rapid phase change. At these locations internal motion is often present, but with larger (diurnal?) or shorter periods that cannot be resolved well. The phase jumps from about 180 to about -180 degrees must be interpreted as continuous phase changes, as the phase is defined on a cyclic scale.

In station 31 (16° 30.49' S, 40° 0.71' E, depth 648 m) a large internal wave is detected near the bottom, with an amplitude of more than 40 dbar, implying an excursion of the isotherms of more than 80 m. This wave has a small extent in the vertical. The downward phase propagation implies upward travelling wave energy.

Station 26 (16° 49.26' S, 41° 16.20' E, depth 2654 m) shows more modest internal wave activity with amplitudes of 20 dbar at a 'depth' of 700 dbar and around 2000 dbar. There is no clear phase propagation around 700 dbar, but phase changes abruptly at 1000 dbar. From 1300 to 1600 dbar the phase is increasing continuously, which points at upward energy propagation. Further downwards it decreases with a minimum around 2000 dbar and a sudden rise at 2200 dbar.

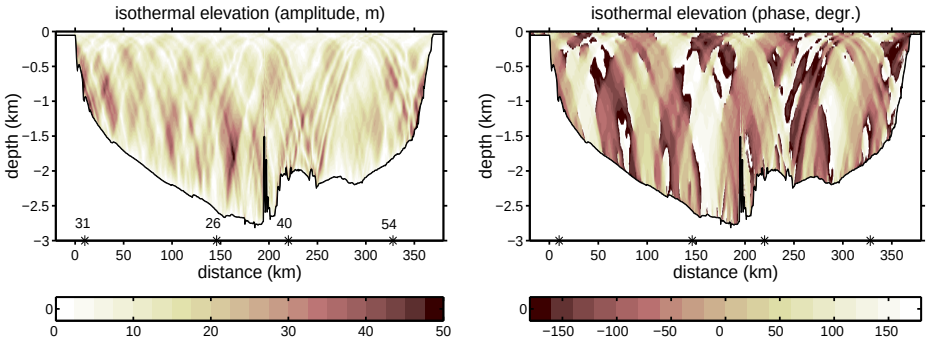

Figure 5.5: Amplitude and phase of isotherm displacement from the numerical internal-tide generation model. The absolute amplitude is arbitrary, depending on the barotropic flux.

Station 40 (16° 58.77' S 41° 56.09' E, depth 2008 m) has two large regions of strong wave activity with amplitudes around 40 dbar: around a depth of 1200 and 1700 dbar. They are separated by a region of low amplitude and a phase shift. In the regions of strong wave activity the phase is increasing slowly with depth, so the wave energy must be travelling upwards.

Station 54 (17° 12.34' S 42° 49.67' E, depth 1808 m) has modest internal wave activity, with a broad region around 900 dbar and two small regions around 1500 and 1800 dbar where the amplitude of the waves is around 20 dbar. There is a clear phase shift at 600 dbar. There is no evident phase propagation in the internal wave regions, so that no firm conclusions can be drawn about the direction of energy propagation.

The yo-yo stations are too far apart to follow a beam of internal waves in the horizontal. Reflection alters the phase, which hampers direct comparison between the stations. Furthermore, there is a week time difference between the first and the last yo-yo station, which may cause relative differences in amplitude due to the spring-neap cycle. Station 40 was during spring-tide, and indeed has internal waves with largest amplitude. The other stations are three to two days earlier (yearday 461, station 26, yearday 462, station 31) or three days later (yearday 467, station 54). Direct beams from the shelf were not identified.

The amplitude and phase of the isotherm displacement were calculated by the numerical tide generating model for the stratification observed in the 2001-cruise. It reproduces the large isotherm displacement at station 31, but not the large displacements at station 40. Overall, model isotherm displacements are larger at the Mozambique side of the channel, where they appear in large patches at mid-depth. The observed location of maximum isotherm displacement is represented fairly well. As for the phase, only relative phases can be compared. The locations of large phase transitions are more or less in accordance with the observations for station 26 (the large phase change around 1000 m depth) and 40. But for station 54 the phase change in the lower part of the water column is not observed, and for station 31 the direction of phase propagation is the other way round.

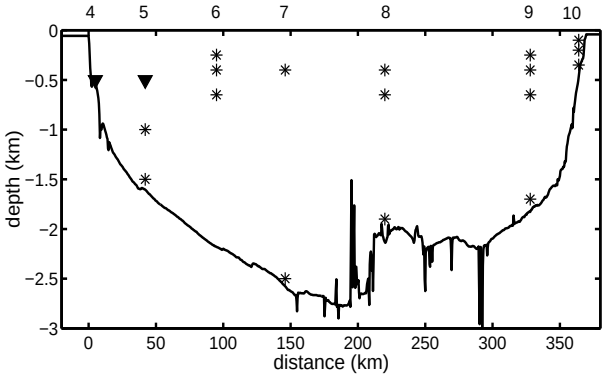

Figure 5.6: Distribution of current meters (stars) and upward looking ADCP's (triangles) over the Mozambique Channel. Numbers refer to mooring identifi cation numbers.

5.5 Current meter results

Current meters that measure horizontal velocities were deployed in March-April 2000. After the first year of deployment, the moorings were surfaced, serviced and redeployed. In November 2001, the moorings were finally recovered with the British RV Charles Darwin. The exact locations and operation times of the instruments are displayed in table 5.1. Figure 5.1 indicates the geographical positions of the moorings. Figure 5.6 shows their vertical distribution over the channel. The ADCP's at the Mozambique-side cover the upper 500 m.

The current meters were connected to the bottom with long mooring cables. When the low-frequency current speed exceeded 25 cm/s (at $\pm$ 200 m below the surface), which occurred during eddy passages, the moorings were inclined considerably. The vertical position of the upper current meters could be be up to 200 m lower than their upright position, as is observed from pressure sensors on the current meters. In case of these strong flows, the mooring also oscillated strongly, according to the strong pressure fluctuations. The frequency of these fluctuations was the semidiurnal tidal frequency. Also high-frequency oscillations of small amplitude may have been present, that are above the Nyquist frequency. The strong motion caused heavy damage to the rotors or interior of some of the current meters. During the second deployment period, for two moorings, the bottom weight was not heavy enough for the strong currents. Mooring ACS08 drifted some kilometers away from its original position. Mooring ACS06 even drifted more than 10 km to the southwest and was not detected during the recovery with the British RV Charles Darwin, but was found later after the mooring cable had broken and was then picked up. Because both the time resolution and the spatial coverage of the surviving current meters were better in the second deployment period, we will mainly consider these results.

Some current meters were provided with temperature sensors. In theory, temperature fluctuations can be directly related to the internal tide since the barotropic tide hardly causes excursions of the isotherms. But because of the mooring motion, temperature fluctuations may also be caused by the change in vertical position of the current meter. Separation of the two effects is cumbersome, if possible at all, therefore the temperature results are not used.

mooring position		water depth	mooring ID	design depth	instrument type	sampling rate	deployment period
lat (S)	lon (E)	(m)		(m)		hr^{-1}	(yearday)
16° 30.62'	39° 58.52'	536	ACS04-A	500	ADCP-LR	1	98-463
16° 24.73'	40° 16.63'	1595	ACS05-A	500	ADCP-LR	1	98-459
			ACS05-2	1498	RCM8	3	98-459
16° 41.92'	40° 48.41'	2199	ACS06-1	250	RCM8	3	98-460
			ACS06-2	400	RCM8	3	98-124
16° 48.74'	40° 48.41'	2603	ACS07-1	250	RCM8	3	99-464
			ACS07-2	400	RCM8	3	99-197
16° 58.63'	41° 56.02'	1998	ACS08-1	250	RCM8	3	99-457
			ACS08-2	400	RCM8	3	99-457
			ACS08-3	650	RCM8	3	99-457
			ACS08-4	1902	RCM9	3	99-457
17° 12.13'	42° 50.24'	1815	ACS09-1	350	RCM8	3	99-457
			ACS09-3	650	RCM8	3	99-457
17° 17.30'	43° 09.55'	445	ACS10-1	100	RCM8	3	99-305
			ACS10-2	200	RCM8	3	99-457
			ACS10-3	349	RCM8	3	99-457
16° 30.62'	39° 58.52'	526	ACS04-A	500	ADCP-LR	2	464-680
16° 24.73'	40° 16.63'	1595	ACS05-1	1000	RCM11	6	464-679
			ACS05-2	1498	RCM11	6	464-679
16° 41.92'	40° 48.41'	2199	ACS06-1	250	RCM9	6	467-750
			ACS06-2	400	RCM8	6	467-750
			ACS06-3	650	RCM8	6	467-750
16° 48.74'	41° 13.88'	2603	ACS07-2	400	RCM8	6	466-527
			ACS07-4	2507	RCM11	6	466-679
16° 58.63'	41° 56.02'	1998	ACS08-2	400	RCM8	6	466-680
			ACS08-3	650	RCM8	6	466-680
			ACS08-4	1901	RCM11	6	466-680
17° 12.13'	42° 50.24'	1815	ACS09-1	250	RCM8	6	468-677
			ACS09-2	400	RCM8	6	468-677
			ACS09-3	650	RCM8	6	468-677
			ACS09-4	1719	RCM11	6	468-677
17° 17.30'	43° 09.55'	445	ACS10-1	100	RCM9	6	468-615
			ACS10-2	200	RCM11	6	468-677
			ACS10-3	349	RCM8	6	468-677

Table 5.1: Position and sampling rates of the current meters that worked properly for more than 20 days. The second period is indicated separately, as different current meters were used and instrument losses occurred at different locations.

The horizontal velocity measurements were decomposed in two components: the u-component is directed along the mooring array, the v-component is perpendicular to it and in the direction of the channel. Thus the common geographical coordinate system is rotated clockwise over 14 degrees. The resulting u-components can then be compared directly with

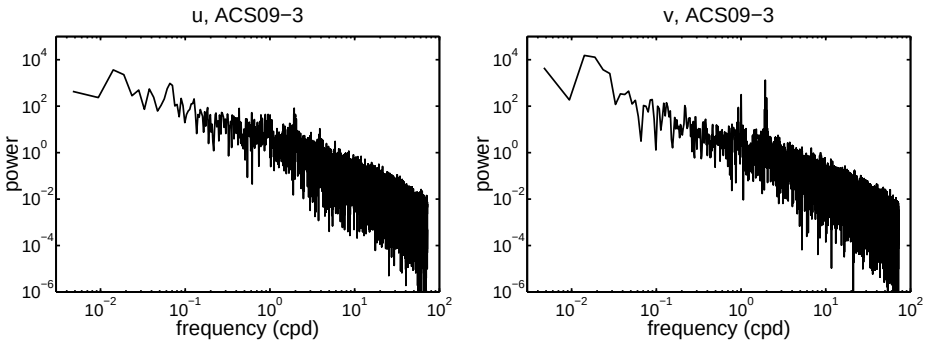

Figure 5.7: Raw power spectra (cm^2 s^{-2} /cpd) of ACS09-3, u in left panel, v in right panel.

the (two-dimensional) numerical models.

Spectra of the raw signal are shown in figure 5.7 for current meter ACS09-3, which serves as an example that exhibits features typical for this channel. The most energetic part is the low-frequency part, which must be associated with the eddies. The peaks of the tidal frequencies are much higher and sharper for the v-component than for the u-component.

5.5.1 Barotropic currents

To study internal tides, the barotropic tides have to be subtracted from the velocity records. We chose to estimate the barotropic currents from the data for every mooring separately. The time series were high pass filtered with a cut-off frequency of 1/4 cycle per day (cpd), to eliminate the energetic long-term flow (eddies). The filtered signals were averaged per mooring (vertical averaging). The upper current meters are more closely together and at first weight factors have been used to compensate for this. However, as this hardly altered the results, direct averaging was used.

Harmonic analysis was applied to the averaged velocity records to find amplitude and phase of the coherent tidal currents, according to

$$u = \sum_n U_n \cos(\omega_n t - \psi_n). \tag{2}$$

The tidal components that were taken into account are the diurnal components O_1 (soli-lunar declinational tide, period 23.93 hours) and K_1 (main lunar tide, period 25.82 hours) and the semidiurnal constituents N_2 (longer lunar elliptic, period 12.66 hours), M_2 and S_2, as these five generally are strongest. Like for the yo-yo stations, the phase $\psi = 0$ refers to January 1st 2000 0 h00 UTC. It is assumed that the results represent the barotropic tide. The baroclinic tide should in theory be averaged out by averaging over the water column. Because of the poor vertical resolution, this might not be the case. However, internal tides are often intermittent (which is the case as will be illustrated), and they probably do not contribute significantly to the deterministic tidal part of the signal when long-term observations are analysed. The amplitudes and phases are displayed in table 5.2, for both periods (if available).

The time series of the high-passed, vertically averaged u-velocities were not well represented by the harmonic fit; the percentage of the signal that is accounted for by the analysis ranged from 30% to at most 50% for ACS08 and the ADCP near the shelf. For the individual current meters the fit was worse, 10% to 30%. The results were not consistent over the two periods of observation. The spectrum in figure 5.7 already indicated that the contribution of the tidal frequencies to the spectrum was small. Only in the ADCP's the vertically averaged tidal currents in u were significant. There the vertical averaging is more accurate, as nearly the whole water column is resolved.

The harmonic analysis of the v-component was more successful: 50% to even 80% of the signal was accounted for. The individual current meter signals close to the bottom were in general better represented by the harmonic analysis than those near the surface. Again averages gave better fits than individual records, but the differences are not as dramatic as for the u-component, pointing at the vertical persistence and dominant character of the v-component of the tidal currents.

The barotropic tidal flow due to the M_2, S_2 and K_1-tide dominated the current meter signal for the v-component. Amplitudes were not constant over the basin, tidal currents were weaker in the deeper parts of the basin and stronger near the shelf. Phases were nearly uniform for these components. Regarding the strong topography, that locally affects the currents, and the coarseness of the vertical resolution (especially at ACS06 and ACS07), which inhibited averaging out the internal tide in the vertical, the results seem consistent. The surface tide was determined from the pressure sensor on ACS04 and its decomposition is also included in table 5.2.

Hereafter the symbol $\tilde{v}$ will be used for the v-component from which the barotropic tide has been subtracted. Then u and $\tilde{v}$ are of the same order of magnitude in the semidiurnal tidal band. Because of the poor fit and low amplitudes, the fits were not subtracted from the u-component, except for the ADCP's.

5.5.2 Internal tides

Intermittency

To give an impression of the internal semidiurnal signal, band pass filtered (1.7-2.4 cpd) signals of u are presented in figure 5.8. Only the last mooring period is shown. The figure illustrates that the amplitudes were irregular. Near the shelf, motion was considerably stronger, which can be interpreted as the effect of the generation area where strong internal tides are expected. Events of high velocities of one current meter could not be related to events of high velocities in other current meter records. Since internal wave ray paths are different for the different tidal frequencies, at each current meter the internal waves will have different strength and phase, and will add up to different patterns (Gerkema, 2002).

But also for individual current meters velocity amplitudes were highly irregular (intermittent); the change in amplitude could not be attributed to a regular spring-neap cycle. This is typical for internal tides. In figure 5.9, u and $\tilde{v}$ are plotted. Differences in phase and amplitude between the current meters were clearly present, but only for short time. They come and go. Also the phases and amplitudes of u and $\tilde{v}$ varied with respect to each other for individual current meter records. Contrary to the mathematical definition of intermit-

mooring	O1	ψ	K_1	ψ	N_2	ψ	M_2	ψ	S_2	ψ	% fit
ACS04-I(u)	0.64	147	1.44	-108	0.49	166	2.32	64	1.05	-157	62
ACS04-I(v)	0.29	150	0.65	-112	0.33	167	1.34	72	0.58	-121	57
ACS04-II(u)	0.48	154	1.33	-101	0.33	144	1.47	91	0.88	-149	50
ACS04-II(v)	0.40	154	1.13	-101	0.39	-170	1.47	104	0.86	-123	52
ACS05-I(u)	0.30	-157	0.83	-79	0.56	-156	2.14	99	5.86	-74	43
ACS05-I(v)	0.51	162	1.20	-108	0.47	-87	1.52	108	0.63	-130	41
ACS05-II(u)	0.31	176	0.94	-95	0.40	150	0.81	90	0.43	-140	39
ACS05-II(v)	0.53	169	0.89	-80	0.79	-123	2.47	104	1.30	-86	73
ACS06-II(u)	0.27	169	0.24	-52	0.22	-158	1.29	105	0.63	-88	32
ACS06-II(v)	0.35	-168	0.81	-102	0.69	-124	2.29	128	0.90	-74	48
ACS07-II(u)	0.09	-63	0.46	-124	0.20	-78	0.72	88	0.29	-127	27
ACS07-II(v)	0.47	132	1.19	-93	0.26	178	2.41	99	1.37	-107	65
ACS08-I(u)	0.13	140	0.20	-140	0.09	95	0.37	113	0.21	-43	20
ACS08-I(v)	0.44	158	1.32	105	0.81	-134	2.25	98	0.91	-107	74
ACS08-II(u)	0.43	158	0.69	-84	0.40	-98	0.97	116	0.57	-109	50
ACS08-II(v)	0.58	175	1.17	-88	0.52	-142	2.25	108	1.21	-105	74
ACS09-I(u)	0.13	42	0.31	158	0.22	-58	0.42	-148	0.31	67	17
ACS09-I(v)	0.65	149	1.66	-117	0.74	-147	3.60	95	1.89	-110	75
ACS09-II(u)	0.31	7	0.48	175	0.25	-127	0.48	180	0.61	55	28
ACS09-II(v)	0.81	131	1.75	-113	0.66	-148	3.39	97	1.56	-116	85
ACS10-I(u)	0.40	-31	0.32	87	0.43	-15	0.52	144	0.44	-38	29
ACS10-I(v)	1.19	110	2.74	-127	1.29	-164	4.31	104	1.76	-120	77
ACS10-II(u)	0.52	-34	0.72	88	0.41	6	1.02	-174	0.71	17	32
ACS10-II(v)	0.89	117	2.81	-111	0.81	-96	3.62	98	2.07	-80	69
surface (m)	0.06	-148	0.05	-3	0.15	1	0.90	-105	0.49	67	98

Table 5.2: Harmonic analysis (amplitudes in cm/s, phases in degrees) of high pass filtered and vertically averaged current meter records, and harmonic analysis of depth sensor of ACS04 to give the surface tide (in m). Roman numerals indicate the period of observation: I is March/April 2000-2001, II is April-November 2001.

tency, where the presence of an intrinsic near-equilibrium causes near-periodic behaviour, it is here the constant perturbation in background conditions and forcing strength that causes the variability.

To quantify changes in amplitude and phase of current meter records, harmonic analysis was applied on windows of only four days of the band-pass filtered records shown in figure 5.8. For such narrow windows, the different semidiurnal constituents cannot be resolved. Therefore only M_2 was fitted, to represent the semidiurnal motion. The spring-neap cycle is then mimicked by a regular increase and decrease of the amplitudes and regular phase variations around a constant value. If the signal is dominated by M_2, the fit to the windows is good, up to 100% for some windows. If the signal is dominated by S_2, the phase may change dramatically and the fit is considerably less.

The results of harmonic analysis of the u-component of ACS09 and ACS10 are shown in figure 5.10 for four-day windows with steps of one day. The resulting amplitudes varied smoothly but irregularly. The signal, that was explained up to 30% by harmonic analysis

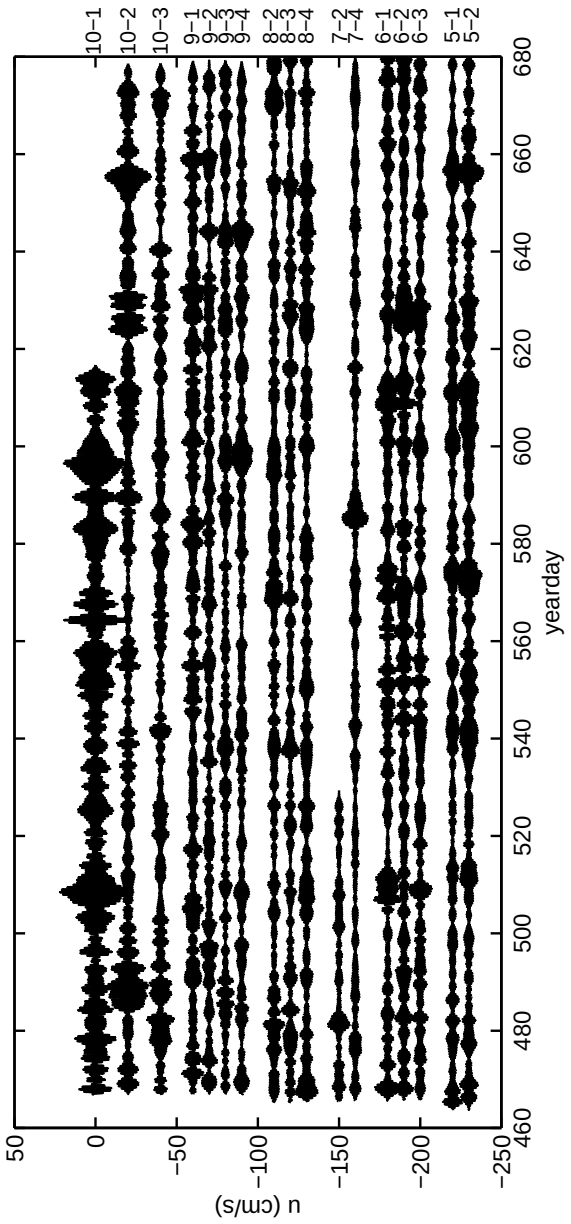

Figure 5.8: Observed band-pass (1.7-2.4 cpd) filtered u of current meters ACS05-ACS10. The vertical scaling is in cm/s, with offsets for the different records.

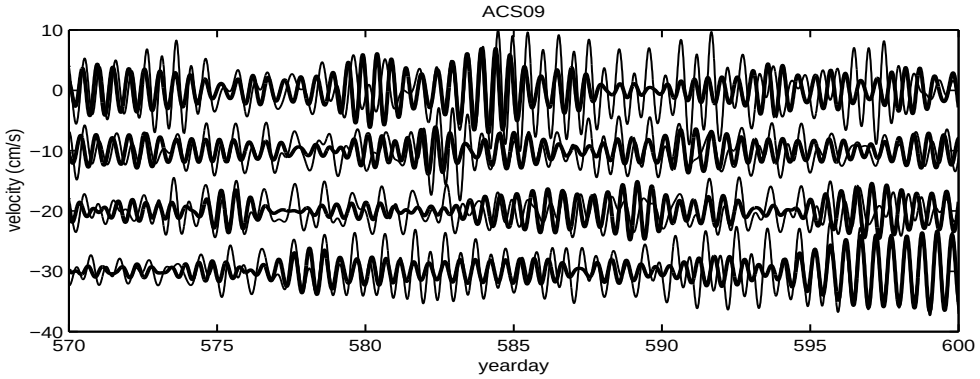

Figure 5.9: Enlargement of figure 5.8, that illustrates differences in the amplitude and phase in the vertical of the four ACS09 current meters for u (thick line) and $\tilde{v}$ (thin line). The phase differences between the different current meter records for yearday 595-600 are especially clear, but phase differences can be found nearly at all times.

is now explained for generally more than 50% up to almost 100%. Most of the spikes in the phase are due to the transition of 180 to -180 degrees and vice versa, which is in fact a continuous transition.

Phases and amplitudes were different for the different current meters, which illustrates that we are looking at internal tides. For ACS09, current meters 1 and 2 in general had the same phase, current meter 4 was generally 180 degrees out of phase, current meter 3 tended to follow the upper two current meters, but differed considerably from time to time. Amplitudes of current meters 1 and 4 were largest. The lower current meter had small phase changes, whereas the upper current meter exhibited slow but large phase changes over the full 360 degrees and back. For ACS10-1 the upper current meter had the largest amplitudes. The phases of the three current meters were different, but those of 2 and 3 appeared more closely related. Also patterns of phase changes were different. For ACS10-1, the phase was generally around 170 degrees, with phase jumps due to the 180 to -180 degrees transition.

No direct relation was observed between amplitude and phase changes of the current meter internal tidal signal and the presence or absence of eddies, despite the changes in stratification and the mooring motion.

Spectra and integrated signal

As the internal tidal currents are highly variable, a different method is sought to quantify the overall results. The spectra appear a good instrument to do this. When the tidal signal is incoherent, due to changes in ray path or current meter position, the energy may leak to the side bands of the tidal bands (van Haren, 2002). Therefore the full semidiurnal band was studied.

Three different power spectra of u and $\tilde{v}$ from different regions are shown in figure 5.11. The spectral levels in the generation area (ACS10-1) are clearly highest, also just outside the semidiurnal band. Peaks at the M_2 and S_2 frequency are visible, but do not stand out much.

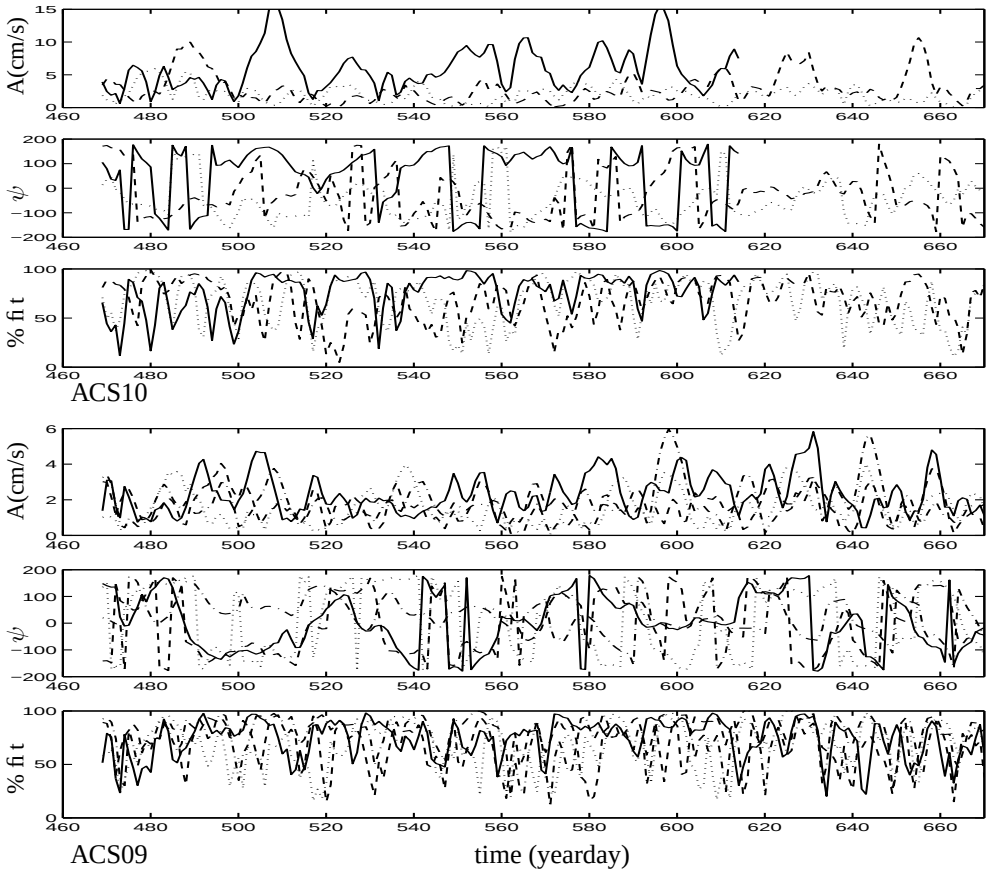

Figure 5.10: Fit of M_2 to band-pass filtered u-velocity in windows of 4 days with time steps of one day. From top to bottom: amplitude, phase and % fit of ACS10 (solid=upper, dashed=middle, dotted=lower current meter), amplitude, phase and %fit of ACS09 (solid=upper, dashed=second, dotted=third, dash-dotted=lower current meter).

In the spectrum of the near-bottom current meter ACS09-4 distinct tidal peaks are visible, which contain most of the energy. For this current meter, mooring motion can be neglected, variations must be attributed to changes in ray paths. Apparently amplitude and phase of the observed velocities did not change as much as in current meter ACS09-1, for which the tidal peaks have nearly vanished but for which overall levels are higher.

To enable the identification of regions where motion is strongest on average the spectra were integrated over the semidiurnal band. These results can then be compared with the numerical models. This is a coarse method, but it gives a summary of the different current meters results and eliminates the problem of the variability. The current meter records were high-pass filtered and the v-component was corrected for the barotropic tide. For the ADCP-records of ACS04-A and ACS05-A the spectra per bin were calculated and then averaged per

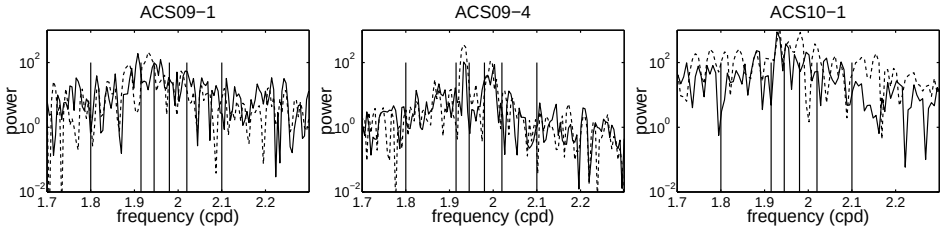

Figure 5.11: Power spectra (cm^2 s^{-2} /cpd) of u (solid) and $\tilde{v}$ (dashed) for three different current meters. ACS10-1 is in the generation area, ACS09-4 is at the bottom and ACS09-1 at the top of a mooring. The vertical bars around 1.92 and 2 indicate the windows of intergration for the computation of the energy content of the M_2 and S_2 band, the outer vertical bars give the boundaries of the window for the semidiurnal band D_2.

100 m. Mooring motion was not taken into account: for the ADCP's the vertical averaging already is a coarse approximation, for the current meters there is no way to correct for it. The full record length was used to get the best possible spectral resolution since also the integrals over small bands around M_2 and S_2 were computed. Using smaller windows and averaging did not alter the qualitative results for the total semidiurnal band, but the narrow bands were not resolved well. The contribution of the M_2 and S_2-integrals to the total energy in the semidiurnal band is an indication for the variability of the tidal signal: a high contribution means that the periodic signal was persistent and that little energy has leaked to the sidebands. The results are put in table 5.3.

The table indicates that motion was strongest for the upper current meters of ACS04, ACS05 and ACS10. One may argue that the upper current meters near the shelf are in the generation area, but values of ACS05 are still strong, and this mooring is 40 km off the shelf. Further, this motion decreased rapidly with increasing depth. For the rest of the current meters, motion was strongest at ACS05-2, ACS06-2, ACS07-2, ACS08-4 and ACS09-1 for u, and for $\tilde{v}$ at ACS05-2, ACS06-1, ACS07-2, ACS08-4 and ACS09-4. Differences between current meters remained however within a factor 4. The changes in location of maximum velocity of u and $\tilde{v}$ may be caused by the subtraction of the barotropic tide for the latter. Subtraction of the true, vertically uniform barotropic tide should give the same maxima for u and $\tilde{v}$, as differences in the vertical are due to the baroclinic tide. As the vertical resolution is poor, the signal of one current meter may dominate, such that for this current meter $\tilde{v}$ is lower and for the other current meters $\tilde{v}$ becomes larger.

We will compare our results with the results from the numerical internal-tide generation model. The internal tidal current amplitudes and phases of u were calculated for the stratification with and without eddy and are displayed in plate VI. The two stratification regimes yield large scale patterns that are comparable, in the sense that for both stratification regimes, motion is strongest above the pycnocline. For the stratification with eddy, motion is generally weaker, which must be an effect of the change of wave ray direction with respect to the topography, which alters the effectiveness of internal-tide generation and focusing or defocusing upon reflection. Phase patterns are scattered more for the stratification with eddy, especially at the Madagascar side. The difference in pycnocline strength for the both regimes could be

	u				$\tilde{v}$			
ACS	M2	S2	K1	D2	M2	S2	K1	D2
04-50	6.6477	2.9538	0.7466	24.2471	2.2320	2.1607	0.6958	12.1404
04-150	2.3548	0.7576	0.3865	8.7603	1.0209	0.4133	0.5084	4.2808
04-250	1.2377	0.5321	0.4226	5.2019	0.3550	0.2738	0.2836	2.0029
04-350	1.2747	0.7976	0.5203	4.4088	0.6819	0.4233	0.4982	2.1551
04-450	1.7514	0.8369	0.3737	5.7101	0.6064	0.5233	0.3535	2.6209
05-50	5.3651	1.8222	1.5516	22.6459	4.4627	3.5676	1.9054	21.4495
05-150	2.9434	1.0444	0.6075	9.8855	1.5613	1.3873	1.2832	7.9199
05-250	2.6944	0.6564	0.7258	6.3895	0.9373	0.8655	0.7687	4.8273
05-350	2.3212	0.5621	0.8512	5.1309	0.4910	0.6356	0.6571	3.3653
05-450	1.9299	0.5175	0.5905	4.0469	0.3427	0.6015	0.5738	2.6479
05-1	0.5041	0.3806	0.6087	2.0203	0.3581	0.2292	0.1309	1.4075
05-2	1.0134	0.5779	0.7777	4.4001	0.3783	0.1295	0.2176	1.7126
06-1	0.6171	0.2323	0.3557	1.7950	2.6784	0.5454	0.3104	4.8952
06-2	1.0540	0.2634	0.2798	2.1940	0.8080	0.0984	0.2191	1.9261
06-3	0.8296	0.1578	0.2608	1.5176	0.2794	0.1305	0.4831	0.9139
07-2	0.5737	0.6064	0.2568	2.6448	0.1249	0.7508	0.0847	2.1412
07-4	0.4841	0.1540	0.1234	1.6296	0.2649	0.1341	0.2188	1.0937
08-2	1.0550	0.2126	0.5365	2.4047	0.2471	0.3364	0.2391	1.7814
08-3	0.1898	0.2906	0.5305	1.2730	0.1614	0.3514	0.3996	1.1273
08-4	1.4928	0.6501	0.6554	2.9928	0.1948	0.2884	0.1794	2.0150
09-1	0.3561	0.3979	0.2589	3.4636	1.4087	0.6752	0.2177	4.5477
09-2	0.2365	0.5690	0.5589	1.8848	0.5674	0.3441	0.3116	2.1277
09-3	0.3438	0.5651	0.3388	1.7861	0.0940	0.4804	0.3182	1.5092
09-4	0.6564	0.7843	0.5589	2.2867	3.9230	1.1794	0.2936	5.9214
10-1	6.5819	2.4783	1.4208	19.6943	3.1923	3.7489	2.1824	16.8149
10-2	0.9269	0.6453	0.4742	5.0844	1.9543	0.3587	0.7302	7.4445
10-3	0.4063	0.0943	1.6259	2.4360	1.8395	0.2781	0.0728	5.6944

Table 5.3: Spectral energy integrated over tidal bands for u and $\tilde{v}$, in cm^2 s^{-2} for the second period of observations, except for ACS05-A. The numbers 50-450 refer to depths in m.

responsible for this (Gerkema, 2001). But also changes in ray paths may lead to different reflection patterns, with a different concentration of energy.

To compare, the energy in the semidiurnal band was transformed into overall semidiurnal band velocity amplitudes according to $A = 2\sqrt{(}D_2$-integrated power$)$. The large values in the upper ADCP-observations and ACS10 are in accordance with the model. Especially the large values observed for ACS05-A, which is clearly outside the generation area, are reproduced as an effect of the the pycnocline.

Most current meters were not in these areas of strong motion, they are all well below the pycnocline. Still, there are differences in intensity of the currents, albeit not as large. For ACS09 the upper and lower current meter showed stronger motion, in accordance with the

model. This mooring was just to the south of the island Juan de Nova, that may generate internal waves also. Especially the $\tilde{v}$-component had large amplitudes. In ACS08 the the strongest signal was found for the lowest current meter, although only for the u-component. Still, amplitude and phase differences between the current meters of this mooring were observed, indicating the presence of internal waves. Since motion was weak as compared to the other moorings, the results do not stand out. None of the three current meters were in positions where strong motion was predicted by the numerical model, the results seem consistent. ACS07 exhibited stronger motion for the upper current meter. This current meter is indeed close to a numerically predicted site of strong motion. For ACS06 the correction for the barotropic tide is doubtful, since the current meters may be within a single internal wave beam and vertical averaging may not rule this out. For $\tilde{v}$, the semidiurnal tidal energy is strongest in the upper current meter, for the u-component it is in the second current meter. This mooring has been displaced more than 10 km to the soutwest by the currents. Inspection of the pressure sensor signals of the current meters suggests that this happened some weeks after the deployment. This may explain differences between observations and the model results. For ACS05, the u-component of the bottom current meter was stronger than for the current meter in the middle. In the model, the bottom current meter is indeed close to an area of stronger energy in the no-eddy stratification regime, but for the eddy regime the upper current meter is in an area of stronger motion. A semidiurnal internal wave beam, generated at the shelf, should reflect from the bottom at about this position as predicted by ray theory.

It is not possible to compare the phases of the integrated spectrum, as it was especially the variability of the phases that led to the use of an integrated spectrum. Phases of the short time harmonic analysis can be compared. For ACS09, the observed phase changes in the vertical are in accordance with the numerical model. The changes due to the presence and absence of an eddy lead to mild variations for the lower current meter, but to tremendous variations for the upper current meters. Also the relatively large contribution of the S_2-component, as observed in the intergrated spectra, could contribute to larger phase variations. For the lower current meters of ACS05, the phase changes (not shown) seemed to be relatively slow for large observational periods and the current meters generally had nearly equal phases, as predicted. For ACS10-1, the phase variations in time were relatively small (most jumps were due to the -180 to 180 degrees transition), which may be an effect of the coupling of the barotropic and baroclinic tides in the generation area. The model predicts large phase differences in the vertical, which are different for the two stratification regimes. These could be observed in the 10-2 and 10-3.

In general, the modelled variation of phase and amplitude in horizontal and vertical were large. Mooring motion alone could contribute very much to the intermittency, moving the current meter into and out of regions with strong motion, for example ACS05-1 and ACS08. Also phase changes may be considerable. In addition, the stratification changes nearly continuously due to the slow passage of eddies. Again for the current meters of ACS05 and ACS08-2 changes in phase and amplitude are particularly large. For S_2, similar spatial variations of energy and phase were found from the numerical model. The combination of mooring motion, changes in stratification and the strongly localized regions with energy concentration or large phase jumps must lead to the observed intermittent behaviour.

5.6 Discussion

Internal tides were clearly present in the channel. Direct evidence came from the yo-yo stations, with isotherm displacements of 40 m to 80 m near the shelf. But they only provide a snapshot and are too far apart to be related to each other. Also differences in time with respect to spring time may contribute to amplitude differences.

The current meter observations presented here span a long time. The second period of observations was more successful in the sense that the time resolution and spatial coverage were better. Therefore, in the data analysis mainly results from the second period have been used, except for the ADCP off the shelf. However, the current meter signals reveal only highly variable internal tides, such that it is not possible to speak of *the* internal wave field. The intermittency makes it difficult to relate the signals of the different current meters. It is probably related to changes in wave ray paths due to the passage of eddies which alters the stratification, and changes in current meter positions due to large velocities of the eddies. Also Doppler shifts and changes in the absolute vorticity due to the large velocities in the eddies may put energy to nearby frequencies and alter wave ray paths (Kunze, 1985), but we did not take these effects into account, given other uncertainties. At some locations, the change in phase due to a change of ray path or mooring position may be particularly large, thus accounting for the intermittency (Gerkema, 2002). In this respect, the observations resemble the classical obervations of Magaard & McKee (1973), who have long-time observations in the western North Atlantic, where eddies pass that are shed off by the Gulf stream. A direct connection between amplitude and phase changes of the internal waves and the passage of eddies was not found however. But also in shelf areas intermittency was observed (Lerczak *et al.*, 2003), albeit with a stable vertical structure. In van Haren (2002), the contributions of the different tidal frequencies M_2, S_2 and N_2 could be separated in time and variations in their maxima could be interpreted as changes in ray path. Due to the strong mooring motion this is not possible here.

Calculation of the long-time energy content of the spectral bands of the semidiurnal frequency revealed that energy is concentrated around the pycnocline. This seems not purely an effect of the generation area, as it was also observed 40 km off the shelf. The pycnocline is assumed to play an important role in the behaviour of internal tides: for an intermediate strength waves are scattered whereas a strong pycnocline acts as a reflector such that an internal wave beam preserves its identity (Gerkema, 2001). The pycnocline was indeed rather strong. In the presence of an eddy it is considerably weaker. The exact generation locations and beam structure of the internal tides also seem closely related to the stratification (Gerkema *et al.*, 2003; Lam *et al.*, 2003).

None of the deep current meters revealed strong internal wave amplitudes. The presence of internal waves was however betrayed by phase differences between the current meters, as observed from the short term harmonic analysis of the filtered and barotropic tide-corrected records. Further, the strength of the velocity changed over the basin, maxima were reached at different moments in time, indicating different phases of the M_2 and S_2 tides at different locations.

The numerical internal-tide generation model was only valid for a cross section of an infinitely long channel. In reality, the Mozambique Channel is far from two-dimensional. The bottom topography in the along-channel direction is uniform along the Davie Ridge.

The island Juan de Nova, slightly to the north of ACS09 may generate waves that penetrate into our area of observation. Although the barotropic tide was strongest in the along-channel direction, no attention was paid to other generation areas. Finally, the fact that we observe in the narrowest part means that waves that propagate along the channel will be refracted away from this cross section upon reflection at the coast. This may be a serious limitation for the concentration of energy.

To conclude: internal tides were present, but the appearance for the individual current meters was highly intermittent. When long time averages of the signal were studied, it appears that the upper part of the water column contains the strongest internal tidal currents, but significant isotherm displacement was observed in the interior, where current meters were absent. It would be especially worthwhile to study internal wave currents in the upper few hundred meters, to investigate the effect of scattering and reflection near the pycnocline in more detail.

5.7 Synthesis

In relation to the rest of the thesis, it is clear that the observations cannot be interpreted as a simple wave attractor. This does not mean that the theory about wave focusing and the appearance of attractors is not applicable to the ocean at all.

The most important complication, that has not been discussed in previous chapters, is the effect of a strong spatial variation in stratification, which causes scattering, an effect that is not accounted for in ray theory. This has a large impact on the actual wave field, as shown by the numerical model. But also without scattering wave attractors cannot be readily found. Although internal waves with tidal frequencies are most easily generated, they do not necessarily lead to wave attractors, as the existence of wave attractors depends very much on the wave frequency. It is well possible that a basin of certain basin shape and stratification has potential for wave attractors for frequencies other than the tidal frequencies. Furthermore, in nature, basin shapes are hardly ever enclosed, such that part of the wave rays escapes to the shelf, or uniform in one direction, such that attractors cannot extend in the horizontal.

From the observational side, ocean observations only cover points, or lines for the ADCP's, whereas in the laboratory full cross sections could be observed. Unless a very good model is available and the observational programme is very well designed, interpretation of observations is difficult. Further, the variability in background conditions, resulting in the change of ray paths and therewith in intermittency, will complicate the detection of structure.

Still, the numerical tide generating model indeed showed that energy is distributed very unevenly, with patches of high concentration. Such patches cannot be predicted by low modes only, also high modes must be taken into account, as well as reflection at the bottom. The bottom topography is responsible for the generation, but it appears to determine the spatial distribution of wave energy as well. Despite the scattering, in the deep sea structures are very beam-like. This means that understanding reflection at the bottom remains an essential part of the understanding of inertial wave behaviour. It is very well possible that in the ocean "echoes" of internal wave attractors can be observed as isolated spots of high internal wave energy, that cannot be directly related to a generation area. In that respect, despite all its limitations, this thesis may contribute to understanding the behaviour of internal waves in oceans

and lakes.

This chapter is a manuscript by A.M.M. Manders, L.R.M. Maas and T. Gerkema. We thank H. Ridderinkhof for the realization of the observations and the crews of the Pelagia, Darwin and Bazaruto for their assistance.

Bibliography

Aldridge, K. D. 1972 Axisymmetric inertial oscillations of a fluid in a rotating spherical shell. *Mathematika* **19**, 163–168.

Aldridge, K. D. & Lumb, L. 1987 Inertial waves identified in the earth's fluid core. *Nature* **325**, 421–423.

Aldridge, K. D., Lumb, L. I. & Henderson, G. A. 1989 A poincaré model for the earth's fluid core. *Geophys. Astrophys. Fluid Dyn.* **48**, 5–23.

Aldridge, K. D. & Toomre, A. 1969 Axisymmetric inertial oscillations of a fluid in a rotating spherical container. *J. Fluid Mech.* **37**, 307–323.

Arnol'd, V. I. 1965 Small denominators. I Mappings of the circumference to itself. *Am. Math. Soc. Transl. Series 2* **46**, 213–263.

Arnol'd, V. I. & Khesin, B. A. 1998 *Topological methods in hydrodynamics*. Springer, New York.

Baines, P. G. 1967 Forced oscillations of an enclosed rotating fluid. *J. Fluid Mech.* **30**, 533–546.

Baines, P. G. 1986 Internal tides, internal waves and near-inertial motions. In *Baroclinic processes on continental shelves* (ed. N. K. Mooers). American Geophysical Union.

Beardsley, R. C. 1970 An experimental study of inertial waves in a closed cone. *Stud. Appl. Maths.* **49**, 187–196.

Bourgin, D. G. 1939 The Dirichlet problem for the damped wave equation. *Bull. Am. Math. Soc.* pp. 97–120.

Bourgin, D. G. & Duffin, R. 1939 The Dirichlet problem for the vibrating string equation. *Bull. Am. Math. Soc.* **45**, 851–858.

Bretherton, P. 1964 Low frequency oscillations trapped near the equator. *Tellus* **XVI** (2), 181–185.

Bryan, G. 1889 The waves on a rotating liquid spheroid of finite ellipticity. *Phil. Trans. R. Soc. London* **180**, 187–219.

Cacchione, D. & Wunsch, C. 1974 Experimental study of internal waves over a slope. *J. Fluid Mech.* **66**, 223–239.

Cartan, M. E. 1922 Sur les petites oscillations d'une masse de fluide. *Bull. des Sciènces Math.* **46**, 317–369.

Coddington, E. A. & Levinson, N. 1955 *Theory of ordinary differential equations*. McGraw-Hill, New York.

Dauxois, T. & Young, W. R. 1999 Near-critical reflection of internal waves. *J. Fluid Mech.* **390**, 271–295.

De Melo, W. & van Strien, S. 1993 *One-Dimensional Dynamics*. Springer.

DiMarco, S. F., Chapman, P., W. D. Nowlin Jr., Hacker, P., Donohue, K., Luther, M., Johnson, G. C. & Toole, J. 2002 Volume transport and property distributions of the Mozambique Channel. *Deep-Sea Research II* **49**, 1481–1511.

Dintrans, B., Rieutord, M. & Valdettaro, L. 1999 Gravito-inertial waves in a rotating stratified sphere or spherical shell. *J. Fluid Mech.* **398**, 271–297.

Egbert, G. D. & Ray, R. D. 2001 Estimates of M2 tidal energy dissipation from TOPEX/Poseidon altimeter data. *J. Geoph. Res.* **106**, 22475–22502.

Eriksen, C. C. 1982 Observations of internal wave reflection off sloping bottoms. *J. Geoph. Res.* **87** (C1), 525–538.

Fincham, A. & Spedding, G. R. 1997 Low cost, high resolution dpiv for measurement of turbulent fluid flow. *Exp. in Fluids* **23**, 449–462.

Franklin, J. N. 1972 Axisymmetric inertial oscillations of a rotating fluid. *Jour. of Math. Anal. and Appl.* **39**, 742–760.

Franks, P. J. S. 1995 Thin layers of phytoplankton: a model of formation by near-inertial wave shear. *Deep-Sea Research* **42**, 75–91.

Fricker, P. D. & Nepf, H. M. 2000 Bathymetry, stratification, and internal seiche structure. *J. Geoph. Res.* **105**, 14237–14251.

Friedlander, S. 1982 Turning surface behaviour for internal waves subject to general gravitational fields. *Geophys. Astrophys. Fluid Dyn* **21**, 189–200.

Friedlander, S. & Siegmann, W. L. 1982 Internal waves in a rotating stratified fluid in an arbitrary gravitational field. *Geophys. Astrophys. Fluid Dyn* **19**, 267–291.

Fu, L.-L. 1981 Observations and models of inertial waves in the deep ocean. *Rev. Geoph. Space Phys.* **19**, 141–170.

Fultz, D. 1959 A note on the overstability and the elastoid-inertia oscillations of Kelvin, Solberg and Bjerknes. *J. Meteorl.* **16**, 199–208.

Garrett, C. & Munk, W. 1972 Space-time scales of internal waves. *Geophys. Fluid Dyn.* **2**, 225–264.

Genin, A., Paull, C. K. & Dillon, W. P. 1992 Anomalous abundances of deep-sea fauna on a rocky bottom exposed to strong currents. *Deep-Sea Research* **39**, 293–302.

Gerkema, T. 2001 Internal and interfacial tides: beam scattering and local generation of solitary waves. *J. Mar. Res.* **59**, 227–255.

Gerkema, T. 2002 Application of an internal tide generation model to baroclinic spring-neap cycles. *J.Geophys. Res.* **107**, doi:10.1029/2001JC001177.

Gerkema, T., Lam, F.-P. A. & Maas, L. R. M. 2003 Internal tides in the Bay of Biscay: conversion rates and seasonal effects. *subm. to Deep Sea Res. II* .

Gill, A. E. 1982 *Atmosphere-Ocean Dynamics*. Academic Press.

Görtler, H. 1943 Über eine Schwingungserscheinung in Flüssigkeiten mit stabiler Dichteschichtung. *Z. angew. Math. Mech.* **23**, 65–71.

Görtler, H. 1944 Einige Bemerkungen über Strömungen in rotierenden Flüssigkeiten. *Z. angew. Math. Mech.* **25**, 210–214.

Greenspan, H. P. 1968*a* On the inviscid theory of rotating fluids. *Stud. Appl. Math.* **48**, 19–28.

Greenspan, H. P. 1968*b* *The theory of rotating fluids*. Cambridge University Press.

van Haren, H. 2002 Incoherent internal tidal currents in the deep-ocean. *Subm. to Ocean Dyn.* .

van Haren, H., Maas, L. & van Aken, H. 2002 On the nature of internal wave spectra near a continental slope. *Geoph. Res. Let.* **29**, doi:10.1029/2001GL014341.

van Haren, H. & Millot, C. 2003 Rectilinear and circular inertial motions in the Western Mediterranean Sea. *Oceanol. Acta* **in press**.

van Heijst, G. J. F., Maas, L. R. M. & Williams, C. W. M. 1994 The spin-up of fluid in a rectangular container with a sloping bottom. *J. Fluid Mech.* **265**, 125–159.

Henderson, G. A. & Aldridge, K. D. 1992 A finite-element method for inertial waves in a frustum. *J. Fluid Mech.* **234**, 317–327.

Høiland, E. 1962 Discussion of a hyperbolic equation relating to inertia and gravitational fluid oscillations. *Geofys. Publ.* **XXIV** (6), 211–227.

Hollerbach, R. & Kerswell, R. R. 1995 Oscillatory internal shear layers in rotating and precessing flows. *J. Fluid Mech.* **298**, 327–339.

Holloway, P. E., Chatwin, P. G. & Craig, P. 2001 Internal tide observtions from the Australian North West shelf in summer 1995. *J. Phys. Oc.* **31**, 1182–1199.

Israeli, M. 1972 On trapped oscillations of rotating fluids in spherical shells. *Stud. Appl. Maths.* **51**, 219–237.

Ivey, G. N. & Nokes, R. I. 1989 Vertical mixing due to the breaking of critical internal waves on sloping boundaries. *J. Fluid Mech.* **204**, 479–500.

John, F. 1941 The Dirichlet problem for a hyperbolic equation. *Am. J. Math.* **63**, 141–154.

John, F. 1978 *Partial differential equations*. Springer Verlag, New York.

Kelvin, L. 1880 Vibrations of a columnar vortex. *Phil. Mag.* **10**, 155–168.

Krauss, W. 1966 *Interne Wellen*. Gebr. Borntraeger, Berlin.

Kunze, E. 1985 Near-inertial wave propagation in geostrophic shear. *J. Phys. Oc* **15**, 544–565.

Lam, F.-P. A., Maas, L. R. M. & Gerkema, T. 2003 Spatial structure of tidal and residual currents as observed over the shelf break in the Bay of Biscay. *subm to* .

Leaman, K. D. 1980 Some observations of baroclinic diurnal tides over a near-critical bottom slope. *J. Phys. Oc* **10**, 1540–1551.

LeBlond, P. H. & Mysak, L. A. 1978 *Waves in the Ocean*. Elsevier.

LeProvost, C. 2001 Ocean tides. In *Satellite altimetry and Earth sciences* (ed. L.-L. Fu & A. Cazenave). Academic Press.

Lerczak, J. A., Winant, C. D. & Hendershott, M. C. 2003 Observations of the semidiural internal tide on the southern California slope and shelf. *J. Geophys. Res.* **108** (C3), dOI 10.1029/2001JC001128.

Levine, M. D. 2002 A modification of the Garrett-Munk internal wave spectrum. *J. Phys. Oc.* **32**, 3166–3181.

Maas, L. R. M. 2001 Wave focusing and ensuing mean flow due to symmetry breaking in rotating fluids. *J. Fluid Mech.* **437**, 13–28.

Maas, L. R. M. 2003 On the amphidromic structure of inertial waves in a rectangular parallelepiped. *Fluid Dyn. Res.* **in press**.

Maas, L. R. M., Benielli, D., Sommeria, J. & Lam, F.-P. A. 1997 Observation of an internal wave attractor in a confined, stably stratified fluid. *Nature* **388**, 557–561.

Maas, L. R. M. & van Haren, J. J. M. 1987 Observations on the vertical structure of tidal and inertial currents in the central North Sea. *J. Mar. Res.* **45**, 293–318.

Maas, L. R. M. & Lam, F.-P. A. 1995 Geometric focusing of internal waves. *J. Fluid Mech.* **300**, 1–41.

Magaard, L. & McKee, W. D. 1973 Semidiurnal tidal currents at ‘site D’. *Deep-Sea Research* **20**, 997–1009.

Magnus, W., Oberhettinger, F. & Soni, R. P. 1966 *Formulas and Theorems for the Special Functions of Mathematical Physics, 3rd edn*. Springer.

Malkus, W. V. R. 1968 Precession of the Earth as the cause of geomagnetism. *Science* **160** (3825), 259–264.

Manasseh, R. 1992 Breakdown regimes of inertia waves in a precessing cylinder. *J. Fluid Mech.* **243**, 261–296.

Manasseh, R. 1993 Visualization of the flows in precessing tanks with internal baffles. *Am. Inst. Aeronaut. Astronaut. J.* **31**, 312–318.

McEwan, A. D. 1970 Inertial oscillations in a rotating fluid cylinder. *J. Fluid Mech.* **40**, 603–640.

Morozov, E. G. 1995 Semidiurnal internal wave global field. *Deep-Sea Res. I* **42**, 135–148.

Munk, W. & Wunsch, C. 1998 Abyssal recipes II: energetics of tidal and wind mixing. *Deep-Sea Res. I* **45**, 1977–2010.

Myint-U, T. & Debnath, L. 1987 *Partial differential equations for scientists and engineers*. New York: North Holland.

Oser, H. 1958 Experimentelle Untersuchung über harmonische Schwingungen in rotierenden Flüssigkeiten. *Z. angew. Math. Mech.* **38** (9/10), 386–391.

Petruncio, E. T., Rosenfeld, L. K. & Paduan, J. D. 1998 Observations of the internal tide in Monterey Canyon. *J. Phys. Oc.* **28**, 1873–1903.

Phillips, O. M. 1963 Energy transfer in rotating fluids by reflection of inertial waves. *The Physics of Fluids* **6**, 513–520.

Pingree, R. D. & New, A. L. 1991 Abyssal penetration and bottom reflection of internal tidal energy in the Bay of Biscay. *J. Phys. Oc.* **21**, 28–39.

van der Plas, G. A. J. & Bastiaans, R. J. M. 2000 The fptvwiz algorithm and its validation with synthetic data. *Tech. Rep.*. Eindhoven University of Technology.

Poincaré, H. 1885 Sur l' équilibre d'une masse fluide animée d'un mouvement de rotation. *Acta Mathematica* **VIII**, 259–380.

Ray, R. D. & Mitchum, G. T. 1997 Surface manifestation of internal tides in the deep ocean: observations from altimetry and island gauges. *Prog. Oceanog.* **40**, 135–162.

Ridderinkhof, H. & de Ruijter, W. P. M. 2003 Moored current observations in the mozambique channel. *Deep Sea Res. II* **50/12-13**, 1933–1955.

Rieutord, M. 1995 Inertial modes in the liquid core of the Earth. *Phys. Earth. Plan. Int.* **91**, 41–46.

Rieutord, M., Georgeot, B. & Valdettaro, L. 2001 Inertial waves in a rotating spherical shell: attractors and asymptotic spectrum. *J. Fluid Mech.* **435**, 103–144.

Rieutord, M. & Valdettaro, L. 1997 Inertial waves in a rotating spherical shell. *J. Fluid Mech.* **341**, 77–99.

Rieutord, M., Valdettaro, L. & Georgeot, B. 2002 Analysis of singular inertial modes in a spherical shell: the slender toroidal shell model. *J. Fluid Mech.* **463**, 345–360.

Robertson, R. 2001 Internal tides and baroclinicity in the Southern Weddell Sea 2. effects of the critical latitude and stratification. *J. Geoph. Res. C11* **106**, 2000JC000467.

Schuman, E. H. 1998 *The Sea*, , vol. 11, chap. The coastal ocean off southeast Africa, including Madagascar. John Wiley&Sons.

Schuster, H. G. 1984 *Deterministic chaos*. Physik Verlag.

Sjöberg, B. & Stigebrandt, A. 1992 Computations of the geographical distribution of the energy flux to mixing processes via internal tides and the associated vertical circulation in the ocean. *Deep-Sea Res.* **39**, 269–291.

Stern, M. E. 1963 Trapping of low frequency oscillations in an equatorial 'bounday layer'. *Tellus* **XV** (3), 246–250.

Stewartson, K. 1971 On trapped oscillations of a rotating fluid in a thin spherical shell. *Tellus* **XXII** (6), 506–510.

Stewartson, K. 1972 On trapped oscillations of a rotating fluid in a thin spherical shell ii. *Tellus* **XXIV** (4), 283–286.

Stewartson, K. & Rickard, J. A. 1969 Pathological oscillations of a rotating fluid. *J. Fluid Mech.* **5**, 577–592.

Tilgner, A. 1999 Driven inertial oscillations in spherical shells. *Phys. Review E* **59**, 1789–1794.

Tolstoy, I. 1973 *Wave propagation*. McGraw-Hill.

Turner, J. S. 1973 *Buoyancy effects in fluids*. Cambridge University Press.

van Veldhoven, A. K. 2000 The propagation of internal tides in the Faeroe-Shetland channel. Master's thesis, Utrecht University, iMAU V-00-06.

Veronis, G. 1970 The analogy between rotating and stratified fluids. *Ann. Rev. Fluid Mech.* **2**, 37–66.

Wood, W. W. 1965 Properties of inviscid, recirculating flows. *J. Fluid Mech.* **22**, 337–346.

Wunsch, C. 1969 Progressive internal waves on slopes. *J.Fluid Mech.* **35**, 131–144.

Wunsch, C. 1975 Deep ocean internal waves: what do we really know? *J. Geophys. Res* **80**, 339–343.

Wunsch, C. 1976 Geographical variability of the internal wave field: A search for sources and sinks. *J. Phys. Oceanogr* **6**, 471–485.

Samenvatting

Interne golven

Overal om ons heen zijn golven te vinden. De bekendste zijn wel die op het wateroppervlak. Golven danken hun bestaan aan een stabiel basisevenwicht. Als dat verstoord wordt gaat een terugdrijvende kracht werken om deze verstoring terug naar zijn evenwichtspositie te brengen. Maar de evenwichtspositie wordt voorbijgeschoten, en een tegengesteld gerichte terugdrijvende kracht gaat werken. Er ontstaat een golf. De aard van het basisevenwicht bepaalt de classificatie van de golven. Voor golven op het wateroppervlak bijvoorbeeld is deze terugdrijvende kracht de zwaartekracht, het zijn zwaartekrachtsgolven. Alleen de verstoring van de evenwichtspositie (energie) plant zich voort, de vloeistofdeeltjes zelf keren uiteindelijk terug naar hun rustpositie.

Minder bekend is dat er ook golven *door* de vloeistof lopen, zogenaamde *interne golven*. Deze golven hebben een maximale uitwijking in het interieur, het vloeistofoppervlak beweegt nauwelijks. Zij danken hun bestaan aan een stabiele gelaagdheid van de vloeistof. Het eenvoudigste voorbeeld is een glas gevuld met water en lichtere olie, waarbij golven op het grensvlak water-olie lopen, terwijl het oppervlak vrijwel in rust is. Voor een vloeistof die stabiel gelaagd is in dichtheid heten deze golven *interne zwaartekrachtsgolven* omdat de zwaartekracht (dan wel de opwaartse kracht) ten gevolge van dichtheidsverschillen de terugdrijvende kracht is. Interne golven in een vloeistof met lagen van duidelijk verschillende dichtheid worden ook wel grensvlakgolven genoemd. Maar ook continu gelaagde vloeistoffen, waarbij de dichtheid langzaam verandert, kunnen interne golven bevatten. Deze lopen schuin door de vloeistof ten opzichte van de richting van de zwaartekracht (vertikaal). Zij hebben de bijzondere eigenschap dat de hoek met de vertikaal waaronder de beweging zich voortplant alleen afhankelijk is van de verhouding tussen de frequentie van de golf en de zogenaamde Brunt-Väisälä-frequentie, die door het dichtheidsverloop bepaald is. De vloeistofdeeltjes trillen langs lijnen die deze hoek maken. Het golfveld zelf kan daarmee als tweedimensionaal worden opgevat.

Een homogene, maar uniform roterende vloeistof kan ook in zekere zin gelaagd zijn. Vloeistof die verder van de rotatie-as is, moet een hogere snelheid hebben om in dezelfde tijd een omwenteling gemaakt te hebben dan vloeistof met een kleinere straal. De vloeistof is gelaagd in impulsmoment (snelheid maal straal). Deze gelaagdheid is radieel. Als een kleine hoeveelheid vloeistof uit zijn evenwichtspositie gebracht wordt heeft het een ander impulsmoment dan zijn nieuwe omgeving en zal een relatieve snelheid hebben. Ten gevolge

van een traagheidskracht, die in een met de vloeistof meeroterend coördinaatstelsel bekend is als de Corioliskracht, zal het vloeistofdeeltje langs cirkelvormige banen gaan oscilleren ten opzichte van een waarnemer die meedraait met de uniforme rotatie. Deze golven worden *traagheidsgolven* of *inertiaalgolven* genoemd. Ook hier lopen de golven schuin door de vloeistof, met een hoek die nu bepaald wordt door de verhouding tussen de golffrequentie en de rotatiefrequentie. Door de cirkelvormige deeltjesbeweging wordt het golfveld intrinsiek driedimensionaal.

Interne zwaartekrachtsgolven en de traagheidsgolven hebben eigenschappen die nauw verwant zijn. In een vloeistof die uniform roteert èn gelaagd is in dichtheid zijn de beide soorten interne golven gecombineerd in één soort golf. Deze golven worden algemeen waargenomen in meren, zeeën en oceanen, die ook bestaan uit dichtheidsgelaagde, roterende vloeistoffen. Een gedeelte van de grootschalige getijstromingen wordt omgezet in interne golven (interne getijden) wanneer deze stromingen over de continentale helling of oceanische ruggen gericht zijn. De interne getijden kunnen op hun beurt door reflectie aan de hellende bodem tot locale menging leiden. Hoeveel en waar menging plaatsvindt is weer van belang voor de grootschalige stromingen. Maar ook voor het interieur van sterren en de vloeibare buitenkern van de aarde kunnen interne golven van belang zijn. Hier kunnen zij bijvoorbeeld worden opgewekt door zware diepe aardbevingen of kleine bewegingen van de rotatie-as.

Zoals gezegd lopen de interne golven schuin door de vloeistof. De paden waarlangs de golfenergie door de vloeistof loopt worden ook *golfstralen* genoemd. De vier mogelijke richtingen vanuit een punt vormen in een zijaanzicht een zogenaamd Andreaskruis. Als een golf reflecteert, veranderen de achtergrondgelaagdheid en de golffrequentie niet, zodat de gereflecteerde golf nog steeds onder een van deze richtingen moet wegelopen. Dit heeft vooral consequenties voor reflectie aan een schuine wand (niet parallel aan een van de symmetrieassen van het Andreaskruis). Na reflectie komen twee golfstralen ofwel dichter bij elkaar, resulterend in een sterkere beweging van de vloeistof (*focussering*) of raken juist verder van elkaar, waarbij de beweging zwakker wordt (*defocussering*).

Golfpatronen in twee dimensies

In dit proefschrift wordt het gedrag van reflecterende interne golven in afgesloten bekkens onderzocht. In eerste instantie werd gekeken naar golven in een oneindig lang kanaal, die niet in de kanaalrichting lopen. Een beschrijving in een doorsnede volstaat dan, wat het vinden van golfpatronen aanzienlijk vereenvoudigt. Omdat de vrijheid in voortplantingsrichting ernstig beperkt is, zal herhaalde reflectie aan de wanden van het kanaal niet leiden tot chaotische patronen zoals voor het klassieke ‘biljartprobleem’, waarbij alle richtingen mogelijk zijn, maar juist tot gestructureerde patronen. Het meest bekend zijn de oplossingen in termen van *staande golven*, waarbij alle golfstralen na een eindig aantal reflecties op zichzelf terugkomen (golfstralen zijn periodiek). De oplossingen kunnen dan geschreven worden als som van golven die precies passen in deze doorsnede. Bij een kleine verandering van de voortplantingsrichting of de vorm van het kanaal passen deze patronen niet meer en kan alleen de nuloplossing gevonden worden. Bij verdere veranderingen kan weer een nieuwe staande golf bestaan, met golfstralen die na een ander aantal reflecties op zichzelf terugkeren.

Het kan ook voorkomen dat slechts een beperkt aantal periodieke stralen bestaat. Nu lo-

pen de stralen in de richting van deze paar periodieke banen door herhaalde focussering aan de wanden. Deze periodieke banen fungeren als 'limietbanen' of *aantrekkers*, en alle energie raakt geconcentreerd rond deze aantrekkers. Deze concentratie kan vervolgens leiden tot het breken van golven als de beweging te sterk wordt, of op een andere manier leiden tot het lokaal mengen van de vloeistof. Voor een roterende vloeistof kan deze menging leiden tot een netto stroming. Zulke aantrekkers zijn minder gevoelig voor verandering van voortplantingsrichting en vorm van het kanaal, zij bestaan over *intervallen* van richtingen en vorm. Ook hier geldt dat de patronen bij te grote verandering niet meer passen, en dat voor een grotere verandering periodieke banen met een ander aantal reflectiepunten worden gevonden.

De achterliggende vergelijking die de hierboven beschreven patronen bepaalt is de golfvergelijking in twee ruimtelijke dimensies. De tijd kan buiten beschouwing gelaten worden door steeds golven van één frequentie te bekijken, zodat het patroon slechts bepaald wordt door de mogelijke voortplantingsrichting (afhankelijk van de frequentie) en de vorm van het kanaal. Ondanks de ogenschijnlijke eenvoud van het probleem is het niet eenvoudig om oplossingen van de golfvergelijking en daarmee patronen te vinden. Voor een kanaal met rechte wanden of een buis kan de vergelijking opgesplitst worden in twee nog eenvoudiger vergelijkingen: één voor elke ruimtelijke coördinaat, waarvoor de oplossingen eenvoudig aan de randvoorwaarden (geen beweging door de rand) kunnen voldoen. Dit geeft dan de staande golven. Als een kanaal echter hellende wanden heeft kan deze scheidingsmethode niet gebruikt worden, omdat dan de randvoorwaarde op een combinatie van deze coördinaten toegepast moet worden.

Een alternatief is dan om een oplossing te *construeren* door voor elk punt in de doorsnede te berekenen waar de stralen door dit punt de rand snijden. De druk op de rand bepaalt wat voor druk er door deze golfstralen naar het binnenste wordt doorgegeven. De druk op de rand wordt weer bepaald door de manier van opwekken van golven. In de wiskunde wordt een dergelijke methode, waarbij gekeken wordt naar het gedrag van de oplossing langs specifieke lijnen de *methode van karakteristieken* genoemd. Een complicatie voor een doorsnede van een kanaal is dat als er periodieke banen zijn, de druk aan de rand ook periodiek moet zijn. Alleen specifieke drukverdelingen zorgen dat er geen strijdigheden ontstaan. De methode van karakteristieken wordt dan ook meestal toegepast in tijdafhankelijke problemen, waar een golfstraal nooit terugkomt op hetzelfde punt in tijd en ruimte. In het onderhavige geval kunnen dergelijke complicaties waarschijnlijk ook gerepareerd worden door het volledige tijdafhankelijke probleem te beschrijven. Omdat het beschrijven van de ruimtelijke patronen alleen al moeilijk genoeg is wordt in dit proefschrift de aandacht daarop gericht.

Een voor de hand liggende vraag is of er iets bijzonders is met een bekkenrand om aantrekkers mogelijk te maken, afgezien van een helling die de symmetrie ten opzichte van het Andreaskruis breekt. Zulke bijzonderheden zijn bijvoorbeeld hoeken, waar de rand niet meer glad is, of uitstulpingen naar binnen toe. Om deze vraag te beantwoorden is in hoofdstuk 2 een speciale rand gekozen. Deze rand bevatte geen hoeken en instulpingen, en varieerde tussen een cirkel (uiterste geval) en een driehoek (uiterste geval), afhankelijk van een storingsparameter. Voor de cirkel is bekend dat er geen golfaantrekkers mogelijk zijn: of alle golfstralen zijn periodiek, of alle golfstralen blijven reflecteren zonder ooit op zichzelf terug te keren, voor de driehoek reflecteren de golfstralen richting de hoekpunten, waaruit ze niet kunnen ontsnappen. Wiskundigen zien reflectie in een gesloten gebied als een afbeelding van de rand van dit gebied op zichzelf. Om het gedrag te beschrijven werd gebruik gemaakt van

de theorie die hiervoor bekend is.

Golfstralen met verschillende voortplantingsrichtingen (frequenties) werden numeriek gevolgd over een groot aantal reflecties en de eventuele convergentie naar een aantrekker werd in kaart gebracht. Golfaantrekkers werden inderdaad algemeen gevonden. Het aantrekken was sterker naarmate de vorm meer verwant was aan de driehoek. De randen van de intervallen werden gevormd door frequenties waarvoor kritieke punten (punten waar de raaklijn aan de rand parallel is aan de golfstraal) met elkaar werden verbonden door een golfstraal, zodat de aantrekker degenereerde tot een lijn, en door frequenties waarvoor twee aantrekkers, die elkaars spiegelbeeld waren, samenvielen en elkaar annihileerden. Aan de randen van deze intervallen ging het aantrekken nog maar heel langzaam. Er was één frequentie die door een extra symmetrie voor alle randparameters leidde tot een staande golf. Als deze symmetrie verstoord werd door de bekkenrand iets te draaien verdween deze staande golf, en veranderde de ordening van de frequentie-intervallen met betrekking tot de periode van de aantrekker (aantal reflecties van de periodieke baan die de aantrekker vormt). Ook werd met eerste orde storingstheorie (waarmee je het effect van kleine veranderingen bekijkt) gekeken naar het bestaan van aantrekkers voor algemene randen die gezien kunnen worden als kleine verstoringen van de cirkel. Voor de bekeken kanaalrand moest het breder worden van een frequentie-interval van de eenvoudigste aantrekker met het groter worden van de rand-storingsparameter worden beschreven met tweede orde storingstheorie (nog kleinere veranderingen bekijken). Het ontbreken van hoeken en uitstulpingen leidde niet tot de afwezigheid van aantrekkers, maar wel tot het ontbreken van sprongen of oneindigheden in de sterkte van de aantrekker.

Golfpatronen in drie dimensies

In drie dimensies wordt het ruimtelijke patroon van inwendige golven nog moeilijker te beschrijven dan in twee dimensies. Voor de zogeheten Poincarévergelijking, de golfvergelijking in drie ruimtelijke coördinaten, geldt weer dat alleen voor de eenvoudigste vormen van het bekken (een cylinder, bol of rechthoekige bak) oplossingen gevonden kunnen worden door de vergelijking op te delen in eenvoudigere vergelijkingen. De methode van karakteristieken kan nu niet gebruikt worden, en de wiskundige ‘opvolger’, geschikt voor vergelijkingen voor twee ruimtelijke dimensies en de tijd, leidt tot te grote complicaties wat betreft voorwaarden voor de druk op de rand.

Als hulpmiddel werd weer naar golfstralen gekeken. Deze kunnen weliswaar niet gebruikt worden om een volledige oplossing te construeren, zoals in twee dimensies, maar geven wel ondersteuning bij het vinden van mogelijk gedrag. Uit stralentheorie volgt dat golfstralen hun hoek met de richting van de zwaartekracht en/of de rotatie-as moeten behouden. In drie dimensies betekent dat dat golven langs kegels lopen waarvan de tophoek bepaald wordt door de golffrequentie en de dichtheidsverdeling en/of de rotatiesnelheid. De hoek in het horizontale vlak is echter vrij. Bij reflectie aan een schuine wand zal de golf dan ook niet alleen reflecteren zoals hiervoor beschreven, maar in horizontale richting ook breken, wat wil zeggen dat de gereflecteerde golf een andere hoek maakt in het horizontale vlak dan de inkomende.

Focusserende reflectie gaat vergezeld van breking, zodanig dat de gereflecteerde golf-

straal een kleinere hoek maakt met een doorsnede van het kanaal dan de inkomende. Voor frequenties waarvoor een tweedimensionale aantrekker werd voorspeld kunnen daarom ook in drie dimensies golfstralen naar een aantrekker gaan. Op welke positie in de kanaalrichting de aantrekker bereikt wordt is echter sterk afhankelijk van de startpositie en aanvankelijke hoek in het horizontale vlak. Voor een situatie waarin in twee dimensies een staande golf zou ontstaan zal een golf die begint met een component van voortplanting in de horizontale richting niet convergeren naar een vaste positie, daar de balans tussen focussering en defocussering ook een balans tussen convergentie en divergentie in de horizontale richting geeft.

Het is echter niet mogelijk om een echte oplossing te vinden door naar individuele stralen te kijken. Ook de interactie tussen golfstralen, zoals versterking en uitdoving, moet meegenomen worden om het golfveld adequaat te beschrijven.

Laboratoriumobservaties

Om de voorspellingen van aantrekkers te verifiëren en om de driedimensionale structuur van het golfveld te bestuderen zijn laboratoriumexperimenten uitgevoerd. Een langwerpige, rechthoekige bak werd voorzien van een hellende zijwand om een aantrekker mogelijk te maken. Deze bak werd gevuld met kraanwater en zeer kleine zwevende bolletjes voor de visualisatie. De bak werd op een roterend platform geplaatst, waarbij de rotatiesnelheid regelmatig gevarieerd werd rond een basisrotatie om inertiaalgolven op te wekken met een frequentie gelijk aan de frequentie van de regelmatige variatie. Door in een verduisterde ruimte een dun vlak in de vloeistof te belichten en dit te registreren met een digitale camera werd de beweging vastgelegd. Met beeldverwerkingsprogramma's werden deze beelden door de computer vertaald naar tweedimensionale snelheidsvelden. Verscheidene golffrequenties werden gebruikt om verscheidene aantrekkers en een staande golf op te wekken. Metingen werden in verschillende horizontale en verticale vlakken verricht om een ruimtelijk beeld van het golfveld te verkrijgen. Twee reeksen van experimenten zijn gedaan: één in een grote bak (breedte$\times$lengte$\times$hoogte=107$\times$500$\times$80 cm) op het 13 m diameter roterend platform van het Coriolislaboratorium in Grenoble (Frankrijk) en een in een veel kleinere bak (19$\times$40$\times$19.5 cm) op een 1 m diameter roterend platform in het Vloeistofdynamisch Laboratorium van de Technische Universiteit Eindhoven.

In de eerste reeks van metingen (hoofdstuk 3) zijn zes verschillende frequenties onderzocht: vier binnen het frequentie-interval van de eenvoudigste aantrekker, waarvan twee rond het midden en twee aan de rand van het interval, één waarvoor een staande golf verwacht werd en één voor een iets gecompliceerdere en zwakkere aantrekker. Alle voorspelde vormen zijn waargenomen. Voor de theoretisch sterkste aantrekkers was de beweging het sterkst, voor de staande golf was deze zwakker en de gecompliceerdere aantrekker was niet in zijn geheel zichtbaar als baan van versterkte beweging. De staande golf onderscheidde zich inderdaad in fasegedrag in de verticale doorsnedes: de beweging veranderde uniform van fase, terwijl voor de aantrekkers de fase zich voortplantte in het vlak van observatie. In de horizontale richting nam de bewegingssterkte voor de sterke aantrekkers af met het naderen van het midden van de tank. Voor de zwakke aantrekkers en de staande golf werd de beweging weer wat sterker naar het midden toe. Voor de aantrekker waarvoor de golfstralen parallel aan de hellende wand liepen (kritische reflectie) was er sprake van faseveranderingen naar het midden toe

met een golflengte van 1/4 tot 1/5 van de baklengte, voor de andere aantrekkers en de staande golf werd dit niet waargenomen of kon dit niet goed geobserveerd worden door technische beperkingen van het experiment.

In de tweede reeks experimenten (hoofdstuk 4) kon de variatie in de horizontale richting beter bestudeerd worden, omdat het hele horizontale vlak tegelijk in beeld gebracht kon worden. Nu werden slechts drie frequenties onderzocht, behorend bij kritische reflectie, een eenvoudige aantrekker en een staande golf. Opnieuw werd fasevoortplanting in de horizontaal gevonden voor de kritische reflectie. Voor de eenvoudige aantrekker werd gedrag gelijkend op dat van een staande golf gevonden in de horizontaal, met een aantrekker die duidelijk zichtbaar was op 1/4 en 3/4 van de lengte, maar nauwelijks nabij de uiteinden van het kanaal en halverwege. Halverwege was er een fasesprong, de twee gedeeltes waren in tegenfase. Dit suggereert een staande golf met een knooplijn in het midden als structuur in de lengterichting. Voor de staande golf werd geen voortplanting in de horizontaal gevonden, de beweging was het sterkste rond het midden, de fasestructuur suggereert de laagste orde staande golf in de lengterichting.

De puur wiskundige aantrekker, met alle energie geconcentreerd op een lijn, is fysisch niet mogelijk. Lineaire golven geven een goede beschrijving van het verschijnen van een aantrekker, maar waar energie geconcentreerd raakt gaan andere processen van belang worden. Het blijkt dat bij de aantrekker niet-lineaire termen een rol gaan spelen, namelijk een term die gevormd wordt door de snelheid maal de ruimtelijke verandering van de snelheid (niet-lineaire advectie van snelheid). Deze blijkt te zorgen voor het evenwicht tussen focussering en verlies van snelheid en bepaalt daarmee de eindige dikte van de aantrekker.

Observaties van interne getijden in het Mozambiquekanaal

De wanden van meren en zeeën zijn veelal hellend. Naar menselijke maatstaven zijn deze hellingen flauw, maar ten opzichte van de voortplantingsrichting van interne golven in deze bekkens is dat zeker niet het geval. Focussering zou dus ook hier tot het ontstaan van golfaantrekkers kunnen leiden. Hoewel interne getijden in de oceaan algemeen waargenomen worden is er slechts weinig bekend over hun ruimtelijke verdeling op regionale schaal, behalve dan vlak bij de continentale helling. In hoofdstuk 5 worden waarnemingen beschreven uit het Mozambiquekanaal, een zeestraat tussen Mozambique en Madagascar. Het heeft een redelijk sterk getij (oppervlaktegetij ongeveer 1 meter) en sterke topografie (ongeveer 400 km breed, 2500 m diep). Het grootste gedeelte van de metingen bestaat uit stroomsnelheden en -richtingen, uit stroommeters die in totaal ruim anderhalf jaar hebben gemeten op diverse plaatsen in het kanaal. Ook zijn tijdens de vaartochten in het kanaal profielen bepaald van o.a. temperatuur en zoutgehalte van het water.

Interne getijden zijn inderdaad waargenomen in het Mozambiquekanaal. Kenmerkend is dat zij niet permanent aanwezig zijn, ze worden onregelmatig sterker en zwakker. Dit zou veroorzaakt kunnen worden door veranderingen in gelaagdheid en het scheef staan van de kabels met stroommeters in de periodes dat een warmere wervel door het kanaal trekt. Dit zorgt voor veranderingen in de paden van golven met de frequenties van het zons- en maansgetij en de positie van stroommeters ten opzichte van deze paden. De variatie was echter zo groot dat deze niet direct gerelateerd kon worden aan de wervels.

Om het langetermijngedrag te bepalen is de bewegingsenergie met frequenties rond de getijfrequenties bepaald voor iedere stroommeter. De sterkste beweging is gevonden voor de bovenste stroommeters, rond de pycnocliene (diepte-interval waarin de dichtheid snel verandert met de diepte, hier voornamelijk als gevolg van de sterke temperatuurverandering). Deze resultaten zijn vergeleken met een numeriek model dat getijden genereert door een stroming over de bodemtopografie voor te schrijven. De gelaagdheid in dit model is gebaseerd op de gemeten profielen van temperatuur en zoutgehalte. Uit het getijgeneratie-model blijkt ook dat de interne getijstromingen het sterkst zijn rond en boven de pycnocliene. De pycnocliene zorgt voor extra reflecties en verstrooiing van interne golven, wat in een stralenmodel niet aanwezig is.

Een aantrekker is hiermee niet waargenomen. Maar men moet niet vergeten dat in de oceanografische praktijk slechts puntmetingen beschikbaar zijn, terwijl in het laboratorium een heel vlak bekeken kon worden. Uit het numeriek model blijkt bijvoorbeeld wel duidelijk dat er gebieden zijn met sterkere en minder sterke interne getijden, waar geen metingen beschikbaar waren. Verder zijn het niet noodzakelijk de getijfrequenties die tot de sterkste en eenvoudigste aantrekkers leiden, dat hangt geheel van de gelaagdheid en de bekkenvorm af. Het is waarschijnlijk dat er in de praktijk op zijn minst rudimenten van golfaantrekkers te vinden zijn in de vorm van geïsoleerde plekken met sterke inwendige getijden die niet als golven rechtstreeks afkomstig van een generatiegebied te interpreteren zijn. In dit licht bezien kan dit proefschrift, met al zijn beperkingen, bijdragen aan inzicht in het gedrag van interne golven in de oceaan.

Dankwoord

Uiteindelijk schreef ik dit proefschrift niet alléén. Op deze plaats wil ik een aantal mensen bedanken die direct of indirect hebben bijgedragen.

Allereerst mijn co-promotor Leo Maas, voor al zijn enthousiasme, uitleg en ideeën, en voor het altijd tijd hebben of maken voor discussies en het geven van commentaar. Door zijn veelzijdige belangstelling kreeg ik de kans om naast theoretisch onderzoek ook lab-experimenten en 'écht' zee-onderzoek te doen, wat ik een prachtige combinatie vind. Ook op persoonlijk gebied was het voor mij een bijzonder prettige samenwerking. Mijn promotoren Hans Duistermaat en Ferdinand Verhulst moet ik bedanken voor hun blijvende belangstelling en de vrijheid die ik gekregen heb. De privé-colleges van Hans hebben duidelijk hun vruchten afgeworpen voor het tweede hoofdstuk.

Het experimenteren was een tamelijk nieuwe, maar geweldige ervaring. I thank the people of the Coriolis Lab in Grenoble for their support. We worked hard, but in a relaxed and pleasant atmosphere. Merci beaucoup. In hetzelfde kader wordt Gert-Jan van Heijst bedankt voor het bieden van de gelegenheid om nieuwe experimenten te doen aan de Technische Universiteit Eindhoven. Gert van der Plas zorgde voor de praktische realisatie en voor mijn inwijding in de particle tracking software. Ronald en Maartje waren mede verantwoordelijk voor de metingen en de prettige tijd in Grenoble. Maartje deelde mijn enthousiasme voor het experimenteren en was bij beide sessies betrokken, in Grenoble als afstudeerstudente en in Eindhoven uit zuivere belangstelling. Het was leuk samenwerken en samen kletsen. Voor de experimenten en de data-nazorg, evenals vele computervragen en vraagjes kon ik altijd terecht bij Frans Eijgenraam.

Ook de oceaan heb ik aan den lijve mogen ondervinden. Herman Ridderinkhof, de Pelagia-bemanning en mede-opstappers van de ACSEX-3-tocht: het was een onvergetelijke tijd aan boord. Maar ook heeft het me inzicht gegeven in de moeilijkheden en beperkingen bij het doen van metingen in zee. Theo Gerkema bedank ik voor zijn bijdrage aan het bijbehorende hoofdstuk.

Natuurlijk moet ik ook al mijn andere collega's bedanken voor de gezelligheid, serieuze en minder serieuze gesprekken, maar ook voor adviezen en hulp bij wat voor problemen dan ook. In het bijzonder vermeld ik Sjef en Astrid, die veel meer werden dan collega's.

Er was ook een leven buiten het werk. Suzanne, Julius, Arja, Lianke, Yvonne, Thierry, Ulrike, Ester, Matthijs en Ron, bedankt voor jullie vriendschap. Ik zag jullie minder vaak dan ik zou willen, jullie wonen helaas niet om de hoek.

Dichter bij huis was er gelukkig muziek: Bert Honig en mijn mede-ensembleleden, jullie hebben het wonen in Den Helder een stuk leuker gemaakt.

Mijn ouders waren er altijd voor me. Bedankt voor alles! Ook mijn broer verdient een eervolle vermelding. Tenslotte Bas, bedankt voor al je liefde en geduld.

Astrid

Curriculum Vitae

Astrid Manders werd op 5 april 1975 geboren te Venray en groeide op in Vierlingsbeek. Van 1987 tot en met 1993 bezocht zij de scholengemeenschap Jerusalem in Venray, waar zij haar gymnasium-β-diploma behaalde. In 1993 begon zij aan een studie geofysica aan de Universiteit Utrecht. Tijdens deze studie van de vaste aarde (propedeuse in 1994), aangevuld met wis- en natuurkundevakken (propedeuse natuurkunde in 1995), ontstond de interesse voor vloeistofdynamica. Dit resulteerde in een afstudeeronderzoek naar smelten en compactie van poreus gesteente, in een eenvoudig model voor smeltvorming onder een mid-oceanische rug. Deze periode werd in augustus 1998 afgesloten met het doctoraaldiploma. Direct daarna begon zij aan haar promotie-onderzoek aan het Nederlands Instituut voor Onderzoek der Zee, waarin het enthousiasme voor de vloeistofdynamica een plaats kreeg en ook de oceanografie grondig verkend kon worden. Hiervan is dit proefschrift de weerslag.